

Università degli Studi di Napoli “Federico II”

Scuola Politecnica e delle Scienze di Base
Area Didattica di Scienze Matematiche Fisiche e Naturali

Dipartimento di Fisica “Ettore Pancini”



Laurea Magistrale in Fisica
Tesi sperimentale

Physics of the Josephson effect in junctions with ferromagnetic barriers

Relatori:
Prof. Francesco Tafuri

Candidato:
Halima Giovanna Ahmad
N94000315

A.A. 2016/2017

Contents

List of Figures	4
List of Tables	7
Introduction	8
1 Conventional Josephson junctions	10
1.1 Notes on superconductivity	10
1.2 SIS Josephson junctions	13
1.2.1 Voltage-Current curves	18
1.2.2 Junctions in magnetic fields	31
1.2.3 Dependence on temperature	37
1.3 SNS Josephson junctions	40
2 SFS and SIFS junctions	45
2.1 Ferromagnetic barriers	45
2.2 Superconducting ferromagnets	47
2.3 SFS junctions	49
2.3.1 Voltage-current characteristics	49
2.3.2 SFS junctions in magnetic fields	49
2.3.3 π -junctions and ϕ -junctions	50
2.3.4 Triplet current in SFS JJs	54
2.3.5 Higher harmonics in CPR for SFS JJs	55
2.4 SIFS junctions	55
2.4.1 Spin-filtering	56

2.4.2	Gadolinium Nitride barriers	59
2.4.3	Second harmonics in CPR	60
2.4.4	Josephson triplet currents in SIFS JJs	63
3	Experimental set-up	68
3.1	Samples scheme	68
3.2	Cooling System	70
3.3	Filtering systems and electronics	73
3.3.1	$I(V)$ measurements	74
3.3.2	$R(T)$ measurements	75
3.3.3	Measurements in magnetic fields	76
3.3.4	Discussion on the errors	76
4	Experimental results	79
4.1	Spin-filtering efficiency	79
4.2	Damping regime of the junctions	82
4.2.1	Critical currents	83
4.2.2	Normal resistances	85
4.2.3	Stewart-McCumber parameters	86
4.3	Fraunhofer pattern analysis	88
4.3.1	Long or small junctions regime	91
4.3.2	Hysteresis in the Fraunhofer patterns	92
4.3.3	Second harmonic	94
4.4	$I_c(T)$ curves	96
	Conclusions	100
	Bibliography	103

List of Figures

1.1	Meissner effect	11
1.2	Dispersion relation for a superconductor	12
1.3	BCS $\Delta(T)$	13
1.4	SIS JJ scheme	14
1.5	JJ equivalent circuit	18
1.6	Washboard potential $U(\varphi)$	20
1.7	$\bar{\eta}(\alpha)$ in the overdamped regime	22
1.8	Hysteresis versus dissipation in NRSJ model $\bar{v}(\alpha)$ for $n = 1$	24
1.9	Hysteresis versus dissipation in NRSJ model $\bar{v}(\alpha)$ for $n = 2$	25
1.10	Measured $I(V)$ for a SIS JJ	26
1.11	$\beta(\tau)$ in the RSJ model	29
1.12	$\beta(\tau)$ in the NRSJ model for a discontinuous $I_N(V)$	30
1.13	$\beta(\tau)$ in the NRSJ model for a parabolic sub-gap	30
1.14	Fraunhofer pattern in a SIS JJ	31
1.15	Integration circuit for the Fraunhofer pattern	32
1.16	Pattern for different non-uniform density J_c	35
1.17	Fraunhofer pattern in an anisotropic magnetic field	36
1.18	Fraunhofer pattern for a long JJ	37
1.19	$R(T)$ and AB fit on $V_c(T)$ in a Nb-AlO _x -Nb JJ	38
1.20	Effect of the electron-phonon strong coupling in the $V_c(T)$	39
1.21	Andreev reflections	41
1.22	Measured $I(V)$ for a SNS JJ	42
1.23	$I_c(T)$ in a short weak link	44
2.1	Magnetization $M(T)$	46

2.2	Ferromagnet magnetization $M(H)$	47
2.3	Order parameter in a SFS JJ	48
2.4	Measured hysteretic Fraunhofer pattern in a SFS JJ	50
2.5	Oscillation in the $I_c(T)$ of a π -JJ	51
2.6	ϕ -JJ $I(V)$	53
2.7	$U(\varphi)$ in presence of a second harmonic in the CPR relation	54
2.8	$Q(g)$ phase-diagram	55
2.9	Barrier height in a spin-filter device	57
2.10	Band structure for metals, ferromagnets and half-metals	59
2.11	Second-harmonic Fraunhofer pattern and Goldobin model	62
2.12	SIFS junction in the Bergeret model	63
2.13	$(I_c(T)/I_c(0))(T/T_c)$ for $h = 0$ and $\alpha = \beta = \pi/2$ vs. r	64
2.14	$(I_c(T)/I_c(0))(T/T_c)$ for $h = 0.576\Delta(0)$ and $\alpha = \beta = \pi/2$ vs. r	65
2.15	$(I_c(T)/I_c(0))(T/T_c)$ for $h = 0.576\Delta(0)$ and $r = 0.06$ vs. $\alpha = \beta$	66
3.1	Sample scheme	69
3.2	Cooling system	71
3.3	IVC	72
3.4	$I(V)$ electronic set-up	74
3.5	$R(T)$ electronic set-up	75
3.6	Noise and error bar in $I(V)$	77
4.1	$R(T)$ curves	80
4.2	$R(T)$ fit on B_JJ4 and H_JJ7	81
4.3	Spin-filtering efficiency and fit	83
4.4	Long-range $I(V)$ at 300 mK and $I_c^{\text{avg}}(t)$	84
4.5	$R_N(t)$ and Simmons model	85
4.6	Stewart model on H_JJ7	87
4.7	$I(V)$ in a magnetic field for F_JJ6	89
4.8	Measured SIFS Fraunhofer patterns	90
4.9	Hysteresis fit for D_JJ5, F_JJ6, G_JJ1	93
4.10	Hysteresis and spin-filtering efficiency vs. the barrier thickness	94
4.11	Goldobin model applied to measured SIFS JJs	95
4.12	Normalized $I_c(T)$ for measured SIFS JJs	97

4.13 Bergeret model applied to our SIFS JJs	99
4.14 Triplet conduction in SIFS JJs	102

List of Tables

1.1	Characteristic parameters of a SIS JJ	27
3.1	GdN barrier thicknesses	69
4.1	Maximum resistance R_{\max}	81
4.2	Spin-filtering efficiency	82
4.3	β and Q factors	88
4.4	L/λ_J and long/small junction limit	92
4.5	Estimated parameters in the Goldobin model	96
4.6	$I_c(T)$ normalization parameters in measured SIFS JJs	96

Introduction

Superconductors exhibit zero resistance and perfect diamagnetic behavior when cooled below a characteristic critical temperature T_c .

One of the most significant theoretical advancement in the field of the superconducting physics came in 1962 when Brian D. Josephson predicted that a non-zero non-dissipative electrical current could flow between two superconducting electrodes, even if separated by an insulating, metallic or semiconducting barrier [1]. Such a device, known as *Josephson junction* (JJ), is very appealing for engineering application in superconducting electronics.

From the point of view of the fundamental physics, the Josephson effect is unique, since it gives direct access to the phase difference φ of the macroscopic wavefunctions that describe the superconducting state.

In this thesis, we will investigate some key features of Josephson junctions where the barrier is composed of a ferromagnet (SFS JJs), because novel phenomena are generated for this type of devices, like a non-monotonic dependence of the *critical current*, i.e. the non-dissipative current at zero voltage, on the ferromagnet layer thickness. In particular, we will analyze junctions composed of a GdN barrier between two NbN electrodes, fabricated at the Materials Science and Metallurgy Department of the University of Cambridge (UK).

In a temperature range from a few millikelvins up to some kelvins the gadolinium nitride GdN is in a ferromagnetic phase and behaves like an insulator, with a large energy gap between the valence and the conductance band [2]. The insulating nature of the ferromagnet will give additional features to the already-known SFS phenomena.

In chapter 1 we will give some hints on the quantum nature of the Joseph-

son effect in junctions with an insulating barrier (SIS) and a metallic weak link (SNS), commonly reported as *conventional* JJs, because their properties have been widely accounted by models fully obeying to BCS theory.

The SFS JJs, instead, fall in another category with remarkable deviations from SIS behavior, commonly reported as *unconventional* junctions. To understand the ferromagnetic junctions phenomenology, we will introduce the theoretical background of SFS JJs in chapter 2.

The possibility to measure samples with different barrier thickness (from 1.50 nm to 3.50 nm) allows a comparative study. In chapter 3, we will describe the experimental set-up and the techniques used to perform low noise and high precision measurements. We will also report a discussion on the errors.

The experimental data will be presented and discussed in chapter 4, in which every section will deal with the following measurements:

- temperature dependence of the resistance, in order to study the superconductive transition of the junctions and the barrier paramagnet-ferromagnet transition that occurs at a nominal temperature of about 30 K;
- voltage-current characteristics, with the aim of studying the electro-dynamical properties of the junctions, measuring footprint parameters described in chapter 1;
- voltage-current characteristic in presence of external magnetic fields, in order to analyze the coupling of the devices with a magnetic field;
- voltage-current characteristic measured at different temperatures from the base temperature of 300 mK up to the critical temperature of the device, to study the critical current dependence on temperature.

We will show that these junctions are of high quality, very robust and exhibit unique properties: spin-filter properties, very low dissipation, a dominant second harmonic in the current-phase relation (CPR) and an exotic critical current dependence on temperature, linked to unconventional conduction processes.

Chapter 1

Conventional Josephson junctions

In this chapter we will give some hints on superconductivity, providing the terminology that we will use. Then, we will concentrate our attention on the most important properties of conventional Josephson junctions and their phenomenology [3], so that we can compare our results on the unconventional junctions studied in this work with those found in literature.

1.1 Notes on superconductivity

According to F. London (1935), superconductivity is a quantum phenomenon characterized by perfect conduction and complete diamagnetism [4]. The resistance R , in fact, becomes zero below a certain critical temperature T_c , and at the same time magnetic fields \mathbf{B} are completely expelled from the superconductors.

A small percentage of the magnetic fields penetrates in the superconductor within a characteristic distance, named as *London depth* λ_L ,

$$\lambda_L^2 = \frac{|\psi|^2 4\pi e^{*2}}{m^* c^2}, \quad (1.1)$$

where $|\psi|^2$ is the *superfluid density* of the superconductor, linked to the superconductor carriers density, and e^* and m^* are the charge and the mass of the particles involved in the conduction; this effect is known as *Meissner*

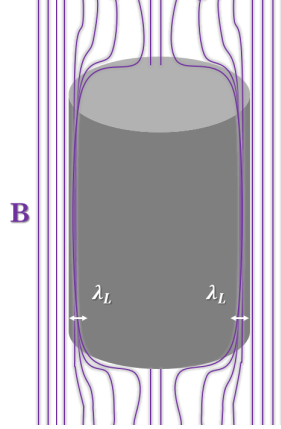


Figure 1.1: Magnetic field and representation of the Meissner effect

effect [5] (figure 1.1).

Dissipationless conduction and complete diamagnetism are described in the *London theory* by equations 1.2 and 1.3, respectively expressed in terms of the measurable electric field \mathbf{E} , the current density \mathbf{J} and the magnetic field \mathbf{B} ,

$$\frac{\partial \mathbf{J}}{\partial t} = \frac{|\psi|^2 e^{*2}}{m^*} \mathbf{E} \quad (1.2)$$

$$\nabla \wedge \mathbf{J} + \frac{|\psi|^2 e^{*2}}{m^* c} \mathbf{B} = 0. \quad (1.3)$$

The microscopic theory of superconductivity, the *BCS theory*, proposed by Bardeen, Cooper, Schrieffer [6], and extended by Gor'kov [7] and Anderson [8] after a few years, allows to understand the nature of the carriers: dissipationless conduction is ensured by the formation of electron pairs in a singlet state due to the delayed interaction mediated by phonons. These pairs, called *Cooper pairs*, have an effective mass m^* and charge e^* equal to

$$\begin{aligned} m^* &= 2m_e \\ e^* &= 2e, \end{aligned} \quad (1.4)$$

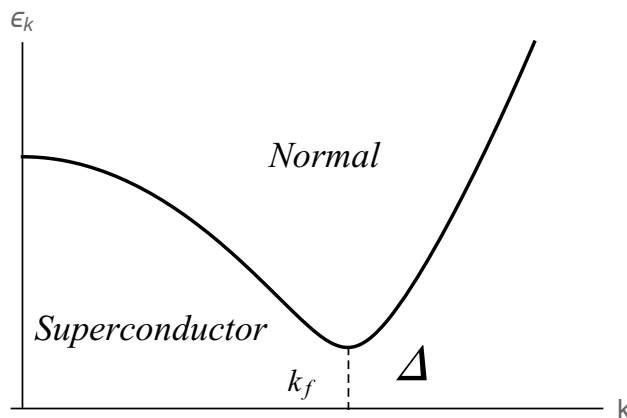


Figure 1.2: Single particle excitation spectrum in a superconductor: the gap near k_f is nearly a constant and, as a consequence, $\Delta_{\mathbf{k}} = \Delta$.

and form a *phase state*¹ [9]

$$|\psi\rangle_{\text{BCS}} = \prod_{\mathbf{k}} \left(u_{\mathbf{k}} + v_{\mathbf{k}} e^{i\vartheta_{\mathbf{k}}} c_{\mathbf{k}\uparrow}^{\dagger} c_{-\mathbf{k}\downarrow}^{\dagger} \right) |0\rangle. \quad (1.5)$$

The amplitude of a Cooper pair ($-\mathbf{k} \downarrow, \mathbf{k} \uparrow$) is the non-vanishing product of the two coefficients $v_{\mathbf{k}}$ and $u_{\mathbf{k}}$ [9],

$$u_{\mathbf{k}} v_{\mathbf{k}} = \frac{1}{2} \frac{\Delta_{\mathbf{k}}}{E_{\mathbf{k}}}, \quad (1.6)$$

where $E_{\mathbf{k}}$ is the single particle excitation energy in figure 1.2,

$$E_{\mathbf{k}} = \sqrt{\xi_{\mathbf{k}}^2 + \Delta_{\mathbf{k}}^2}, \quad (1.7)$$

and $\Delta_{\mathbf{k}}$ is the energy gap that opens in the excitation spectrum.

A look on the excitation spectrum $E_{\mathbf{k}}$ suggests that for excitation energy $k_B T$ lower than the energy gap $\Delta_{\mathbf{k}}$, the system is in its superconductive phase; on the contrary, for excitation $k_B T$ higher than the gap, the superconductor enters in the normal phase. According to this, the energy gap $\Delta_{\mathbf{k}}$ takes the place of an order parameter: for temperature higher than a critical

¹A phase state is simply a $U(1)$ broken symmetry physical state with conserved phase $e^{i\vartheta_{\mathbf{k}}}$.

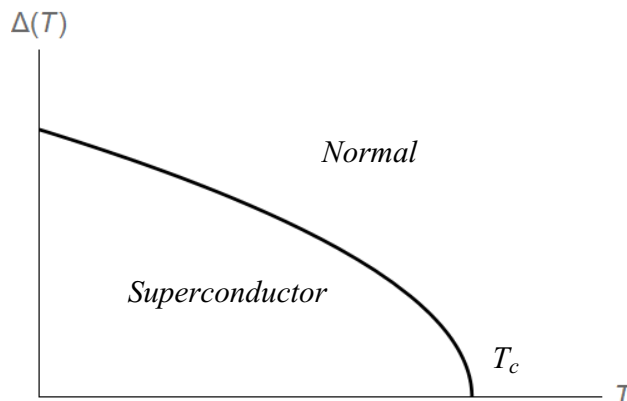


Figure 1.3: $\Delta(T)$ dependence in BCS theory

temperature T_c , the energy gap is zero, while when $T < T_c$ the gap is different from zero and it has the temperature dependence in the BCS theory [6] (figure 1.3)

$$\Delta_{\mathbf{k}}(T) \sim 1.74 \frac{\pi}{\gamma} k_B T_c \sqrt{1 - \frac{T}{T_c}}, \quad (1.8)$$

where $\gamma \sim 1.78$ and T_c is linked to the energy gap by the universal relation

$$T_c = \frac{\Delta_{\mathbf{k}}}{1.76 k_B}. \quad (1.9)$$

1.2 SIS Josephson junctions

The Josephson effect, at a divulgative stage, is commonly depicted as the flow of a supercurrent in a barrier of the order of some nanometers separating two superconductors. Such a device, named as *Josephson junction* (JJ), is represented in figure 1.4.

In this distance range Cooper pairs can flow through the device without any voltage drop, and a phase correlation between the two superconductors is realized. The nature of this phase correlation is truly quantum, but at the same time it is something much more sophisticated: in fact, the phase difference $\varphi = \vartheta_L - \vartheta_R$ between the two superconductors of the junction is a

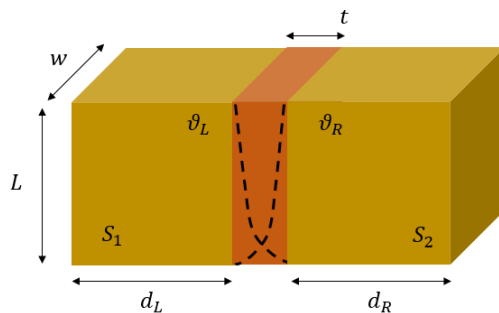


Figure 1.4: An example of a Josephson junction and wave function tails in the insulating barrier

macroscopic variable, regulated by the two equations:

$$I_s = I_c \sin \varphi \quad (1.10)$$

$$\frac{\partial \varphi}{\partial t} = \frac{e^* V}{\hbar}, \quad (1.11)$$

where e^* equals $2e$, V is the voltage drop between the two electrodes, I_s is the supercurrent across the device and I_c is the *critical current*, which is proportional to the carriers tunneling coefficient, and it depends on the geometry, the material and the thickness of the barrier like a decaying exponential function [3].

The first equation states that the current that flows through the junction depends only on the phase difference between the two superconducting electrodes; the second one, instead, states that the application of a voltage drop on the junctions leads to variations in time of the phase difference. Moreover, it is derived solely from the main principles of quantum mechanics and contains only fundamental constants: in short, it is a “universal equation” [10].

A general expression for the supercurrent in equation 1.10 can be derived if we take into account the monodromy of the junction wave function $\Psi(\mathbf{r}_1 \dots \mathbf{r}_{2n})$, where $\mathbf{r}_1 \dots \mathbf{r}_{2n}$ are particle coordinates and n is the Cooper pairs number,

$$\Psi(\mathbf{r}_1 \dots \mathbf{r}_{2n}) = c_L \psi_L(\mathbf{r}_1 \dots \mathbf{r}_{2n}) + c_R \psi_R(\mathbf{r}_1 \dots \mathbf{r}_{2n}). \quad (1.12)$$

The supercurrent at φ must equal the supercurrent at $\varphi + 2\pi$ and, as a consequence, it takes the form

$$I_s = I_c \sin \varphi + \sum_{m=2}^{\infty} I_{cm} \sin(m\varphi). \quad (1.13)$$

All terms except the first one, or *higher harmonics terms*, can be generally neglected in conventional tunnel junctions, while a second harmonic contribution becomes important in some unconventional junctions, as discussed in the next chapters of this work.

The zero voltage drop between superconducting electrodes of a Josephson junction indicates that there is no dissipation in the system; however, a Josephson junction is an energy-storing two-terminal device [11]. If the electrodes phase difference changes with time, this energy is simply

$$U = \int_{t_i}^{t_f} I_s(t)V(t) dt; \quad (1.14)$$

substituting the first and second Josephson equation in 1.14, we obtain

$$U = E_c (\cos \varphi(t_f) - \cos \varphi(t_i)), \quad (1.15)$$

where E_c is the *junction characteristic energy*,

$$E_c = \frac{\hbar}{e^*} I_c. \quad (1.16)$$

As a consequence, a Josephson device can be represented in an equivalent circuit as a *nonlinear reactance* L_s^{-1} . Considering an arbitrary process in which the phase difference is affected by small variations $\tilde{\varphi}$, the supercurrent takes the form

$$\tilde{I} = \int L_s^{-1} \tilde{V} dt, \quad (1.17)$$

with $L_s^{-1} = L_c^{-1} \cos \varphi$ and where L_c is the *characteristic inductance of the junction* [11],

$$L_c = \frac{\hbar}{e^* I_c}. \quad (1.18)$$

Besides the supercurrent, one can also observe:

- displacement currents due to the finite capacitance of a junction;
- thermal motion of the carriers, which induces also thermal and shot noise, i. e. current fluctuations and quasi-particle current.

Let us analyze in detail these current components.

The displacement current When the voltage between the two superconducting electrodes varies in time, a displacement current that depends on the capacitance C of the junction flows through the device,

$$I_D = C \frac{dV}{dt}. \quad (1.19)$$

The capacitance can be expressed as the well-known plane-condenser capacitance

$$C = \frac{\epsilon_r \epsilon_0}{t} A, \quad (1.20)$$

and the specific capacitance of the junction C/A is a slower function of t than the critical current density $J_c = I_c/A$, which is exponential in the thickness. In conclusion, the specific capacitance is nearly a constant in a wide range of critical current densities and it is of the order of the $\mu\text{F}/\text{cm}^2$ for conventional junctions.

In order to characterize the capacitance effect for a Josephson junction, we introduce the dimensionless *Stewart-McCumber parameter*

$$\beta \equiv (\omega_P R_0 C)^2, \quad (1.21)$$

where ω_P is the *plasma frequency*

$$\omega_P = \frac{1}{\sqrt{L_c C}}, \quad (1.22)$$

L_c is the characteristic inductance of the junction in equation 1.18 and R_0 is the resistance of the system.

Often, people introduce another important factor, linked to the Stewart-McCumber parameter: the *damping factor* Q^{-1} ,

$$Q^{-1} = \frac{1}{\sqrt{\beta}}, \quad (1.23)$$

where the quantity Q corresponds to the quality factor of an oscillator.

Junctions with high damping and low quality factor ($\beta \ll 1$ and small capacitance) are known as *overdamped junctions*; on the contrary, we call them *underdamped junctions*.

The quasi-particles current When the temperature in the system is different from zero, the thermal motion breaks some Cooper pairs and single electrons can flow through the junction. These electrons are different from metal electrons, and we call them *quasi-particles*. We do not observe them when the voltage across the junction is zero, but for T close to T_c , or slightly below that, the thermal energy $2k_B T$ is much larger than the sum of the superconducting gaps of the two electrodes ($\Delta_L + \Delta_R$), and the quasiparticle contribution to the current is large. As a consequence, the current follows the usual ohmic law

$$I_N(V) = \frac{V}{R_N}, \quad (1.24)$$

where R_N is the *normal resistance* of the junction and $I_N(V)$ is known as *normal current*. We observe this ohmic regime due to quasi particles also for $V > (\Delta_L + \Delta_R)/e$, at all temperatures.

In any case, the normal current can also present high non-linearities as a function of V , but one typically attributes these non-linearities to the normal resistance [11].

The combination of the normal current and the supercurrent suggests that in these systems a finite relaxation time exists: defining the *characteristic voltage of the junction* V_c as

$$V_c \equiv I_c R_N, \quad (1.25)$$

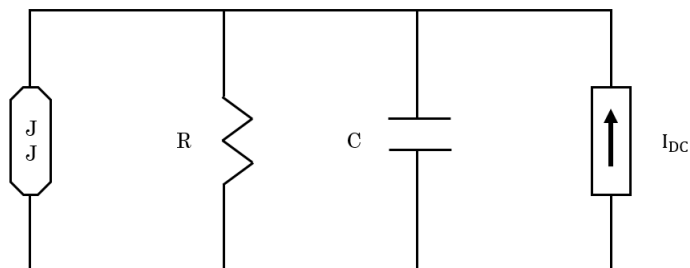


Figure 1.5: Equivalent circuit of a Josephson junction device

and using the equation 1.18, we get

$$\omega_c = V_c \frac{e^*}{\hbar} = \frac{R_N}{L_c}, \quad (1.26)$$

where the quantity on the left hand-side has a frequency dimension, and we will refer to it as *Josephson oscillation frequency* ω_c . This parameter is very important in practical application, like microwave devices based on the Josephson effect, which can be very important in superconducting circuits: in conventional Josephson junctions it is of the order of some terahertz, so that the fastest pulse-rise time is of the order of few picoseconds.

The normal current is a dissipative term and generates *thermal noise*, important in the low voltage range and for thermal energy higher than $\hbar\omega_c$, and *shot noise*, dominant in the high voltage range [11].

1.2.1 Voltage-Current curves

A Josephson junction can be represented by a simple equivalent circuit with a capacitor, a resistance and a non-linear element that contributes with a sinusoidal current in terms of the phase difference between the two superconductors of the junction [3] (figure 1.5).

The junction is current-biased by the use of a high impedance current generator: in this way, we can directly observe a zero-voltage state and the critical current in the voltage-current characteristics.

The $I(V)$ curves are symmetrical with respect to the origin and they can be found by solving the *Kirchhoff second circuit law*

$$I_{\text{DC}} = I_c \sin \varphi + I_N(V) + C \frac{dV(t)}{dt}. \quad (1.27)$$

We can observe two different regimes, which indicate the superconductive state, or *S state*, and the resistive one, also known as *R State*.

Let us first suppose that the bias current is smaller than the critical current of the junction: for negligible capacitances and normal currents, the equation 1.27 reduces to

$$\frac{I_{\text{DC}}}{I_c} = \sin \varphi, \quad (1.28)$$

which presents two stationary solutions at zero voltage:

$$\varphi_s = \arcsin(I_{\text{DC}}/I_c) \quad (1.29)$$

$$\varphi'_s = \pi - \arcsin(I_{\text{DC}}/I_c); \quad (1.30)$$

the junction is in its S state and a DC current flows without voltage drop. This phenomenon is the *DC Josephson effect*.

If the bias current exceeds the critical current, it can not be carried out only by the supercurrent and the normal current appears, enacting a non-zero voltage across the junction and an oscillation frequency different from zero: this is the *AC Josephson effect*, natural attribute of the R State.

The differential equation 1.27 can be also seen as describing a *phase particle* moving in a tilted washboard potential

$$U(\varphi) = E_c \left(1 - \cos \varphi - \frac{I_{\text{DC}}}{I_c} \varphi \right), \quad (1.31)$$

and subjected to a viscous force.

As we can observe in figure 1.6, the junction is in its S state when the ratio $I_{\text{DC}}/I_c = \alpha < 1$, i. e. the phase particle is trapped into a minimum of the washboard potential; on the contrary, the R state is reached for $\alpha > 1$, and the phase particle rolls down the washboard.

The higher is the damping, the stabler the R state is and thus the particle

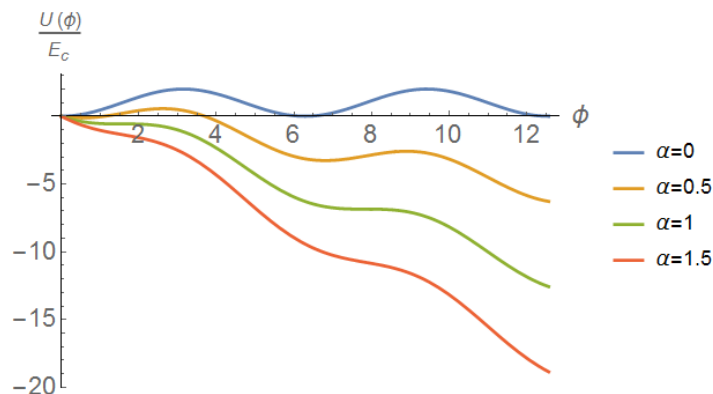


Figure 1.6: Washboard potential for the phase particle for different α values: *Mathematica11* simulations

remains in the finite voltage state until a current, known as *retrapping current* I_r , is reached.

In the underdamped regime one can observe a strong hysteresis in the $I(V)$ curves, i. e. the retrapping current is very small compared to the critical one. We will demonstrate in the next sections that the hysteresis degree strictly depends on the capacitance of the junctions and on dissipation processes in the devices.

RSJ and NRSJ models

With the aim of resolving the circuit equation 1.27, two models are commonly used: the *resistively shunted junction model* (RSJ) and the *non-linear resistively shunted junction model* (NRSJ). They both give predictions on the shape of the $I(V)$ curves, modeling the hysteretic behavior and the sub-gap leakage currents respectively.

In the RSJ model, the circuit equation 1.27 presents an ohmic normal current and it can be rewritten as

$$I_{\text{DC}} = I_c \sin \varphi(t) + \frac{V(t)}{R_N} + C \frac{dV(t)}{dt}; \quad (1.32)$$

the addition of noise currents in equation 1.32, typically in a stationary form, leads to the *generalized RSJ model* [3].

The RSJ model and its generalization allows to describe qualitatively experimental results for junctions with high damping ($\beta \ll 1$) and $\omega \ll \omega_g$, where ω_g is the frequency associated with the energy gap of the junction. Moreover, in this model the Cooper pairs current equals exactly the critical current, but it is a strong approximation; a microscopic approach with Green's functions, in fact, demonstrates that Cooper pairs current I_p depends non-trivially on the frequency, and in principle it can be different from the critical current. This last result is used in the *tunnel junction model* (TJM), which provides an almost exact description of tunnel junctions, but it is computationally more complex than other models here described, so we do not further focus our attention on this subject [3].

Let us define the normalized voltage η [3],

$$\eta = \frac{V}{V_c}, \quad (1.33)$$

the normalized current α ,

$$\alpha = \frac{I_{DC}}{I_c}, \quad (1.34)$$

and the dimensionless time χ ,

$$\chi = \omega_P t, \quad (1.35)$$

so that the circuit equation 1.32 becomes

$$\alpha = \sin \varphi(\chi) + \eta(\chi) + \sqrt{\beta} \frac{d\eta(\chi)}{d\chi}. \quad (1.36)$$

In the overdamped regime, i.e. for junction capacitance and β sufficiently small, we can analytically calculate the temporal mean value of the normalized voltage $\bar{\eta}$, as plotted in figure 1.7; we can observe that there is no hysteresis in the curve and that, for currents higher than a value of about $2I_c$, the $\bar{\eta}(\alpha)$ characteristic becomes linear.

Non-linear conductance is taken into account in the *non-linear-resistive shunted junction model* (NRSJ), where the normal current can be expressed

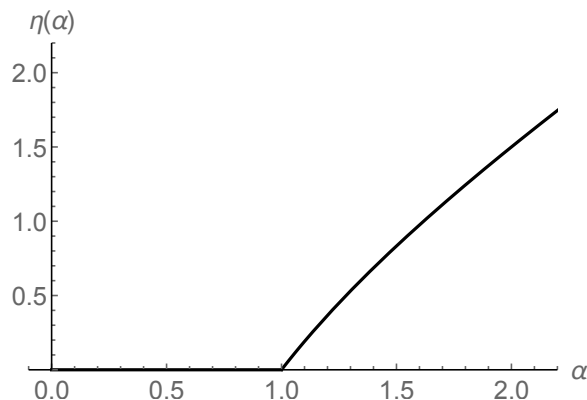


Figure 1.7: Normalized voltage $\bar{\eta}$ vs. the normalized current α : *Mathematica8* simulation, with $\beta = 0.001$

or as a discontinuous function

$$I_N(V) = \begin{cases} \frac{V}{R_L}, & |V| < V_g \\ \frac{V}{R_N}, & |V| > V_g, \end{cases} \quad (1.37)$$

where R_L is the *leakage resistance*, or as power-dependent on the voltage below the gap V_g , in the form

$$I_N(V) = I_0 (V/V_0)^n. \quad (1.38)$$

The second approximation, in particular, leads to the circuit equation

$$I_{\text{DC}} = I_0 \left(\frac{V(t)}{V_0} \right)^n + I_c \sin \varphi(t) + C \frac{dV(t)}{dt}, \quad (1.39)$$

where I_0 and V_0 are normalization parameters.

Following the work by W.C. Stewart [12], we first normalize the equation with respect to I_c and we define the normalized voltage $v(t)$,

$$v(t) = \left(\frac{I_0}{I_c} \right)^{1/n} \frac{V(t)}{V_0}, \quad (1.40)$$

so that equation 1.39 can be rewritten as

$$\alpha = \sin \varphi(t) + v(t)^n + \frac{C}{I_c} \left(\frac{I_c}{I_0} \right)^{1/n} V_0 \frac{dv(t)}{dt}. \quad (1.41)$$

This equation can be also expressed in terms of a derivative with respect to φ by using the second Josephson law (equation 1.11),

$$\alpha = \sin \varphi + v(\varphi)^n + k^{-1} v(\varphi) \frac{dv(\varphi)}{d\varphi}, \quad (1.42)$$

where the term k^{-1} is an alternative expression for the Stewart-McCumber parameter β that takes into account the non-linearities in the system,

$$k^{-1} = C \frac{2e}{\hbar I_c} \left(\frac{I_c}{I_0} \right)^{2/n} V_0^2. \quad (1.43)$$

We solved numerically the differential equation with *Mathematica11* for different α and k values, with the boundary condition

$$v(\varphi_s) = v(\arcsin(\alpha)) = 1, \quad (1.44)$$

finding out a set of periodical $v(\varphi)$ functions in the range $[\pi - \varphi_s, \varphi_s]$.

The normalized current-voltage characteristic is found by plotting the temporal mean values of $v(\varphi)$,

$$\bar{v} = \frac{2\pi}{\int_{\pi - \arcsin \alpha}^{\arcsin \alpha + 2\pi} \frac{1}{v(\phi)} d\phi}, \quad (1.45)$$

as a function of α .

Let us report analytical results for the current power-dependent on the voltage with $n = 1$ and $n = 2$.

For $n = 1$, we found the analytical result

$$\bar{v}(\alpha) = \alpha - \frac{1}{2\alpha \left(1 + \left(\frac{\alpha}{k} \right)^2 \right)}; \quad (1.46)$$

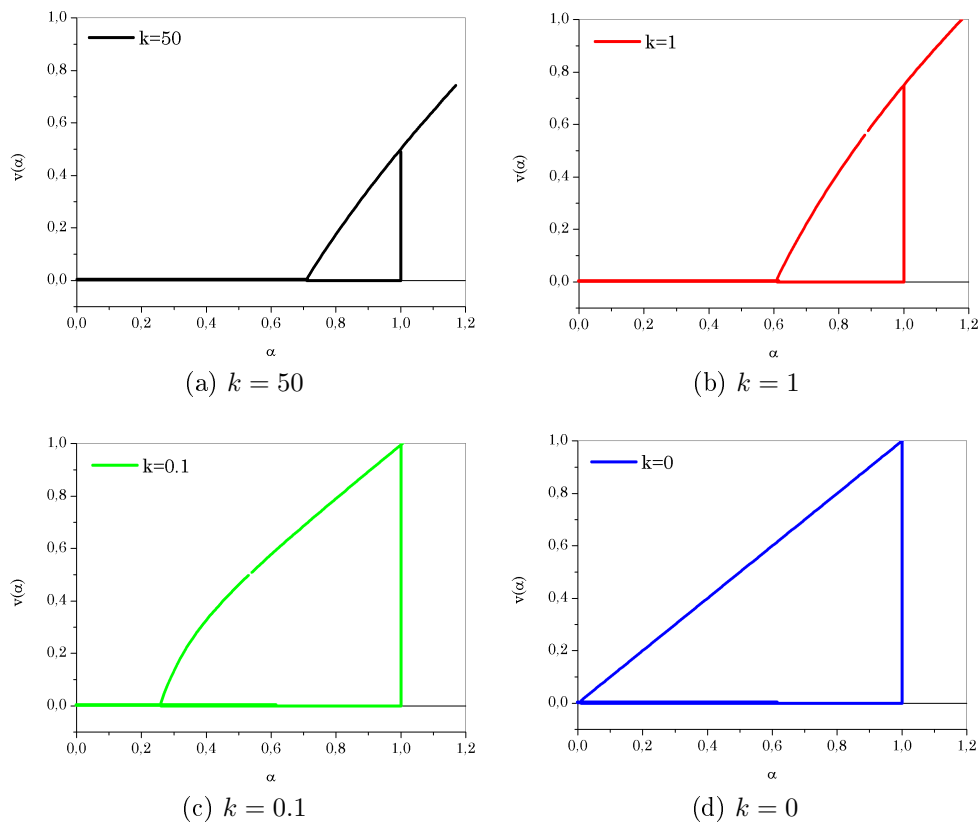


Figure 1.8: Normalized voltage-current characteristics in the NRSJ model in the case of linear normal current $I_N(V)$ ($n = 1$) for different k values: as k decreases (C increases), the hysteresis and the switching voltage in the curves increase

the $\bar{v}(\alpha)$ curves in the sub-gap region are plotted in figure 1.8 for different values of k . For all currents below the critical one, we can observe a hysteresis in the $I(V)$ curves, which gets more and more important when k tends to zero, according to the fact that the capacitance increases. At the same time the sub-gap shape reaches an ohmic behavior for $k = 0$. Also the voltage at which the S state to the R state transition occurs (switching voltage V_s) changes with k : the more k increases (C decreases), the more V_s decreases.

For a parabolic sub-gap, i. e. for $n = 2$, the analytical solution for the

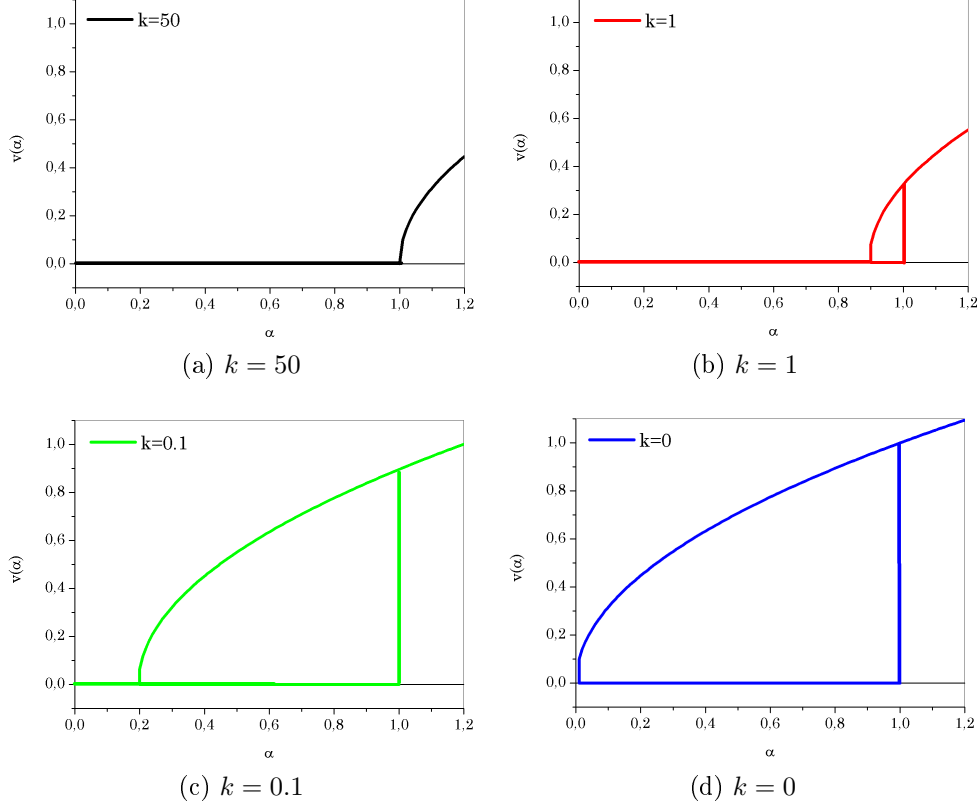


Figure 1.9: Normalized voltage-current characteristics in the NRSJ model in the case of parabolic normal current $I_N(V)$ ($n = 2$) for different k values: as k decreases (C increases), the hysteresis and the switching voltage in the curves increase

voltage dependence on the phase is

$$v(\varphi) = 1 - \frac{2\alpha_0}{\alpha + \alpha_0} \sin(\varphi + \gamma), \quad (1.47)$$

where the quantity α_0 and γ depend on k as

$$\alpha_0 = \frac{2k}{\sqrt{1 + 4k^2}} \quad (1.48)$$

$$\gamma = \arctan(2k). \quad (1.49)$$

The integration leads to the curves in figure 1.9 when \bar{v} is plotted as a function

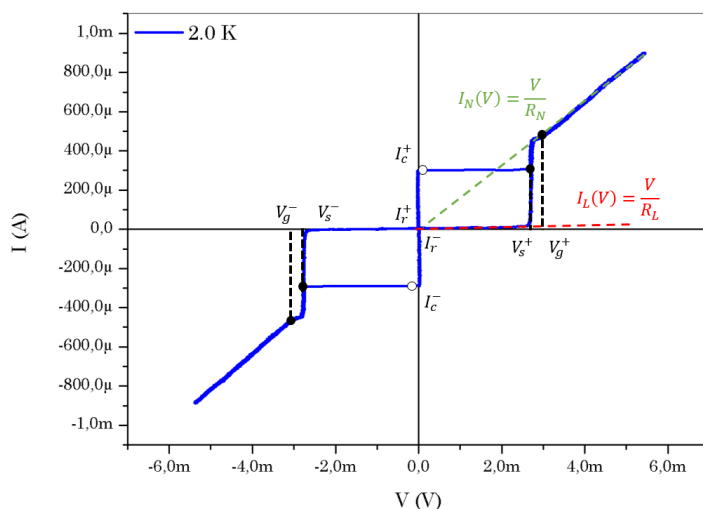


Figure 1.10: $I(V)$ characteristics measured at 2 K for a conventional Nb-AlO_x-Nb junction from Hypres

of α for different values of k . Also in this case the hysteresis and the switching voltage V_s increase as k decreases (C increases).

Finally, also for $n = \infty$ an analytical result for the $I(V)$ curves can be found: this case is more appropriate in the case of tunnel junctions with very high hysteresis degree, as in a junction with an insulating barrier made of AlO_x from Hypres, represented in figure 1.10, for which the characteristic parameters are reported in table 1.1². However, we do not focus on this case, because we will see that the $I(V)$ curves of the junctions analyzed in this work are very different from that observed in this conventional SIS JJ.

Hysteresis and Stewart-McCumber parameter

From an energetical point of view, the appearance of the hysteresis in the $I(V)$ curves means that the energy fed into the system by the external bias current is smaller than the energy lost because of dissipation processes linked to a quasi-particle flowing. As a consequence, the junction switches to the zero-voltage state at the retrapping current I_r , expressed in terms of the

²A discussion on the errors and the measurements techniques thanks to which we were able to estimate these parameters is reported in chapter 3 and in chapter 4. Values without errors are nominal parameters.

Table 1.1: Characteristic parameters of a typical Nb-AlO_x-Nb Josephson junction from Hypres

Parameters	Values
J_c	4.5 kA/cm ²
t	1 nm
ϵ_r	10
I_c^+	(302 ± 3) μA
I_c^-	(290 ± 3) μA
A	7 μm ²
R_N	(5.66 ± 0.11) Ω
$R_N A$	(37.2 ± 0.7) Ωμm ²
V_c	(1.68 ± 0.02) mV
ω_c	(5.11 ± 0.15) THz
C	0.58 pF
ω_P	(1.245 ± 0.006) THz
β	892

dissipated energy U_d as

$$I_r = \frac{U_d 2e}{\hbar}. \quad (1.50)$$

The dissipated energy

$$U_d = \int_0^{2\pi/\omega_c} dt I_N(V)V \quad (1.51)$$

can be calculated by substituting the expression of V in equation 1.11 in terms of the phase difference and by expliciting the normal current depending on the two models reported in section 1.2.1.

In the moderately damping regime, for example, the RSJ model can be employed. The normal current takes the form in equation 1.24 and the dissipated energy U_d is

$$U_d = \int_0^{2\pi/\omega_c} dt \frac{\hbar^2}{(2e)^2 R_N} \left(\frac{d\varphi}{dt} \right)^2. \quad (1.52)$$

The factor $\frac{d\varphi}{dt}$ is linked to the kinetic energy in the junction K ,

$$K = \frac{E_c}{2\omega_p^2} \left(\frac{d\varphi}{dt} \right)^2, \quad (1.53)$$

where E_c is defined in equation 1.16. The kinetic energy can be expressed in terms of the total energy E as

$$K = E - U, \quad (1.54)$$

with U energy fed in the junction in equation 1.15, here reported for sake of convenience for $\varphi(t_i) = 0$,

$$U = E_c (1 - \cos \varphi). \quad (1.55)$$

In conclusion, the dissipated energy takes the form

$$U_d = \int_0^{2\pi} d\varphi \frac{\hbar J_c}{2e\sqrt{\beta}} \sqrt{2 \left(\frac{E}{E_c} - 1 + \cos \varphi \right)}. \quad (1.56)$$

In the R State, the minimum of the kinetic energy K is positive, and the energy satisfies the condition

$$E \geq 2E_c. \quad (1.57)$$

At the limit energy value $E = 2E_c$, the current equals the retrapping current, and the dissipated energy is a function of the Stewart-McCumber parameter β ,

$$U_d = \frac{4}{\pi} \frac{\hbar}{2e} \frac{I_c}{\sqrt{\beta}}. \quad (1.58)$$

The retrapping current, in conclusion, takes the form

$$I_r = \frac{4}{\pi} \frac{I_c}{\sqrt{\beta}}, \quad (1.59)$$

and it decreases when the Stewart-McCumber parameter increases, i. e. when

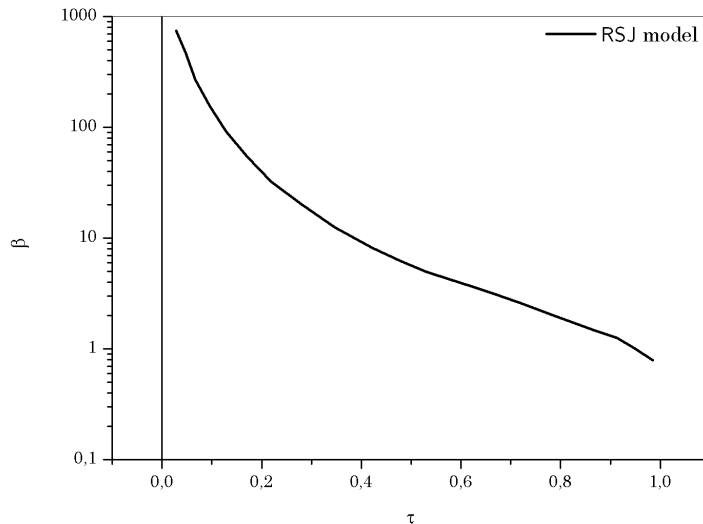


Figure 1.11: $\beta(\tau)$ in the RSJ model [3]

the capacitance of the junction tends to infinity. This means that the more the capacitance of the junction increases, the more the hysteresis is strong, as we have demonstrated with the analysis of the normalized voltage-current characteristics in the RSJ and in the NRSJ.

We can define the ratio $\tau = I_r/I_c$ as

$$\tau \sim \frac{4}{\pi} \frac{1}{\sqrt{\beta}}, \quad (1.60)$$

which allows to estimate the Stewart-McCumber parameter of the junction in a different manner than that exposed in equation 1.21 [3] (figure 1.11).

In the NRSJ the curve $\beta(\tau)$ slightly changes, according to the fact that the dissipated energy U_d is written in terms of a non-linear normal current. When $I_N(V)$ is a discontinuous function (equation 1.37), the theoretical dependence $\beta(\tau)$ shows the trend in figure 1.12; as a comparison, we plot also $\beta(\tau)$ in the RSJ model. When the normal current is a power-law as in equation 1.38, instead, $\beta(\tau)$ depends on the power n . For example, we compare the function $\beta(\tau)$ estimated from the simulations in the case $n = 2$ to the RSJ one in

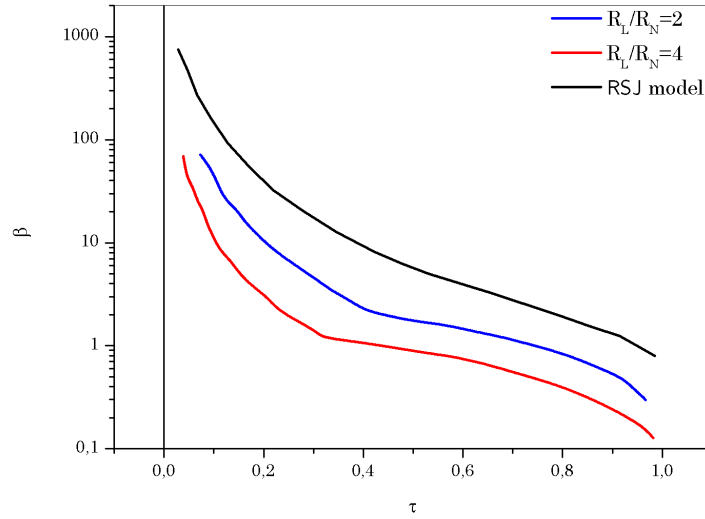


Figure 1.12: $\beta(\tau)$ in the NRSJ model for a discontinuous normal current in equation 1.37 for different R_L/R_N ratios [11]

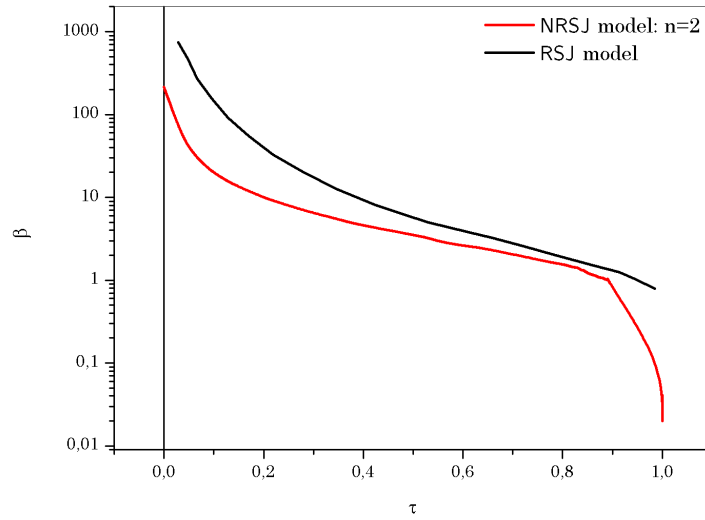


Figure 1.13: Estimated $\beta(\tau)$ in the NRSJ model for $n = 2$ and comparison with the RSJ curve

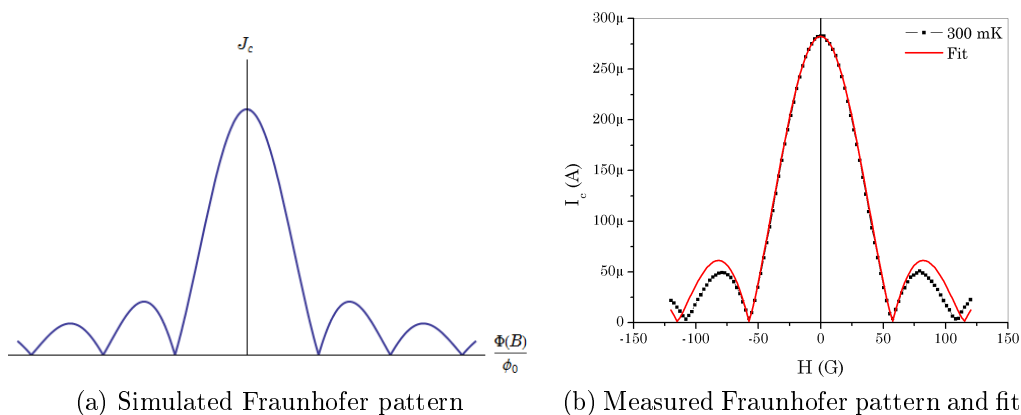


Figure 1.14: Analytical function of a Fraunhofer pattern and example of a measured Fraunhofer pattern in conventional Nb-AlO_x-Nb from Hypres: we calculated the fit function with *Mathematica*

figure 1.13.

1.2.2 Junctions in magnetic fields

Cooper pairs strong phase coherence and “wave nature” cause quantum diffraction and interference in presence of magnetic fields.

Experimentally, one can observe a supercurrent density modulated by the applied magnetic fields and a *Fraunhofer pattern* (figure 1.14), which is the ideal response of a Josephson junction with an uniform distribution of the critical current density J_c .

Let us consider a magnetic field in the \hat{y} -direction of the junction represented in figure 1.15, so that the vector potential \mathbf{A} has only a non-zero \hat{x} -component. Well inside the two superconducting electrodes, quantum currents that solve the London equations 1.2 and 1.3 assume zero values, so that

$$\nabla\varphi = \frac{e^*}{\hbar c} (\mathbf{A}(z \rightarrow \infty) - \mathbf{A}(z \rightarrow -\infty)), \quad (1.61)$$

where $\mathbf{A}(z \rightarrow \infty) - \mathbf{A}(z \rightarrow -\infty)$ is proportional to the magnetic flux across the barrier. Integrating along the two paths in figure 1.15, we get a first

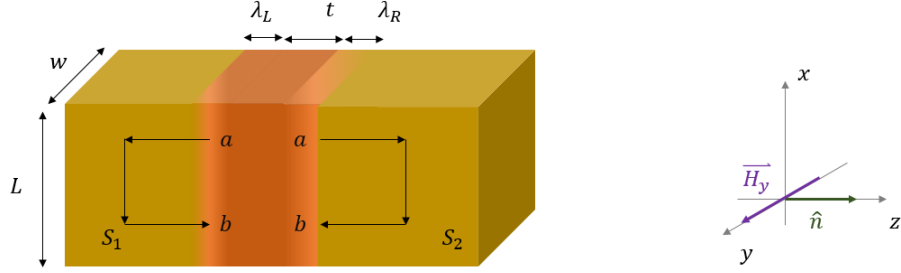


Figure 1.15: Integration circuit for the construction of the Fraunhofer pattern

order equation in x , which leads to

$$\varphi(x) = \frac{e^*}{\hbar c} H_y (\lambda_L + \lambda_R + t) x + \varphi(0), \quad (1.62)$$

where λ_L (λ_R) is the London length in the left (right) superconductor. The supercurrent density, then, can be expressed as

$$J(x, H_y) = J_c \sin \left(\frac{e^*}{\hbar c} H_y (\lambda_L + \lambda_R + t) x + \varphi(0) \right), \quad (1.63)$$

where the quantity $(\lambda_L + \lambda_R + t)$ is the magnetic spacing due to the field penetration into the surface sheets of electrodes for the *Meissner effect*, and we rename it d' for convenience.

When the electrodes thicknesses are smaller than the London penetration depth we have to take into account that Meissner currents are strongly reduced and an additional kinetic inductance must be added; the magnetic spacing is corrected and takes the form

$$d'' = t + \lambda_L \coth \left(\frac{d_L}{\lambda_L} \right) + \lambda_R \coth \left(\frac{d_R}{\lambda_R} \right), \quad (1.64)$$

where d_L (d_R) are the electrode thicknesses [13].

An integral of J_c on the surface Lw of the junction (figure 1.15), in the important hypothesis of current spatial uniformity, allows to write down the

critical current I_c as a function of the magnetic field,

$$I_c(H) = I_c(0) \left| \frac{\sin\left(\frac{\Phi(H)\pi}{\phi_0^*}\right)}{\frac{\Phi(H)\pi}{\phi_0^*}} \right|, \quad (1.65)$$

where ϕ_0^* is the magnetic flux quantum

$$\phi_0^* = \frac{hc}{e^*} = 2.07 \cdot 10^{-7} \text{ Gcm}^2, \quad (1.66)$$

and $\Phi(H)$ is the magnetic field flux. When the magnetic field flux is an integer multiple of the magnetic flux quantum, the critical current is zero, and the periodicity in terms of the magnetic field is

$$\Delta H = \frac{\phi_0^*}{Ld'}, \quad (1.67)$$

or in the latter case

$$\Delta H = \frac{\phi_0^*}{Ld''}. \quad (1.68)$$

The study of the Fraunhofer pattern is important to characterize the junctions: comparing the dimensions of the samples with some characteristic lengths, we can classify the Josephson junctions as *small* or *long junctions*.

Let us suppose that a magnetic field in the $\hat{x} - \hat{y}$ plane is applied, so that the equation 1.61 is a two first order equations system in x and y . We get a non-linear wave equation in the stationary case

$$\nabla^2 \varphi - \lambda_J^{-2} \sin \varphi = 0, \quad (1.69)$$

where λ_J is the *Josephson penetration length*

$$\lambda_J = \sqrt{\frac{\phi_0^*}{2\pi\mu_0 J_c d'}}, \quad (1.70)$$

written in terms of the critical current density J_c . With the aim of simplify the problem, let us take a phase that changes only in the \hat{x} -direction: the

boundary conditions for this problem are [9]

$$\begin{cases} \lambda_J \partial_x \varphi|_0 = \frac{I_- + d' \mu_0 H / L_0}{J_c} \\ \lambda_J \partial_x \varphi|_L = \frac{I_+ + d' \mu_0 H / L_0}{J_c}, \end{cases} \quad (1.71)$$

where L_0 is the specific inductance of the junction per unit length

$$L_0^{-1} = \int_0^L dy (\mu_0 d')^{-1}, \quad (1.72)$$

and $I_{-(+)}$ are the truly injected currents, which have to be added to the Meissner currents $d' \mu_0 H / L_0$. Clearly, for finite electrodes in the boundary conditions 1.71 one has to substitute the magnetic spacing d' with d'' [9].

When the $I_{-(+)}$ currents are zero, another magnetic spacing is induced [9]: by solving the system 1.71, we obtain

$$d''' = t + \lambda_L \tanh\left(\frac{d_L}{2\lambda_L}\right) + \lambda_R \tanh\left(\frac{d_R}{2\lambda_R}\right), \quad (1.73)$$

and the Josephson penetration depth is

$$\lambda_J = \sqrt{\frac{\phi_0^*}{2\pi\mu_0 J_c d'''}}. \quad (1.74)$$

Let us now classify the two Josephson junctions regime: the *small junction* regime and the *long junction* regime.

Small junctions We have a typical small junction when the transverse dimensions of the junctions are smaller than the Josephson penetration length, and the self field due to the current flowing in the electrodes is completely disregarded.

Deviations from the expected behavior of small junctions, like minima with non-zero current, suppression of the amplitude of some lobes or asymmetry of the pattern, can be related to non-uniform current distributions, arbitrary orientation of the magnetic fields applied or structural fluctuations [3].

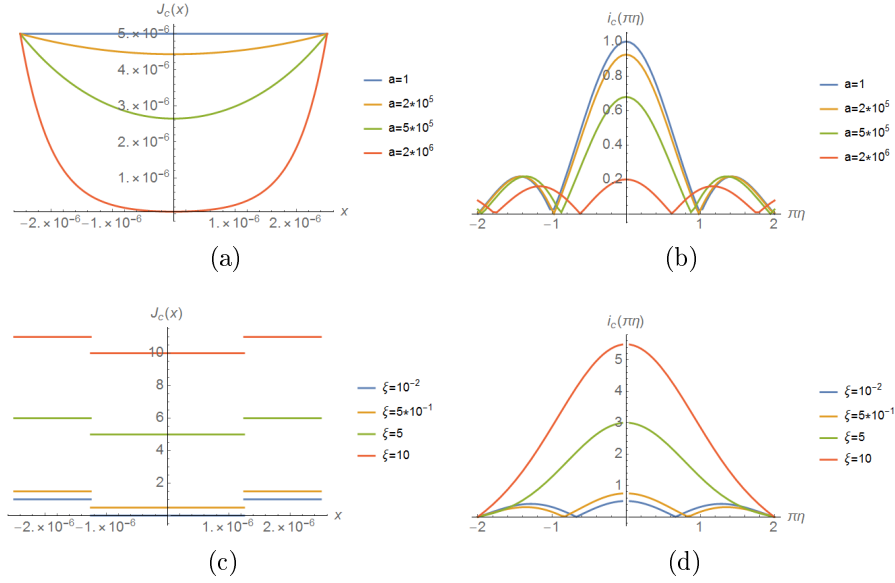


Figure 1.16: *Mathematica11* simulations of non-uniform density current distributions and relative Fraunhofer pattern: (a) *valley-like* current density vs. a ; (b) Fraunhofer pattern for the *valley-like* current density; (c) *step-like* current density vs. ξ for $s = L$ and L lateral dimension of the JJ; (d) Fraunhofer pattern for the *step-like* current density

For example, the density current distribution can assume a *valley shape*, i. e. the critical current is an x -function,

$$J_c(x) = J_{c0} \frac{\cosh(ax)}{\cosh(aL/2)}, \quad (1.75)$$

or it can be a *step-like* function,

$$J_c(x) = J_{c0} \left(\xi p_{1/2}(x) + p_{s/2} \left(x - \frac{L-s}{2} \right) + p_{s/2} \left(x + \frac{L-s}{2} \right) \right), \quad (1.76)$$

with $p_\tau = 1$ for $|x| \leq \tau$ and 0 elsewhere. For sake of clarity, in figure 1.16 we report simulations of these non-uniform current distribution for $J_{c0} = 1$, and relative Fraunhofer patterns.

An arbitrary orientation of external magnetic fields also determines deviations from the Fraunhofer pattern shape: the magnetic field flux,

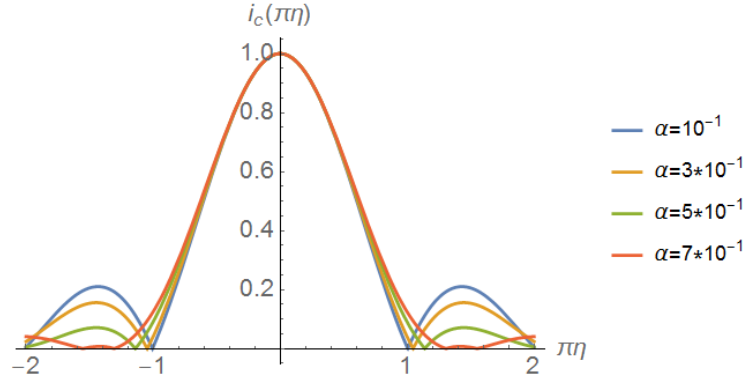


Figure 1.17: Fraunhofer pattern at different angles between magnetic field components H_x and H_y : *Mathematica11* simulations

in fact, assumes the general form

$$\Phi(\mathbf{H}) = \frac{2\pi d_m}{\phi_0^*} (|H| \sin \alpha x - |H| \cos \alpha y), \quad (1.77)$$

where d_m is the appropriate magnetic spacing. In figure 1.17, we report a simulations for different α -values.

Long junctions When the dimensions of the junction are comparable to λ_J , the critical current follows the self-consistent equation

$$I_c(H) = I_c(0) \left| \frac{\sin \left(\pi d_m L \left(H + \frac{2\pi}{c} \frac{I(H)}{w} \right) \right)}{\pi d_m L \left(H + \frac{2\pi}{c} \frac{I(H)}{w} \right)} \right|, \quad (1.78)$$

where H is the applied magnetic field and the term $\frac{2\pi}{c} \frac{I(H)}{w}$ is the contribution due to the self-field, so that the maximum does not occur at zero field, but at a value $-\frac{2\pi}{c} \frac{I_0}{w}$. In terms of the magnetic flux, it is possible to rewrite the equation 1.78 as

$$I_c(H) = I_c(0) \left| \frac{\sin \left(\pi \left(\frac{\Phi(H)}{\phi_0^*} + \frac{L^2}{4\pi\lambda_J^2} \frac{I(H)}{\phi_0^*} \right) \right)}{\pi \left(\frac{\Phi(H)}{\phi_0^*} + \frac{L^2}{4\pi\lambda_J^2} \frac{I(H)}{\phi_0^*} \right)} \right|. \quad (1.79)$$

The self-field starts to be significant at $\frac{L}{\lambda_J}$ values of the order of the

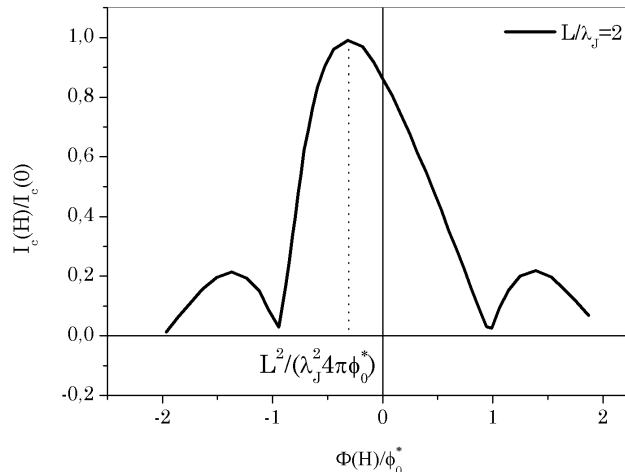


Figure 1.18: Simulated Fraunhofer pattern for a long JJ with $L/\lambda_J = 2$ [3]

unity [3] (figure 1.18).

1.2.3 Dependence on temperature

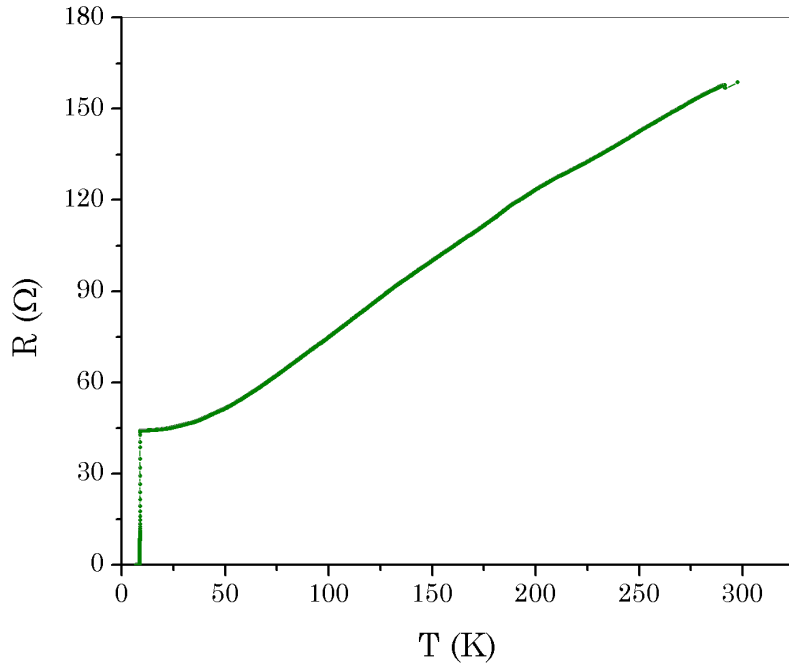
The temperature is a fundamental variable in Josephson junctions experiments. Its variations tune the superconducting properties in the devices.

In figure 1.19 (a), we present an example of a measured function $R(T)$ for a junction with an insulating barrier by *Hypres*, a Nb-AlO_x-Nb junction.

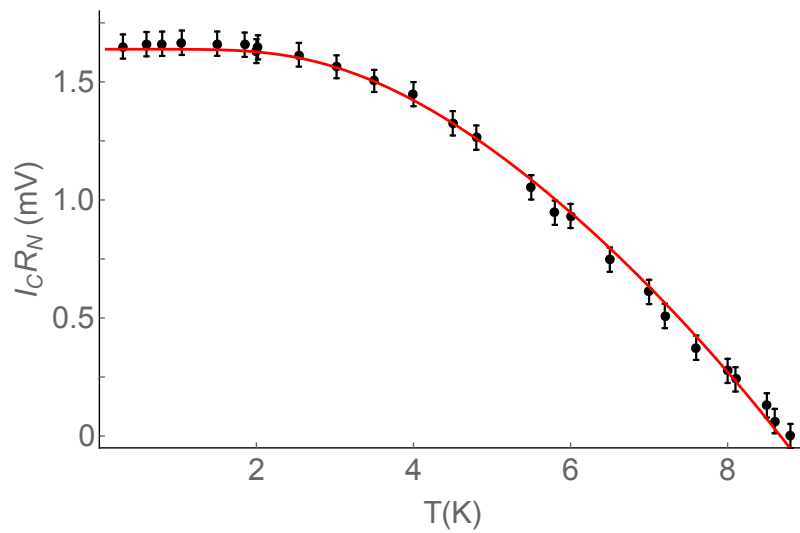
We can also observe that an increase in temperature determines a suppression of the critical current I_c , and as a consequence the characteristic voltage V_c of a JJ depends on temperature. In the BCS theory, it is expressed in terms of the temperature-dependent energy gap $\Delta(T)$ in equation 1.8, as

$$V_c(T) = \frac{\pi}{e^*} \Delta(T) \tanh\left(\frac{\Delta(T)}{2k_B T}\right). \quad (1.80)$$

This formula, known as *Ambegaokar-Baratoff relation* [14], can be approximated with two different analytic expressions for temperature smaller



(a) $R(T)$



(b) $V_c(T)$ and AB fit

Figure 1.19: Resistance versus temperature $R(T)$ and characteristic voltage dependence on temperature $V_c(T)$ for a typical Nb-AlO_x-Nb junction; the red curve on $V_c(T)$ is the AB fit

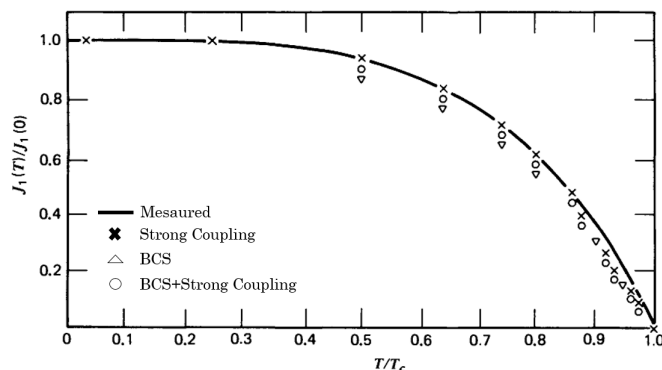


Figure 1.20: Normalized DC Josephson critical current versus reduced temperature; the solid line is an experimental curve measured in junctions Pb-Pb, the crosses and the circles represent two theoretical calculation taking into account the strong coupling, the triangles the BCS theory [3]

than $0.6T_c$ and for temperature near the critical one [3]:

$$V_J = \begin{cases} \frac{\pi}{e^*} \Delta(0) \left(1 - \frac{2\pi k_B T}{\Delta(0)} e^{-\frac{\Delta(0)}{k_B T}}\right) \tanh\left(\frac{\Delta(0) \left(1 - \frac{2\pi k_B T}{\Delta(0)} e^{-\frac{\Delta(0)}{k_B T}}\right)}{2k_B T}\right) & T < 0.6T_c \\ \frac{\pi}{e^*} \Delta(0) \gamma \sqrt{\frac{8}{7\zeta(3)}} \left(1 - \frac{T}{T_c}\right) \tanh\left(\frac{\Delta(0) \gamma \sqrt{\frac{8}{7\zeta(3)}} \left(1 - \frac{T}{T_c}\right)}{2k_B T}\right) & T \sim T_c, \end{cases} \quad (1.81)$$

with $\Delta(0)$ written in terms of the constant $\gamma \sim 1.78$ as

$$\Delta(0) = \frac{\pi}{\gamma} k_B T_c. \quad (1.82)$$

As an example, we show in figure 1.19 (b) the V_c dependence on temperature for a conventional Nb-AlO_x-Nb junction from Hypres, fitted by the AB relation for temperature near the critical one.

The AB formula does not include strong phonon-electron coupling effects, which typically reduce the critical current at temperatures near T_c [3] (figure 1.20). We will see, however, that in unconventional junctions a deviation in $V_c(T)$ can depend also on other parameters, and strong coupling effects are not sufficient to explain it (section 2.4.4 and section 4.4).

1.3 SNS Josephson junctions

Another class of Josephson junctions are the *SNS junctions*, i. e. junctions with a metallic or superconducting barrier, often called “weak link” [10].

In these structures, there are two important length scales that we have to introduce with the aim of classify them: the diffusive and ballistic thermal coherence lengths.

The *thermal coherence length in the diffusive regime* ξ_N^D , i. e. for junctions dimensions $L \gg l_N$ (l_N mean free path), is

$$\xi_N^D = \sqrt{\frac{\hbar D}{2\pi k_B T}}, \quad (1.83)$$

with D diffusion coefficient.

The *thermal coherence length in the ballistic regime* ($L \ll l_N$) ξ_N^B is

$$\xi_N^B = \frac{\hbar v_f}{k_B T}, \quad (1.84)$$

with v_f Fermi velocity.

If the barrier thickness does not exceed ξ_N^D (10 – 100 nm), or ξ_N^B (circa 10 000 nm), the Cooper condensate penetrates in both sides of the barrier, creating a φ -dependent supercurrent [15].

This effect is known as *proximity effect* [16], and it is induced by *Andreev reflections*: an electron with an energy below the superconducting gap is reflected at the interface as a hole, and the corresponding charge e^* is transferred to the Cooper pair that appears on the superconducting side of the interface (figure 1.21). In this mechanism, a closed path between electron and hole is established and a bound states is induced.

We will find different result in the diffusive, or *dirty limit*, and ballistic regime, also known as *clean limit*. However, in both regimes we can classify a Josephson SNS junction as *short weak link* or *long weak link*.

Let us first define the *effective spacing* d_{ef} between the electrodes as the distance between the closest points of the electrodes where the order parameter $|\psi|$ is equal to its value well-inside the superconductors, i. e. where the

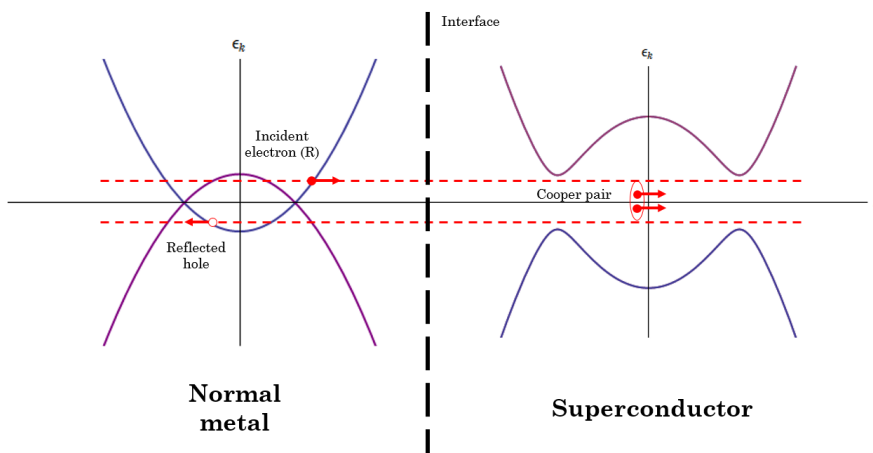


Figure 1.21: Scheme of the Andreev reflection mechanism

condensate wave function is weakly perturbed by the barrier. A SNS JJ is a *short weak link* if

$$d_{\text{ef}} \ll \xi_{\text{N}}^i, \quad (1.85)$$

while it is a *long weak link* if

$$d_{\text{ef}} \gg \xi_{\text{N}}^i, \quad (1.86)$$

with $i \equiv \{\text{D}, \text{B}\}$.

In the long weak link limit, deviations from the sinusoidal trend in the supercurrent become sensitively stronger than in short weak links [17, 18], where we can observe a quite ideal Josephson effect. However, in this thesis we will deal most of all with ferromagnetic junctions, which are similar to SNS short weak links, in the sense clarified in section 2.3.1, so we do not focus further on the long weak links behavior.

We will explore all the elements that characterize a Josephson junction in the case of a short metallic barrier, and we will give some hints on the shapes of the voltage-current characteristics, the coupling with a magnetic field and the critical current dependence on temperature.

Voltage-Current curves Qualitative description of the $I(V)$ curves in a weak link is given by the RSJ model in the overdamped regime (sec-

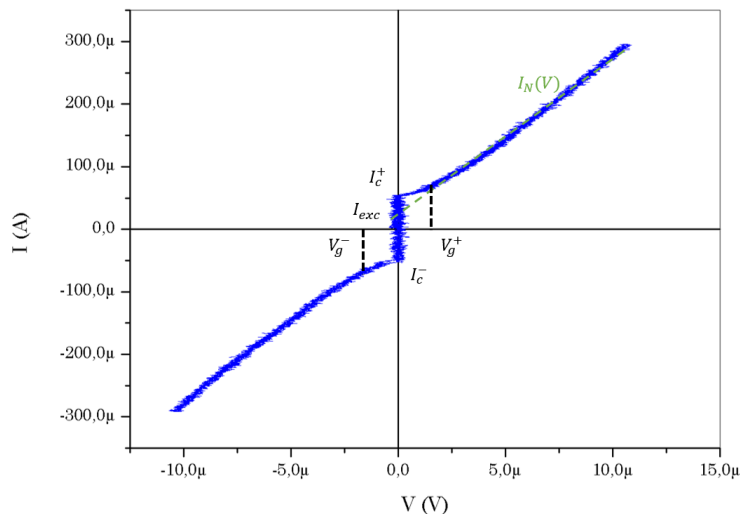


Figure 1.22: $I(V)$ characteristic for a weak link made of a multi-layer barrier Cu-Co-Cu-Ni-Cu interposed between two Nb electrodes

tion 1.2.1). The normal resistance is smaller than in SIS junctions, so as the characteristic voltage of the junction V_c and the characteristic oscillation frequency ω_c . As an example, we report in figure 1.22 the $I(V)$ for a SNS JJ with a multi-layer barrier Cu-Co-Cu-Ni-Cu between two Nb electrodes.

Hysteresis of very small amplitude in $I(V)$ curves for SNS JJs can be due to the heating in the system [20, 21].

The supercurrent properties are close to those in tunnel junctions, even if its sinusoidal trend strictly depends on transmission processes, and not on tunneling processes [10]. The normal branch, on the other hand, is rather different: Andreev reflections produce “pair-quasiparticle” conversion at the interfaces in the high transparencies limit, contributing an *excess current* I_{exc} compared with the normal state [22].

Weak links in magnetic fields A short weak link in the dirty and clean limit presents a Fraunhofer pattern-like $I_c(H)$. We have already described this behavior in section 1.2.2.

Dependence on temperature for a SNS JJ The critical current depen-

dence on temperature in SNS junctions depends on the regime (dirty, clean, ...) and presents differences from the SIS limit.

In the diffusive regime the characteristic voltage $V_c(T)$ for a short weak link follows the AB relation 1.81 for $T \sim T_c$, while at zero temperature the maximum value is

$$V_c(0) = 1.32 \frac{\pi}{e^*} \Delta(0), \quad (1.87)$$

which is 32% greater than $V_c(0)$ for SIS junctions. This is the important result of the *first Kulik and Omel'yanchuk theory*, or KO1 theory [10].

In the frame of this model, K.K. Likharev has evaluated the barrier length effect on the $I_c(T)$ curves [10]: when the dimensionless length l ,

$$l = \frac{L}{\xi_N^D}, \quad (1.88)$$

increases, the critical current gradually assumes an exponential decay at T_c (figure 1.23 (b)).

In the clean limit, instead, the characteristic voltage of the junction at $T = 0$ reaches its upper value in

$$V_c(0) = \frac{2\pi}{e^*} \Delta(0). \quad (1.89)$$

This is the result of the *second Kulik and Omel'yanchuk theory*, or KO2 theory [10].

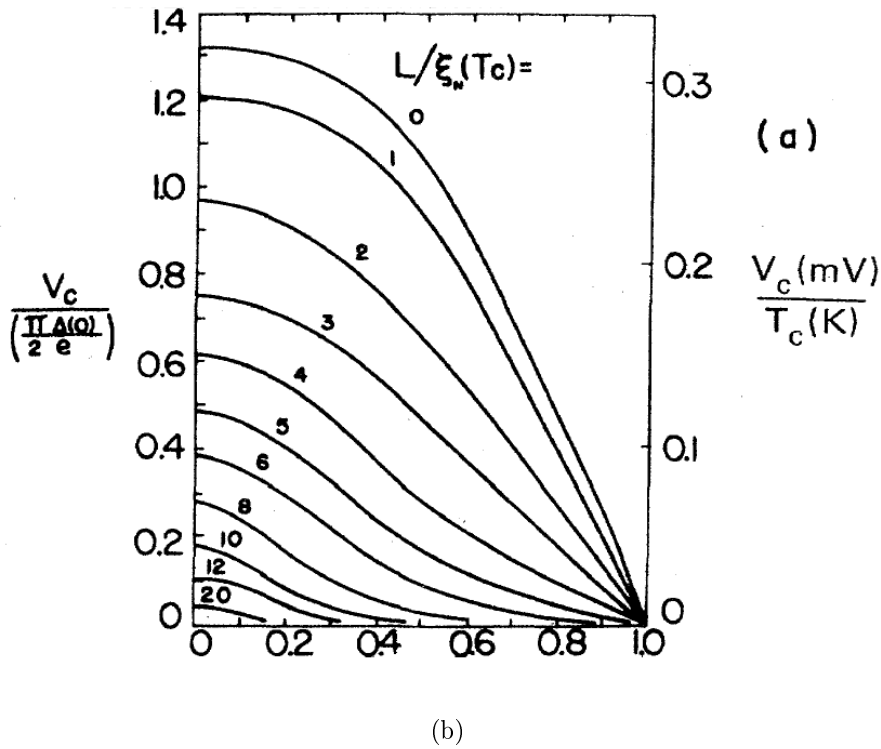
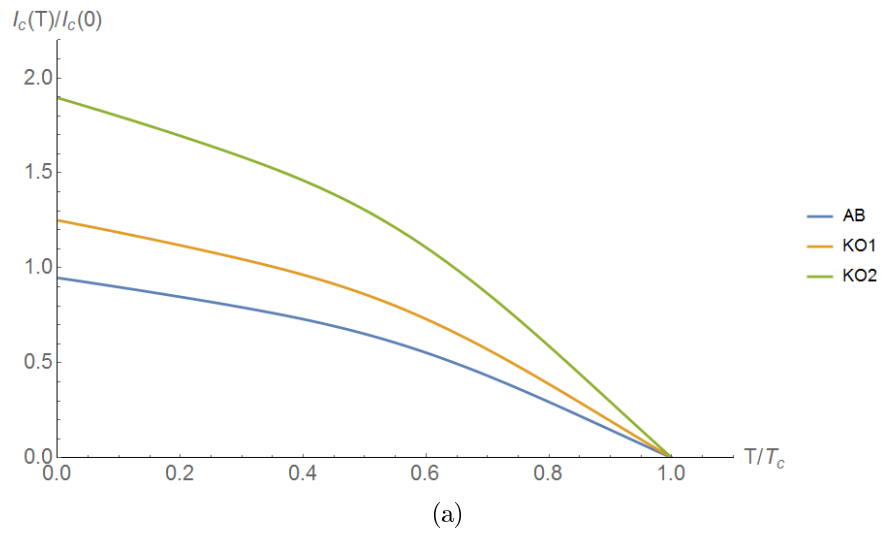


Figure 1.23: In (a), we present a comparison between the normalized current vs. the normalized temperature in the AB relation, and the two corrections for short weak link in the dirty and clean limits (*Mathematica11* simulations); in (b), we report the critical current $I_c(T)$ for different dimensionless thicknesses [10].

Chapter 2

SFS and SIFS junctions

The interplay between two materials with different ordered phase, like superconductors and ferromagnets, is still an unexplored field of the theoretical and experimental physics. Only in the last years, a new class of Josephson junctions composed of ferromagnetic barriers between superconducting electrodes have been implemented: the *SFS junctions*.

These devices have been proposed as building blocks for quantum computing, like RAM (Random Access Memory) [23] or interconnections between superconducting multi-chip modules [24], but apart from possible practical applications, these junctions allow to understand how superconductivity and ferromagnetism can co-exist in the same system, and what kind of new physics can generate [25, 26, 27].

Let us first introduce some notions on ferromagnetic material, so that we can understand why superconductivity and ferromagnetism in bulk structures are in strong competition. After that, we report the most important physical processes of SF heterostructures, and the theoretical predictions on SIFS JJs.

2.1 Ferromagnetic barriers

Ferromagnetic materials are characterized by a spontaneous magnetization M due to the magnetic momentum orientation, which vanishes above a critical temperature known as *Curie temperature* T_{Curie} , at which the ferromagnet

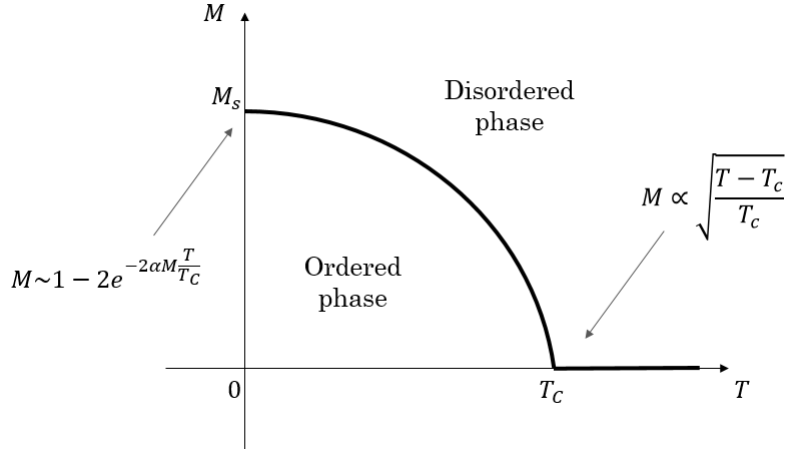


Figure 2.1: Magnetization versus temperature including high and low temperature limits

becomes a paramagnet, i. e. it enters in a *magnetically disordered phase* (figure 2.1). In Weiss mean field theory, in fact, the magnetization in the SI system of a given material

$$\mathbf{M} = \mu_0 \mathbf{B} - \mathbf{H} \quad (2.1)$$

is the ferromagnet-paramagnet transition order parameter. It has the self-consistent expression

$$M(T) = \frac{N}{V} \mu_B \tanh \left(\frac{1}{k_B T} \frac{M V Z}{N \mu_B} \frac{J}{2} \right), \quad (2.2)$$

where N is the total spin number, V is the ferromagnet volume, Z is the coordination number, μ_B is the Bohr magneton and J is the coupling constant equal for all spin pairs [28].

The magnetization as a function of the magnetic field is hysteretic, as reported in figure 2.2. Initially, the magnetization is zero in absence of magnetic fields. Turning the field on, the magnetization follows the *first magnetization curve* and saturates at the *saturation field* H_s . Retracing back the magnetic field, the magnetization follows a different curve and becomes zero when the magnetic field reaches a value known as *coercitive field* $-H_c$ [29].

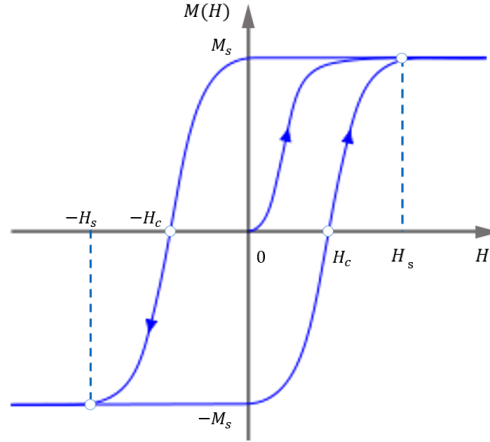


Figure 2.2: Magnetization hysteresis loop

Then, it saturates at negative values in $-H_s$. Finally, when the magnetic field becomes positive, the magnetization is zero at H_c and saturates in H_s .

The final result is a hysteretic loop that depends on the the direction of the spontaneous magnetization with respect to the crystallographic axes, the coercitive fields and the saturation magnetization values, and gives a footprint of the chemical make-up and the crystallographic nature of a ferromagnet [29].

2.2 Superconducting ferromagnets

Let us consider a ferromagnetic superconductor with a ground state consisting of Cooper pair singlets with wave vector $q = 0$, subjected to an applied magnetic field. According to the BCS theory, the superconductor spin structure is not affected until the exchange field energy is sufficiently strong to flip one spin of the singlet and break the Cooper pair, thus destroying superconductivity. This effect, known as *paramagnetic-effect*, occurs at a critical magnetic field value H_P at $T = 0$ K, found from a comparison of the energy gain due to spin polarization in normal state and the energy gain due to the BCS pairing energy,

$$H_P(0) = \frac{\Delta(0)}{\sqrt{2}\mu_B}; \quad (2.3)$$

this is the *Chandrasekar-Clogstone limit* [30].

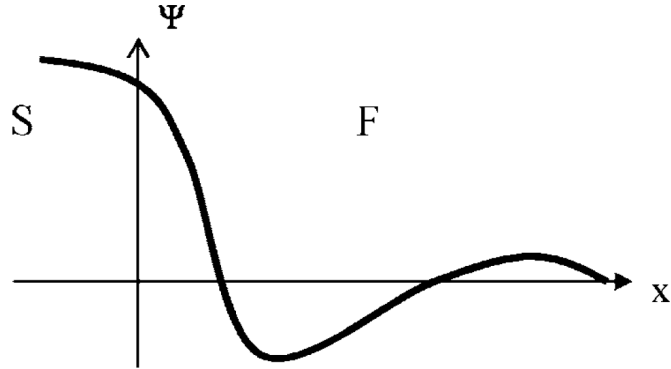


Figure 2.3: Order parameter in the FFLO state

If instead one considers the normal, metallic state at the same finite magnetic field, then the exchange field energy leads to different Fermi surfaces for spin-up and spin-down electrons, which can lead to superconducting pairing where Cooper pair singlets have a finite center-of-mass momentum $q = 2\mu_B H/v_f$, corresponding to the displacement of the two Fermi surfaces [19]. Fulde, Ferrell, Larkin and Ovchinnikov predicted in the frame of this model the appearance of a non-uniform superconducting state with a sinusoidal modulation of the superconducting parameter with the non-zero wave vector q at the scale of superconducting coherence length ξ_s , known as *FFLO state* [19] (figure 2.3).

Experimental confirm of the FFLO state has been searched first in thin films and later in exotic superconductors such as heavy fermions [31] and organic superconductors [32], but it is hard to single out this effect in bulk structures [19].

On the contrary, the observation of a FFLO state has recently become possible due to the great progress in the preparation of high-quality hybrid SFS systems, because the interplay between superconductivity and magnetism occurs at the nanoscale range of layer thicknesses.

2.3 SFS junctions

The JJ footprint is certainly given by the voltage-current characteristic and the critical current dependence on the applied magnetic field. Our purpose is to report the fundamental results about the characteristic behavior of a SFS junction.

2.3.1 Voltage-current characteristics

The $I(V)$ curves are very similar to those observed in SNS junctions (section 1.3): concerning the ferromagnet conducting behavior, in fact, we can observe most of all metallic conductance even when a ferromagnetic structure is composed of non-metallic compounds¹, or at least semiconducting behavior [33].

The voltage-current characteristics are typically non-hysteretic, or slightly hysteretic, as in overdamped junctions described in section 1.2.1. Moreover, in SFS JJs critical currents and normal resistances are smaller than that observed in SIS JJs (table 1.1), so that the characteristic voltage of the junction is of the order of few μV [34].

In order to increase the characteristic voltage of a Josephson junction with a ferromagnetic barrier one typically adds an insulating layer near one of the electrodes: these junctions are called *SIFS JJs*, but we do not focus our attention on this topic further [34].

2.3.2 SFS junctions in magnetic fields

The most important difference between the $I_c(H)$ measured for a tunnel junction and a SFS JJ is the hysteretic nature of the SFS Fraunhofer pattern.

The characteristic Fraunhofer pattern-like $I_c(H)$ is horizontally shifted because of the residual magnetization of the ferromagnetic barrier (figure 2.4):

- by increasing the magnetic field from zero to a positive value we first observe a curve associated to the first magnetization curve and we will

¹For example, transition ferromagnets are typically metals and Heusler compounds can theoretically be half-metallic [33].

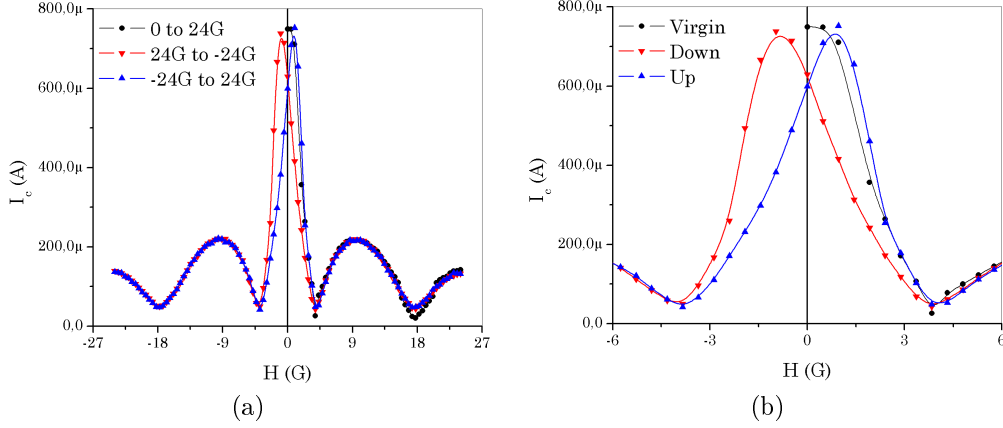


Figure 2.4: In (a), long-range $I_c(H)$ curves in a SI(S)FS junction Nb-Pd_{0.99}Fe_{0.01}-AlO_x-Nb measured at $T = 5.5$ K; in (b), zoom on the curves for small magnetic fields (the line is only a guide for the eye)

refer to it as *virgin curve*, because no magnetic flux is trapped into the F interlayer;

- by decreasing H from positive to negative values, the maximum critical current is shifted to negative values of the magnetic fields; we can refer to this curve as *down curve*;
- by increasing H from negative to positive values, the maximum critical current is shifted to positive values of the magnetic fields; we can refer to this curve as *up curve*.

The hysteretic nature of the pattern is the first motivation for which these junctions can be used as cryogenic RAM [34]. An example of such a $I_c(H)$ is showed in figure 2.4 for a SI(S)FS junction², mentioned in section 2.3.1.

2.3.3 π -junctions and ϕ -junctions

The damped oscillatory behavior of the superconducting order parameter and the presence of an FFLO state in SFS heterostructures (figure 2.5) causes

²The letter S in parenthesis represents a thin superconducting layer leftover from the fabrication processes.

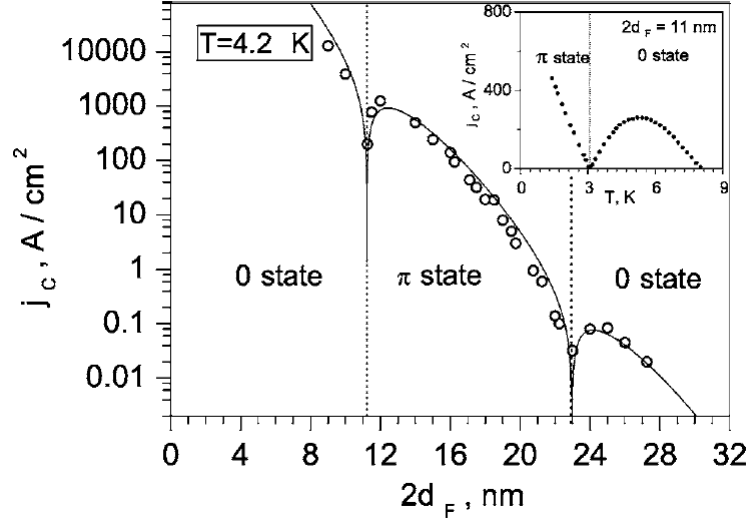


Figure 2.5: Critical density current J_c at $T = 4.2$ K of $\text{Cu}_{0.47}\text{Ni}_{0.53}$ junctions as a function of the F layer thickness. Since the measured J_c is always taken positive, the function $J_c(t)$ presents an evident cups when it changes its sign. In the inset, $J_c(T)$ for a similar junction with ferromagnetic barrier thickness of 11 nm [19].

commensurable oscillations in the critical current by changing the thickness of the barrier [19].

If the ferromagnetic barrier thickness is comparable with the characteristic superconducting correlation decay length in the ferromagnet ξ_f

$$\xi_f = \sqrt{\frac{\hbar D_f}{2\pi h}}, \quad (2.4)$$

where h is the exchange energy and D_f is the diffusion coefficient in the ferromagnet, the pair wave function may cross zero at the center of the F layer with an opposite sign, which means a π shift of the phase of the superconducting order parameter in the adjacent S layer. This interesting phenomenon is related to *spin-flipping* processes that could dominate direct tunneling, and it indicates the transition from the 0 to the π state [19], which is the reason why we call these devices π -junctions.

A 0 to π transition is not clearly identified by $I(V)$ measurements, but it is

possible that a 0 to π phase transition occurs in the system when the critical currents does not go to zero because of higher harmonics in the current-phase relation, or CPR. Up to the second order, for example, one can write the CPR as

$$I_s(\varphi) = I_{c1} \sin \varphi + I_{c2} \sin(2\varphi), \quad (2.5)$$

so that the critical current is a linear combination of I_{c1} and I_{c2} : even if I_{c1} vanishes, it remains finite [36].

We can distinguish two different cases:

- if the ratio I_{c2}/I_{c1} is positive and the first harmonic changes its sign by varying control parameters like the temperature or the ferromagnetic barrier thickness, one can observe a 0 to π transition;
- if the I_{c2}/I_{c1} is negative, the phase of the superconduction state changes *continuously* passing all values between 0 and π , and two critical currents corresponding to values $-\phi$ and ϕ of the phase difference can be measured (figure 2.6). These junctions are the so called ϕ -junctions [35].

The ϕ -JJs were first implemented by Sickinger et al. [37]: they combined a 0-JJ and a π -JJ to achieve a junction with a current-phase relation with a non-vanishing second order term; measured $I(V)$ curves presented in the work are showed in figure 2.6.

The presence of two different switching currents in ϕ -junctions is an attribute of the phase particle dynamics in the system. The washboard potential in presence of a second harmonic is,

$$U(\varphi) = E_{c1} \left(1 + \frac{g}{2} - \cos \varphi - \frac{g}{2} \cos(2\varphi) \right), \quad (2.6)$$

where $g = I_{c2}/I_{c1}$. One can observe that for $g < 0$, the phase particle can be trapped in the ϕ -well or in the $(\phi + \pi)$ -well. When the particle escapes from the ϕ -well, one observes the higher mean switching current, while if it escapes from the $(\phi + \pi)$ -well, one observes the lower switching current (figure 2.7).

On the other hand, it is evident that when $g > 0$, maxima and minima in the washboard potential are inverted with respect to the previous case:

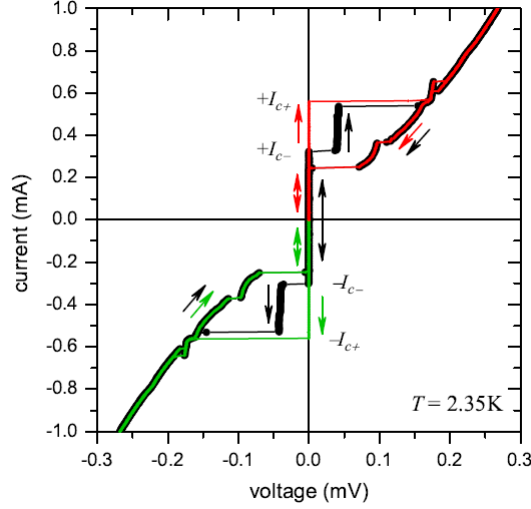


Figure 2.6: Current-voltage characteristics measured at $T \sim 2.35$ K: at this temperature the behavior is deterministic, because if one sweeps from a negative voltage to a positive one, always one observes $\pm I_c^-$, while if one sweeps in a positive voltage range or negative, one measures $\pm I_c^+$ [37].

the phase particle is usually trapped in the lower potential well, and a higher critical current can be observed only in the case of low damping, very unusual for SFS JJs, which typically fall in the overdamped regime.

Let us study the quality factor and the damping for a non-negligible second harmonic. In presence of a non-negligible second harmonic the junction plasma frequency ω_P in the S state can be expressed as a function of g ,

$$\omega_P(g) = \left(\frac{1}{a(g)^2} \right)^{1/4} \sqrt{\frac{e^* I_c}{\hbar C}}, \quad (2.7)$$

where e^* is the Cooper pair charge, and $a(g)$ is the correction

$$a(g) = \sqrt{\frac{\sqrt{32g^2 + 1} + 3}{2\sqrt{32g^2 + 1}}}; \quad (2.8)$$

as a consequence, also the quality factor Q ,

$$Q(g) = \omega_P(g) R_0 C, \quad (2.9)$$

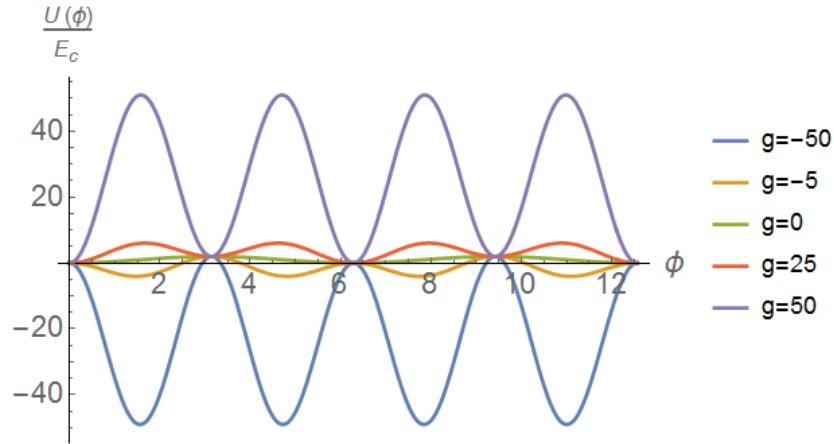


Figure 2.7: Normalized washboard potential in presence of a second harmonic for different g values: *Mathematica11* simulations

depends on g [38], determining the phase diagram for positive g in figure 2.8. Below the $Q(g)$ curve only one critical current appears, while beyond the curve one typically observes two critical currents.

2.3.4 Triplet current in SFS JJs

As in the SNS junctions, in SFS heterostructures a supercurrent can flow because of the *proximity effect*, and can be properly expressed by the Andreev reflections (figure 1.21 in section 1.3). However, we had to clarify that in a SFS junction spin effects play an important role: an incident spin-up electron is reflected by the interface as a spin-down hole, to have as a result a Cooper pair of electrons with opposite spins in the superconductor [19].

Since both the spin-up and spin-down bands of electrons in a ferromagnet are involved in the conduction, the spin-polarization P becomes a very important parameter: because of the spin-channel selection performed by the magnetic barrier, the singlet Cooper pair current is strongly suppressed when compared with equivalent tunnel barriers, and totally suppressed in fully spin-polarized barriers.

In some works, however, it has been predicted that the rapid spatial decay of the supercurrent would not occur if *spin triplet superconductivity* is induced in the ferromagnetic barrier [39]. A long-range proximity effect

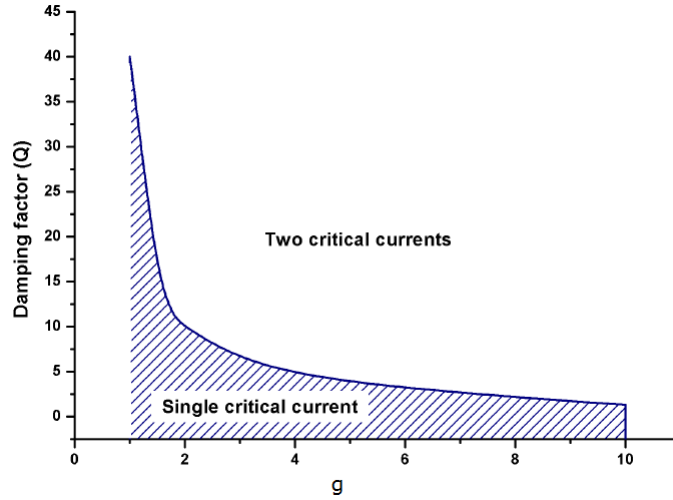


Figure 2.8: Damping factor phase-diagram [38]

arises when the F layer magnetization is strongly inhomogeneous, because the exchange field in a non-collinear magnetic configuration does not influence the components with spin projections $s_z = \pm 1$ [39].

2.3.5 Higher harmonics in CPR for SFS JJs

A possible triplet superconduction state has parallel spins $|\uparrow\uparrow\rangle$ ($|\downarrow\downarrow\rangle$), as suggested by H. Meng et al. [40].

C. Richard et al. predicted in this frame that coherent propagation of two parallel-spin triplet pairs with opposite spin directions can be observed when a superharmonic contribution of the second order dominates the current-phase relation [41]; the critical current I_{c2} is proportional to $1 - P^2$, with P spin-polarization. According to this prediction, the effect should be robust for intermediate spin-polarization.

2.4 SIFS junctions

Each effect described in section 2.3 has so far been limited to systems containing metallic ferromagnets. In collaboration with the Materials Science and Metallurgy Department of Cambridge (UK), we have derived a full char-

acterization of an innovative class of Josephson junctions, known as *SIFS junctions*.

The analysis of these interesting heterostructures allows to find further information about unconventional superconductivity processes like a pure second harmonic term in the CPR relation [42, 43] and the triplet superconductivity [44].

Let us expose the most important features of a SIFS JJ, which will be the main topic of the next sections:

- junctions with ferromagnetic insulator barriers (If), while keeping most of the functionalities of a SFS, fall in the underdamped regime, so that they have the advantage to be promising low-dissipation devices [43];
- these junctions act like *spin-filters*, and they could show a predominant second harmonic in the CPR in presence of spin-filtering efficiency of about 80 – 90% [42];
- the temperature dependence of the characteristic voltage $V_c(T)$ and the Fraunhofer patterns could be strongly modified by the presence of the insulating ferromagnetic barrier [44].

We will concentrate our attention on the physical properties of the GdN barrier.

2.4.1 Spin-filtering

Because of the existence of the finite gap between the conduction band and the valence band of an insulating barrier, electron transport can only take place through quantum mechanical tunneling; the conductance in the junction can be written as

$$\sigma \propto e^{-\frac{2t}{\hbar}\sqrt{2mE_0}}, \quad (2.10)$$

because the electrons tunnel probability is exponentially dependent on the tunnel barrier height and thickness.

When the material goes through its ferromagnetic transition, however, the presence of exchange interactions leads to a spin asymmetry for the two

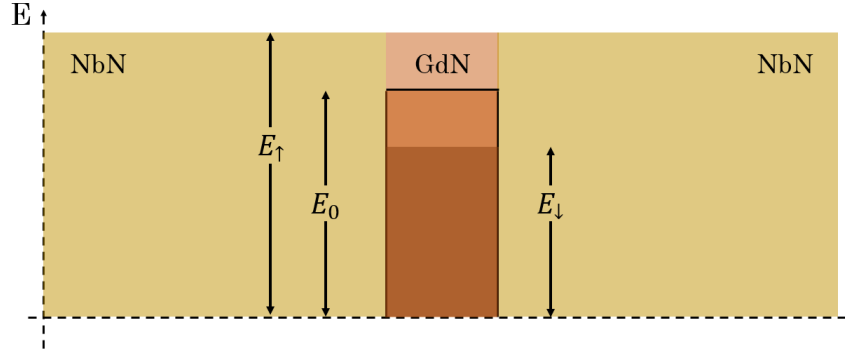


Figure 2.9: Scheme of the barrier encountered by the carriers in a spin-filter device, like our Josephson junction NbN-GdN-NbN

spin channels: electrons of different spins, in fact, experience different barrier heights

$$\begin{cases} E_{\uparrow} = E_0 - \frac{h}{2} & \text{for spin } \uparrow \\ E_{\downarrow} = E_0 + \frac{h}{2} & \text{for spin } \downarrow, \end{cases} \quad (2.11)$$

where h is the ferromagnet exchange field, and the tunneling current acquires a substantial spin polarization, so that these materials are termed *spin-filters* due to the active spin selectivity of the tunneling process [46] (figure 2.9).

We will deduce indirectly the *spin-filtering efficiency* P through the temperature dependence of the tunnel resistance across a spin filter, using the approach and the approximated formula by Senapati et al. [46],

$$P \sim \tanh \left(\cosh^{-1} \left(\frac{R^*}{R} \right) \right), \quad (2.12)$$

where R^* is the resistance that the junction would have if it acts like a non-spin-filter junction and R is the effective one. This expression for P is obtained by defining it as

$$P = \left| \frac{\sigma_{\uparrow} - \sigma_{\downarrow}}{\sigma_{\uparrow} + \sigma_{\downarrow}} \right|, \quad (2.13)$$

where the conductance per spin follows the same rule as in equation 2.10.

The spin-filtering efficiency, in fact, can be written as

$$P = \left| \frac{e^{-x\sqrt{1-\eta}} - e^{-x\sqrt{1+\eta}}}{e^{-x\sqrt{1-\eta}} + e^{-x\sqrt{1+\eta}}} \right|, \quad (2.14)$$

where x is the dimensionless thickness

$$x = \frac{2t}{\hbar} \sqrt{2mE_0}, \quad (2.15)$$

and η is the dimensionless barrier energy

$$\eta = \frac{h}{2E_0}. \quad (2.16)$$

In the hypothesis of exchange fields smaller than the barrier height E_0 , i. e. for $\eta \rightarrow 0$, an expansion in Taylor series leads to

$$P \sim \left| \frac{e^{x\eta/2} - e^{-x\eta/2}}{e^{x\eta/2} + e^{-x\eta/2}} \right| = \left| \tanh \left(\frac{x\eta}{2} \right) \right|. \quad (2.17)$$

Let us now demonstrate that $x\eta/2$ corresponds to $\cosh^{-1}(R^*/R)$ in equation 2.12. The ratio R^*/R in terms of the conductivities is

$$\frac{R^*}{R} = \frac{\sigma_{\uparrow} + \sigma_{\downarrow}}{\sigma}. \quad (2.18)$$

As a consequence, we obtain for $\eta \rightarrow 0$,

$$\frac{R^*}{R} = \frac{e^{-x(1-\frac{\eta}{2})} + e^{-x(1+\frac{\eta}{2})}}{e^{-x}}, \quad (2.19)$$

which leads to

$$\frac{R^*}{R} \sim \cosh \left(\frac{x\eta}{2} \right). \quad (2.20)$$

We will see that the analyzed devices acquire a spin-polarization from a certain value of the barrier thickness: from this onset, we name a SIFS junction as *spin-filter* (chapter 4).

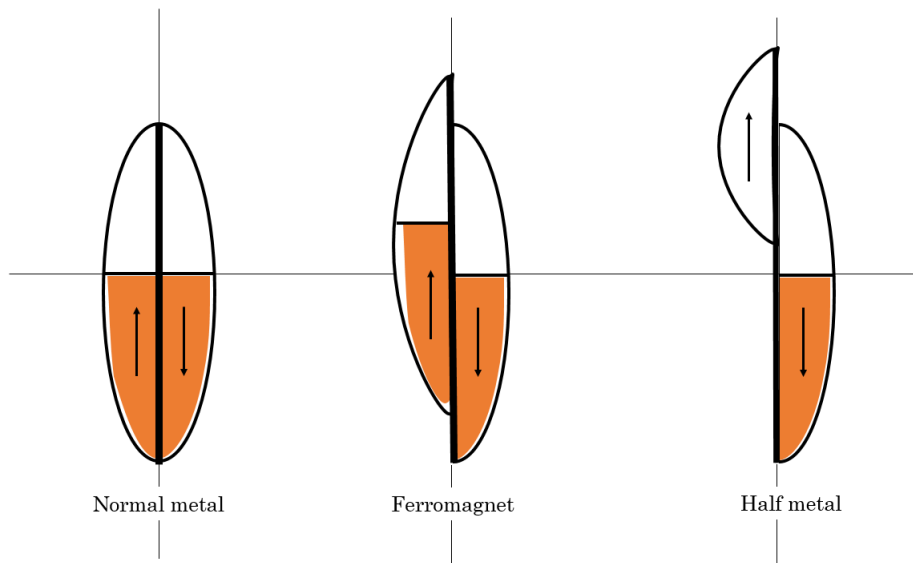


Figure 2.10: Band structures for a normal metal, a ferromagnet and a half metal

2.4.2 Gadolinium Nitride barriers

In this work, we analyze SIFS JJs with a GdN barrier, for which band structure calculations with density functional theory predict a transition from a semiconductor in the paramagnetic phase to a semimetal in the ferromagnetic phase [2]. For one spin channel only semimetallic overlap might occur; the barrier could be a half metal (figure 2.10) with complete spin polarization, and this is why the compound will be of considerable interest for application in spin-filtering devices [47].

The ordered magnetism of GdN originates from the large local spin magnetic moments of the half filled Gd $4f$ -shell coupled by an indirect interaction [48], and strictly depends on stoichiometry, impurities and lattice defects [49]; by increasing the N-fraction, the saturation magnetization M_s decreases, and vice versa. Also the coercive field H_c decreases when the N-fraction increases [50]. According to this, Senapati et al. proposed that different nitrogen concentration correspond to different transport properties [51].

It is not easy to define the GdN electronic structure experimentally because of the difficulties correlated to the sample preparation, so we will talk

about “insulating barrier” because we verified with $I(V)$ measurements that our devices present an underdamped characteristic as in SIS JJs (chapter 4).

Because of internal strain and pressure, also an increase of the lattice parameter of the GdN layers can occur; the most distinct effect visible on the macroscopic magnetic properties resulting in these variations is the reduction of the Curie temperature from $T_{\text{Curie}} = 69$ K [2] in a bulk to nearly 30 K in a GdN film [49].

2.4.3 Second harmonics in CPR

A. Pal et al. observed that SIFS junctions with a GdN barrier and a spin-filtering efficiency of about 80% present hysteretic Fraunhofer patterns with half the expected period, according to the presence of higher harmonics [42].

We will report a simple model due to E. Goldobin that allows to comprehend the effect of a second harmonic in the Fraunhofer patterns [36].

Let us consider a phase linear in the magnetic field

$$\varphi(x) = h\pi x + \varphi(0), \quad (2.21)$$

where h is

$$h = \frac{H_y 2d_m}{\phi_0^*}, \quad (2.22)$$

as in equation 1.62, where d_m is the appropriate magnetic spacing (see section 1.2.2). In order to get the current in terms of h , we have to integrate on the surface of the junction the supercurrent density in presence of a second harmonic,

$$J(x, h, \varphi(0)) = J_{c1} \sin(h\pi x + \varphi(0)) + J_{c2} \sin(2h\pi x + 2\varphi(0)), \quad (2.23)$$

or, in terms of the ratio $J_{c2}/J_{c1} = g$,

$$J(x, h, \varphi(0), g) = J_{c1} (\sin(h\pi x + \varphi(0)) + g \sin(2h\pi x + 2\varphi(0))). \quad (2.24)$$

We get with simple calculations

$$I(h, \varphi(0), g) = \frac{2I_{c1}}{\pi hL} \left(\sin(\pi hL/2) \sin(\varphi(0)) + \frac{g}{2} \sin(\pi hL) \sin(2\varphi(0)) \right), \quad (2.25)$$

where $\pi hL/2 = \pi\Phi(H)/\phi_0^* = \pi\eta$.

The maximum value of the normalized critical current as a function of the dimensionless magnetic field can be found by maximizing with respect to $\varphi(0)$ the quantity $I(h)/I_{c1} = i(h)$. The values for which the supercurrent is maximum are

$$\cos(\varphi_+(0)) = \frac{-1 + \sqrt{1 + 32g^2 \cos^2(\pi\eta)}}{8g \cos(\pi\eta)} \quad (2.26)$$

$$\cos(\varphi_-(0)) = \frac{-1 - \sqrt{1 + 32g^2 \cos^2(\pi\eta)}}{8g \cos(\pi\eta)}, \quad (2.27)$$

so that in principle we get two different branches for the critical current dependence on the magnetic field,

$$i_+(\eta, \varphi(0), g) = i(\eta, \varphi_+(0), g) \quad (2.28)$$

$$i_-(\eta, \varphi(0), g) = i(\eta, \varphi_-(0), g), \quad (2.29)$$

which satisfy the condition:

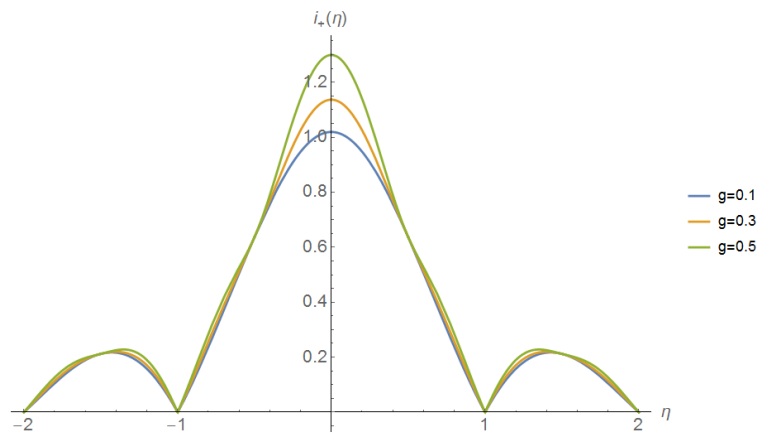
$$i_{\pm}(\eta, g) = i_{\pm}(\eta, -g), \quad (2.30)$$

i. e. the Fraunhofer pattern analysis can not allow to define the sign of the second harmonic term, a possible 0 to π transition or if the analyzed junctions are ϕ -JJs.

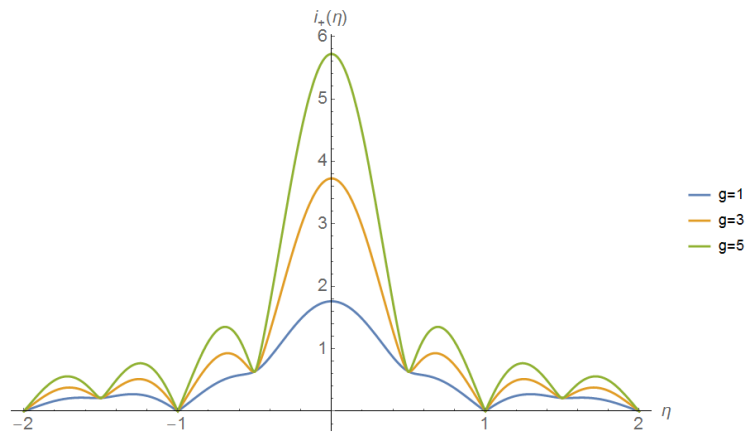
The two critical current follow a Fraunhofer pattern behavior if $\cos(\varphi_{\pm}(0))$ satisfies the condition

$$|\cos(\varphi_{\pm}(0))| \leq 1. \quad (2.31)$$

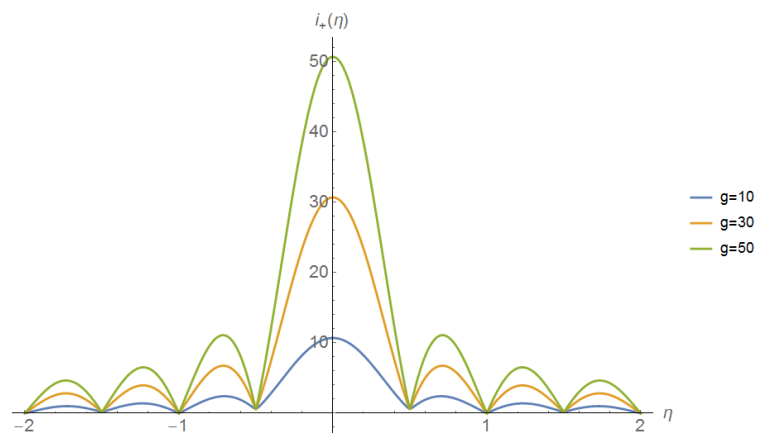
As a consequence, we will concentrate our attention on the $i_+(\eta, g)$ branch, because $|\cos(\varphi(0)_+)|$ certainly satisfies the condition in equation 2.31 for very different values of g .



(a) $g = 0.1, 0.3$ and 0.5



(b) $g = 1, 3$ and 5



(c) $g = 10, 30$ and 50

Figure 2.11: Simulated Fraunhofer patterns with *Mathematica11* in presence of a non-negligible second harmonic for different values of g

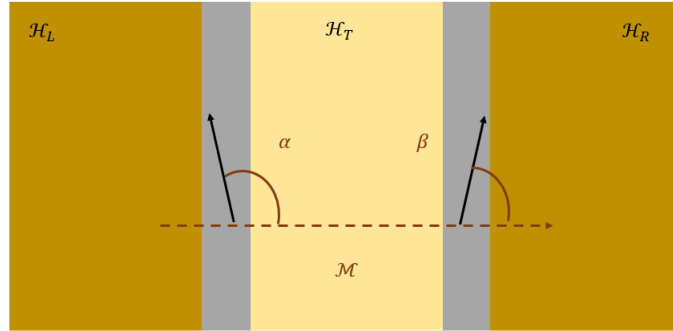


Figure 2.12: SIFS junction model in the Bergeret theory [44]

For values of $g < 1/2$, one typically find a Fraunhofer pattern with the maximum at zero field greater than that in a conventional junction because of the second harmonic contribution (figure 2.11 (a)). Once we exceed this threshold, however, also the minima in the pattern change: in fact, for g very high, we can observe a Fraunhofer pattern with half the expected period (figure 2.11 (c)).

2.4.4 Josephson triplet currents in SIFS JJs

According to the work of C. Richard et al., the presence of a predominant second harmonic in the CPR relation for a SFS JJ leads to a non-zero Josephson triplet current, i.e. a dissipationless spin-polarized current, very appealing in the field of spintronics [41].

It was predicted by F.S. Bergeret et al. that also in SIFS junctions one can observe a non-zero Josephson triplet current [44], but the presence of higher harmonics term is not considered.

They modeled the device with a tunnel spin-filter barrier between two superconducting electrodes; the exchange field was introduced with the insertion of two thin ferromagnetic layers near the electrodes. In this way, one can describe the system with a generic Hamiltonian homogeneous in space

$$\mathcal{H} = \mathcal{H}_L + \mathcal{H}_R + \mathcal{H}_T, \quad (2.32)$$

where the left and right electrodes are modeled by a BCS Hamiltonian ($\mathcal{H}_{L(R)}$),

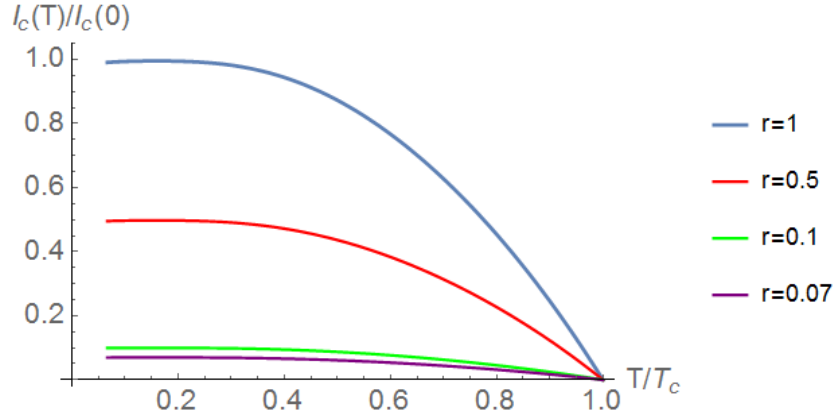


Figure 2.13: Normalized critical current $I_c(T)/I_c(0)$ vs. the normalized temperature T/T_c for exchange field $h = 0$, and $\alpha = \beta = \pi/2$: *Mathematica11* simulations

and the tunnel Hamiltonian (\mathcal{H}_T) takes into account not only a spin-independent tunneling matrix \mathcal{T} as in a conventional insulating barrier, but also a spin-dependent tunneling matrix \mathcal{U} , due to an intrinsic exchange field (figure 2.12).

In the hypothesis of equal energy gaps ($\Delta_L = \Delta_R = \Delta$) in the two superconductors, and equal exchange fields ($h_L = h_R = h$), the characteristic voltage of the junction can be written as

$$V_c(T) = \frac{2\pi T}{e} \sum_{\omega_n > 0} (r (f_s^2 + f_t^2 \cos \alpha \cos \beta) + f_t^2 \sin \alpha \sin \beta), \quad (2.33)$$

where r is a parameter linked to the spin-filtering efficiency P , $f_{s(t)}$ are the anomalous Green's functions, ω_n are the Matsubara frequencies and α and β are the angles that the exchange fields form with the magnetization of the barrier. Let us analyze these factors.

The parameter r can be written in terms of the tunneling amplitude for spin up and down $T_{\uparrow(\downarrow)}$,

$$T_{\uparrow(\downarrow)} = \mathcal{T} \pm \mathcal{U}, \quad (2.34)$$

as

$$r = \frac{2T_{\uparrow}T_{\downarrow}}{T_{\downarrow}^2 + T_{\uparrow}^2}, \quad (2.35)$$

and can be linked to the spin-filtering efficiency P by taking into account

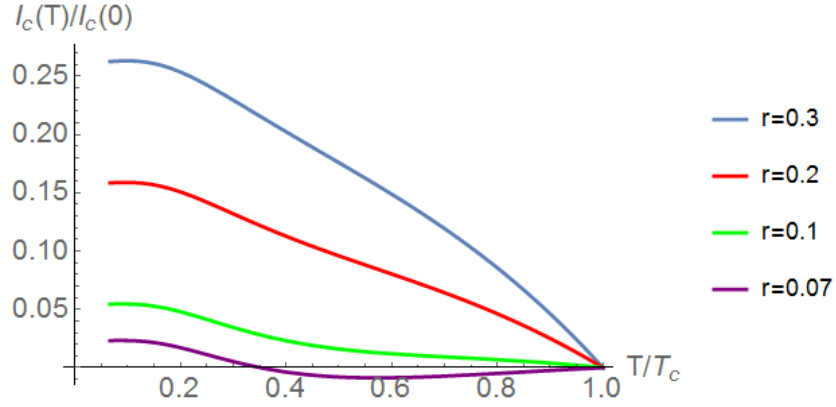


Figure 2.14: Normalized critical current $I_c(T)/I_c(0)$ vs. the normalized temperature T/T_c for exchange field $h = 0.576\Delta(0)$, and $\alpha = \beta = \pi/2$: *Mathematica11* simulations

that P can be expressed as

$$P = \left| \frac{T_{\uparrow}^2 - T_{\downarrow}^2}{T_{\uparrow}^2 + T_{\downarrow}^2} \right|; \quad (2.36)$$

in fact, r assumes the form

$$r = \sqrt{1 - P^2}, \quad (2.37)$$

i. e. it is $r = 1$ for non-magnetic barriers and $r = 0$ for fully-polarized barrier.

The functions $f_{s(t)}$ are a symmetric and asymmetric combination of the anomalous Green functions f_{\pm} ,

$$f_{\pm} = \frac{\Delta}{\sqrt{\Delta^2 + (\omega_n \pm ih)^2}}, \quad (2.38)$$

so that the singlet contribution is represented by the term f_s

$$f_s = \frac{f_+ + f_-}{2}, \quad (2.39)$$

and the triplet one by f_t ,

$$f_t = \frac{f_+ - f_-}{2}. \quad (2.40)$$

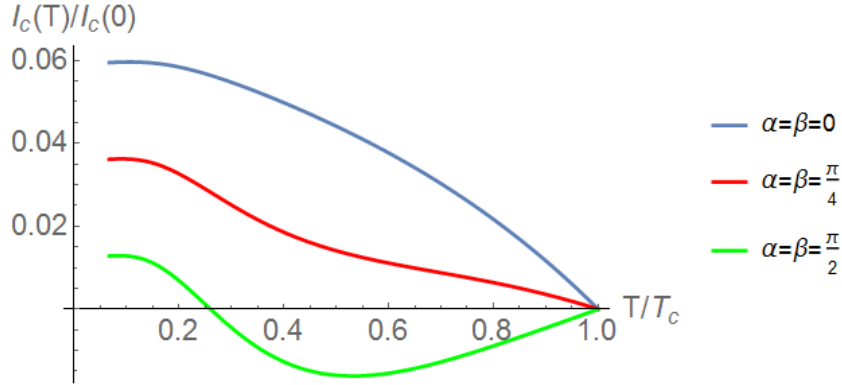


Figure 2.15: Normalized critical current $I_c(T)/I_c(0)$ vs. the normalized temperature T/T_c for $r = 0.06$ and different α and β values: *Mathematica11* simulations

If the exchange field is zero, i.e. in the case of a conventional tunnel junction, the characteristic voltage follows the AB relation multiplied by a factor $r < 1$ (figure 2.13), but when the exchange field starts to become important, the $V_c(T)$ curve behaves in a very different manner from that observed in conventional junctions.

Bergeret et al. demonstrated that a non-collinear magnetic field in the system is necessary to observe a triplet Josephson current; in fact, for α and β different from $k\pi$, with $k \in \mathbb{Z}$, one can study the limit case of a fully-polarized barrier, i.e. for $r = 0$. In this case, the characteristic voltage of the junction reduces to

$$V_c(T) = \frac{2\pi T}{e} \sum_{\omega_n > 0} f_t^2 \sin \alpha \sin \beta, \quad (2.41)$$

so that the only term that contributes to the Josephson current is the triplet component.

The maximum triplet contribution is found for $\alpha = \beta = \pi/2$, for which we plot the normalized critical current versus the normalized temperature for different r values (figure 2.14). As we can observe, the simulated functions differ from the AB behavior when r tends to zero; in particular, for certain r -values we can observe not only a trend different from the AB law, but most

of all one can observe a change in the sign of the critical current and a 0 to π transition.

A comparison between the $I_c(T)/I_c(0)$ versus T/T_c for different α and β values, instead, is showed in figure 2.15 for $r = 0.06$.

Chapter 3

Experimental set-up

This chapter deals with the experimental set-up and the measurements techniques employed in this work to analyze our SIFS junctions in a temperature range from 300 mK to the room temperature. We will especially focus on the description of the cooling system, of the filtering system, of the electronic-rack and of the measurements techniques, which allow to perform high precision and low noise measurements.

3.1 Samples scheme

In this work, we analyze unconventional Josephson junctions with an insulating ferromagnetic barrier, gadolinium nitride GdN (section 2.4.2), between two niobium nitride NbN superconducting electrodes.

Our junctions were fabricated in Materials Science and Metallurgy Department of the University of Cambridge (UK) by optical lithography from trilayer NbN-GdN-NbN films prepared by DC reactive magnetron sputtering at room temperature. We have six sandwiches with different GdN barrier thicknesses (table 3.1).

A 5 nm MgO buffer layer was deposited on a SiO₂ substrates before the deposition of the trilayers, so that it acted as an etch-stop layer for the base 100 nm NbN layer during subsequent lithographic processing of the junctions. The GdN barrier was prepared in an Ar gas atmosphere containing 8% N₂,

Table 3.1: GdN barrier thickness and measured samples

Junction	t_{GdN} (nm)
B	1.50
C	1.75
D	2.00
F	2.50
G	3.00
H	3.50

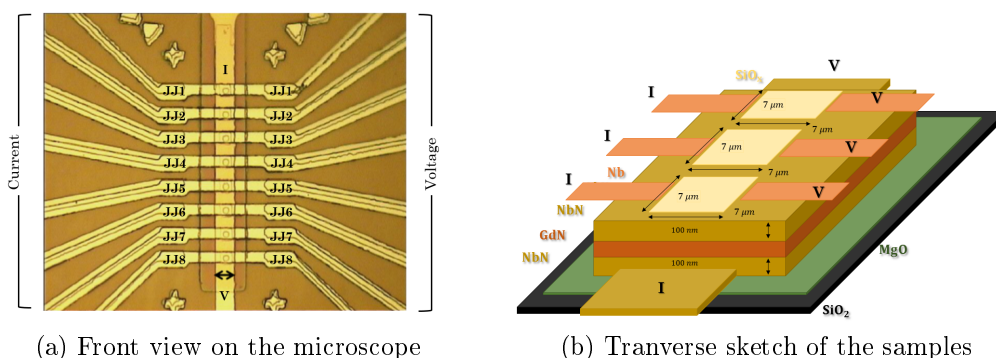


Figure 3.1: In (a): front view of the samples; in (b): transverse sketch of the samples. We show only three junctions characterized by the same GdN thickness, but we remember that we have eight junctions overall.

whereas NbN layers were prepared with 28% N_2 . The junction area, in a square geometry, was defined by selective reactive etching of the top 100 nm NbN layer in CF_4 plasma. The error on the electrodes thickness is ± 10 nm. A layer of sputtered SiO_x was patterned using the lift-off method to provide an electrically isolated contact window on top of the $7 \times 7 \mu\text{m}^2$ junctions. While the NbN base layer acted as the bottom contact, a Nb wiring layer was patterned to achieve the top contact. In figure 3.1, we represent a junction with its typical dimensions and a sample scheme with its contacts.

The fabrication processes implied are still developing and, as a consequence, the physical properties of the junctions strictly depend on the specific samples-run. One-run samples, in conclusion, are required to fully characterize the junctions.

In our case, on the same NbN-GdN-NbN sandwich, there are eight junc-

tions nominally equivalent: in this way, one can make a comparison between two or more junctions with same thicknesses, geometries and fabrication parameters. Moreover, one can ensure that the achieved experimental results depend only on the fundamental physics of the sample, and not on the fabrication processes.

Junctions in the same sandwich showed similar behavior, so we will report only the experimental results about one junction per GdN barrier thickness.

3.2 Cooling System

The study of superconducting phenomena occurs in a temperature range from a few hundred millikelvin up to some degrees kelvin, which is achieved through cryogenic systems.

We used an evaporation cryostat *Oxford Instruments Heliox VL*, immersed into a ^4He bath (figure 3.2). The dewar is composed of an internal chamber 79 cm deep and an external one, which is at very low pressure of about $10^{-5} - 10^{-3}$ mbar that decouples the cryogenic liquid from the environment. The dewar is composed of a first screen of *cryoperm*, a nichel and alluminium alloy, and by a second one in lead, with the aim of protecting from external magnetic fields.

Our cryostat can reach temperatures of about 300 mK exploiting the ^3He condensation, which becomes liquid at 2.2 K at the standard pressure; a decrease in its vapor tension, however, allows to achieve lower temperatures. We succeed in this process by using an adsorption pump composed of a zeolitic material, the *SORB*, active below 30 K. The *SORB* temperature is monitored by a silicium diode thermometer; an increase in temperature is achieved using a heater.

The cryostat core is enclosed in the *inner vacuum chamber*, or IVC, where a 10^{-2} mbar-vacuum is made by a rotative pump *Adixen PASCAL 2015sd*, providing thermal insulation from the environment (figure 3.3). A perfect closing is ensured by the use of grease on IVC edges. The IVC is composed of:

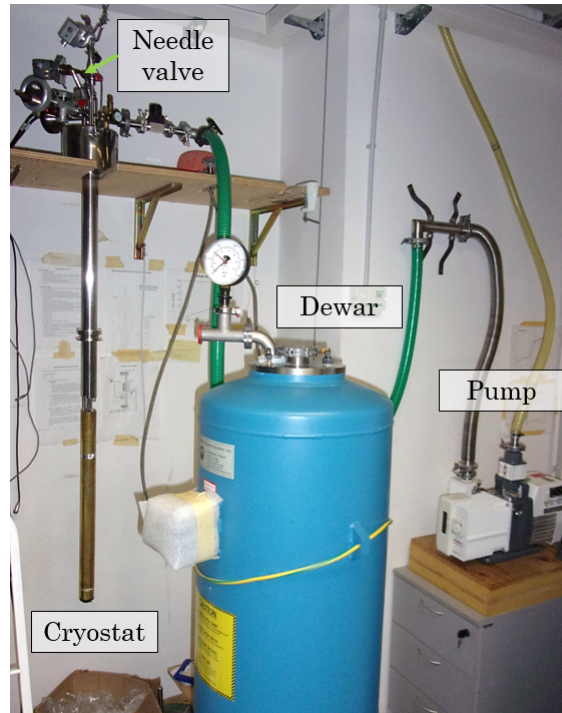


Figure 3.2: View on the experimental set-up in the University of Naples laboratories

- a capillary;
- a pot at 1 K, the *1K-Pot*;
- a pot at 300 mK, the *³He-Pot*;
- a copper sample holder, below the ³He-Pot;
- a niobium-titanium coil thermally anchored to the 1K-Pot and mechanically anchored to the ³He-Pot.

First of all, we immersed the cryostat in the helium dewar ensuring a good thermalisation by the insertion of a small quantity of helium gas in the IVC. After that, the capillary draws liquid ⁴He at 4.2 K from the bath to the *1K-pot*: here a temperature of about 1.8 K is reached by pumping with the external rotative vacuum pump and with a needle valve¹. Finally, the cool-

¹The SORB temperature remains higher than its activation temperature, so that it does not adsorb ³He molecules.

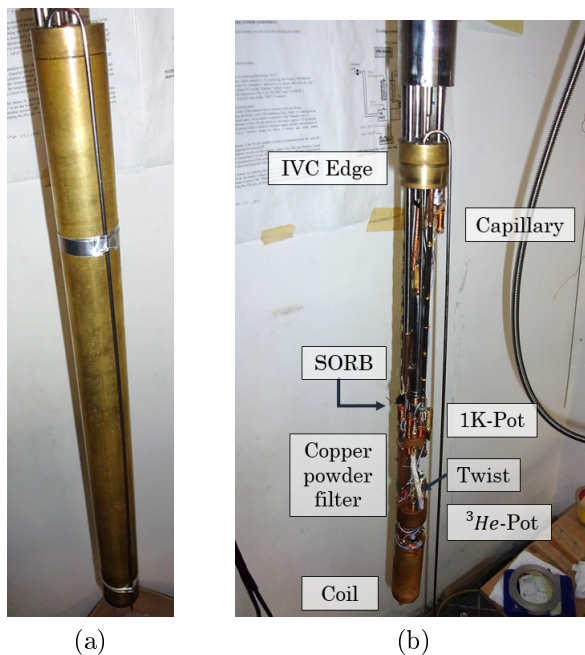


Figure 3.3: View on the IVC and brass screen

down to 300 mK is achieved with the activation of the SORB: we decrease its temperature, so that it starts to adsorb ³He gas and as a consequence we reduce its vapor tension.

The sample is anchored with a silver paste to the copper holder to ensure a good thermal conductivity and it is connected to the electronics with aluminium bonding, using a *K&S 4523 Manual Wire Wedge Bonder*. In particular, to measure $I(V)$ and $R(T)$ curves of superconducting samples and junctions, the four-contact configuration is employed.

The sample is surrounded by a niobium-titanium coil, which is superconducting below a critical temperature of about 10 K. A thermal insulating twist provides thermal contact between the coil and the 1K-Pot, so that the coil is always at about 2 K during measurements and additional Joule dissipation due to the current flow in the coil does not heat the sample stage.

A bias current of 1 A through the coil generates a magnetic field orthogonal to the Josephson supercurrent up to 0.3 T; in particular, previous calibration measurements gave the conversion from the bias current through

the coil I_{coil} in milliamperes to the magnetic field H in gauss:

$$H(\text{G}) = 3I_{\text{coil}}(\text{mA}). \quad (3.1)$$

3.3 Filtering systems and electronics

An accurate measurement of the transport properties of a Josephson junction requires special care to filter electrical and thermal noise. For this purpose, there are two different stages at different temperatures: low pass RC-circuits, known as π -filters, with a cut-off of about 1 MHz have been installed at the 1K-Pot stages; two copper powder filtering stages with typical cut-off frequencies of about 1 GHz have been installed at the 1K-pot stage and at the ^3He -pot stage [52].

Voltage-carrying lines from room temperature electronics to 1K pot are manganine wires, for its low thermal conductivity. The current cables, instead, are copper made, because of its low resistance. From the 1K-Pot to the ^3He -Pot, current-carrying lines are made of niobium and aluminium cables in their superconductive phase. Overall, electrical lines resistance is about $100\ \Omega$ for current-carrying lines and about $200\ \Omega$ for voltage lines [52].

The following instruments are used to perform $R(T)$ and $I(V)$ measurements:

- a temperature controller from *Oxford Instruments ITC530*, connected to the computer and driven by a software in *LabVIEW*, which uses PID, or *Proportional-Integrative-Derivative*, processes to monitor in a wide range of temperatures the ^3He -Pot and the SORB;
- a *LeCroy Wave Runner 6100A* oscilloscope;
- a *SR570 Standard Research Systems* preamplifier;
- a *Agilent 33120A* waveform generator;
- a *EG&G Princeton Applied Research 5210* lock-in amplifier;
- a *Nanovoltmeter Keithley 2182* used in $R(T)$ measurements;

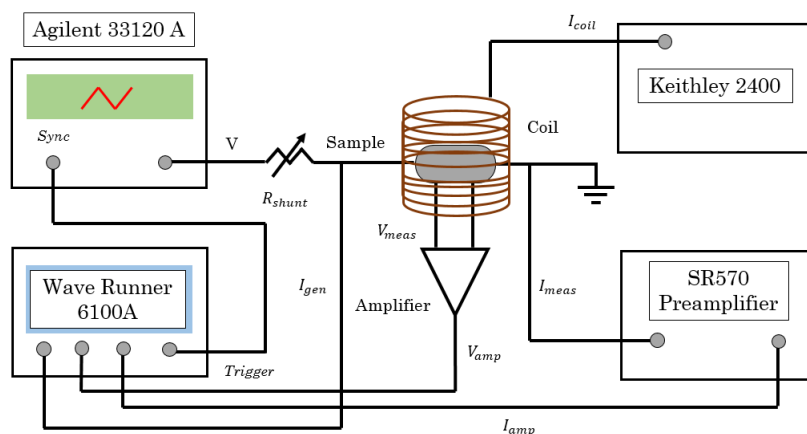


Figure 3.4: Electronic set-up configuration for $I(V)$ measurements

- a *Source Meter Keithley 2400* used as a current generator to produce magnetic fields.

3.3.1 $I(V)$ measurements

In figure 3.4 we show a scheme of the electronic set-up for the $I(V)$ measurements.

As in all measurements on Josephson devices, the junctions are current-biased. The *Agilent 33120A* generates a voltage triangular waveform with a peak-to-peak V_{pp} amplitude at 11.123 Hz, so that the current flowing in the device is

$$I_{\text{bias}} = \frac{V_{\text{pp}}}{R_{\text{shunt}}}, \quad (3.2)$$

where R_{shunt} is the nominal resistance on which the voltage signal falls. The shunt resistance is higher than electrical lines resistance. The error on the generated voltage is $1\%V_{pp}$ from the instrument specifications [53]. We always choose a peak-to-peak amplitude and a shunt resistance in such a way that the bias current is higher than the critical current of our samples.

The voltage signal generated is showed on the oscilloscope *WaveRunner 6100A*, so as the current in the JJ, pre-amplificated by the *SR570 Preamplifier*. The measured voltage drop on the junctions electrodes V is first amplified by an operational amplifier with a 500 gain and later observed on

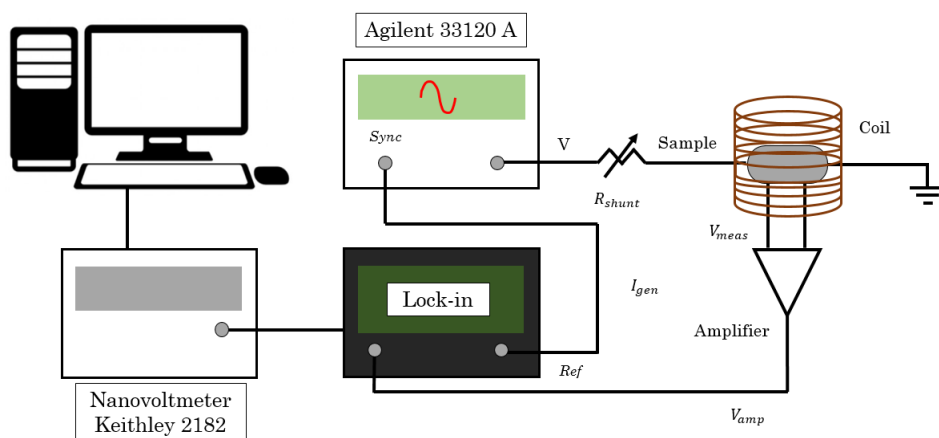


Figure 3.5: Electronic set-up configuration for $R(T)$ measurements

the oscilloscope as average values, properly choosing the number of average sweeps; in particular, in this work we choose 100 number of averages on each channel for all the junctions and 200 number of average sweeps when it was necessary to remove noise effects, i. e. for very small currents. The oscilloscope is connected to the computer, where we saved all the measurements.

3.3.2 $R(T)$ measurements

In figure 3.5 we show a scheme of the electronic set-up for the $R(T)$ measurements.

In $R(T)$ measurements, we generate a sinusoidal waveform with root-mean-squared amplitude $V_{\text{RMS}} = (100 \pm 1)$ mV at 11.123 Hz and the amplified voltage drop between the two superconducting electrodes V is read by the *EG&G Princeton Applied Research 5210* lock-in amplifier; in this way, we can achieve high precision AC measurements. The lock-in, in fact, multiplies the voltage drop on the junction V to the sinusoidal waveform generated V_{RMS} , which is the reference signal, and it integrates their product in a period of 1 s, because the bias currents we use are in the hertz range. The output is a DC signal, because every component that is not at the same frequency of the reference one, or that is an out-of-phase component, is attenuated close to zero.

The output DC voltage signal V_{DC} is read by the *Nanovoltmeter Keithley 2182* and divided by the bias current.

The lock-in allows also to measure the phase difference $\Delta\phi$ between the voltage drop on the junction V and the reference signal V_{pp} ; we required a $\Delta\phi \sim 0$ or π , because this value typically ensures a non-capacitive coupling in the sample, which could be due to dishomogeneities or non-metallic contacts.

3.3.3 Measurements in magnetic fields

In the measurements in magnetic field the source meter *Keithley 2400* generates a current I_{coil} through the coil, so that a magnetic field parallel to the junction surface is produced. The error on the generated current is $0.012\%I_{\text{coil}}$, as declared in the instrument specifications [54].

In a first moment, we applied a magnetic field from zero to an upper value (virgin curves); after that, we applied a field from a positive value to a negative value (down curves), and return (up curves), as we have already described in section 2.3. For each value of the magnetic field we acquired the $I(V)$ characteristics, with a step ΔI_{coil} and a waiting time t_w between each acquisition, chosen in order to perform accurate measurements; we fixed the waiting time to $t_w = 1$ s. The number of average sweeps was set to 30.

3.3.4 Discussion on the errors

In solid state experimental physics, the problem of the errors estimation is very important: often, it is not possible to reproduce an experiment in the same physical conditions an appropriate number of times, nor to have a wide sample of measures to get a standard error on the analyzed physical quantities.

The complexity of the experimental set-up, the presence of the filtering and amplification stages, electrical and thermal noise effects and the huge number of freedom degrees of a solid state sample affect strongly the measurements.

It is reasonable, however, that the real value of the physical quantity resulting from the measurements falls in a certain validity range, with a

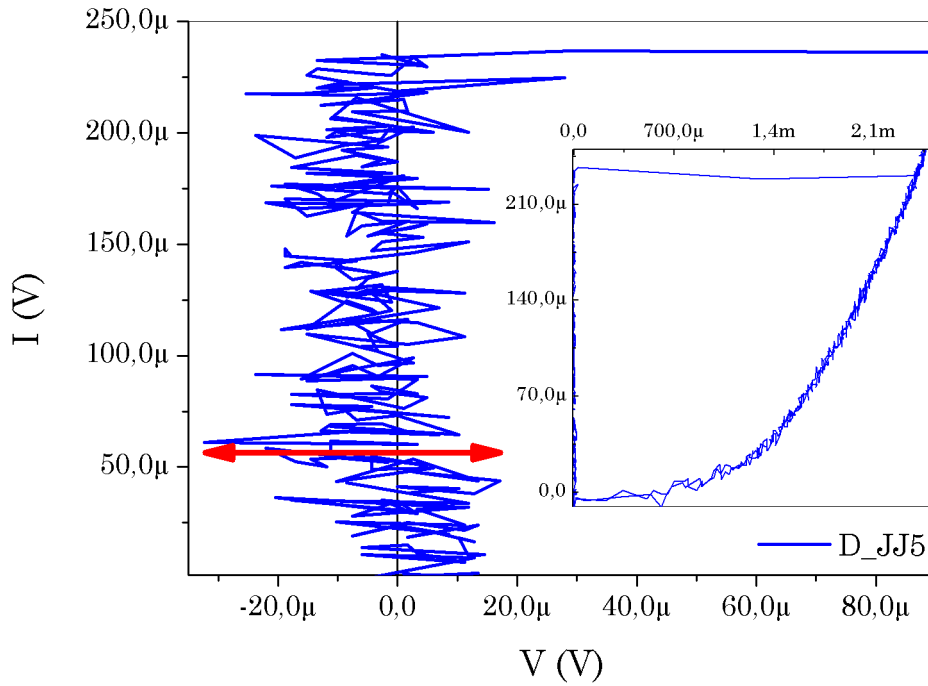


Figure 3.6: Error bar in a typical measured $I(V)$ (junction D_JJ5) due to the noise and the electronics

minimum and a maximum extreme; the semiamplitude of this range gives the *maximum error* (figure 3.6).

The maximum error on the voltage drop V between the junctions electrodes and the current flowing through the device I in the $I(V)$ measurements strictly depends on:

- the voltage range in which one acquires the curve;
- the temperature;
- the frequencies in play and the effect of the filtering stages;
- the electronics accuracy;
- the average operation made by the oscilloscope.

The relative error, instead, is typically the same in every condition: the estimated voltage and current errors are 1%.

The relative error on the resistance is estimated in the same way as in $I(V)$ curves, and it is about 2%.

For what concerns the error on the magnetic field, even if the relative error on the current generated in the coil I_{coil} is of about 0.0012% from the instrument specifications [54], the conversion factor has a bigger relative error. Most of all, we can not appreciate any magnetic field value with an error smaller than the step-field used in the measurements. From ΔI_{coil} values, in fact, one can calculate the magnetic field step ΔH as

$$\Delta H(\text{G}) = 3\Delta I_{\text{coil}}(\text{mA}), \quad (3.3)$$

so that the error is defined as the semiamplitude of the field-step.

More difficult is the error estimation on the temperature; however, for this thesis purpose it is sufficient to have an indicative value of the temperatures in play. A good thermalisation, in fact, certainly does not depend on the specific temperature value: it is sufficient that the measured quantity (current, voltage, magnetic field...) does not change because of thermal fluctuations for a time longer than the measure time.

Chapter 4

Experimental results

In this chapter, we condense all the experimental results with the final aim of a detailed characterization of the Josephson properties of SIFS JJs, made of a GdN barrier between two NbN electrodes (thicknesses in table 4.1).

We will analyze the spin-filter properties of the $R(T)$ measurements and we will give a description of the junctions electrostatics by studying the $I(V)$ curves. We will also report our experimental $I_c(H)$ and $I_c(T)$.

4.1 Spin-filtering efficiency

In figure 4.1, we represent the resistances $R(T)$ for all the junctions normalized to their maximum value (table 4.1), in order to make a comparison between curves with resistances falling in quite different ranges.

For all samples except for **B_JJ4**, $R(T)$ exhibits a typical semiconducting behavior up to 40 K, which is the Curie temperature T_{Curie} and a resistance falling to zero at a temperature of about 12 K; **B_JJ4** $R(T)$, instead, exhibits a prevailing semiconducting behavior until the superconducting transition temperature is reached.

The indirect exchange field from the ferromagnetic interlayer, which increases as the barrier thickness increases, induces a reduction in the tunnel barrier height for one spin channel (up or down); as a consequence, we observe a resistance decrease once the GdN becomes ferromagnetic (figure 2.9

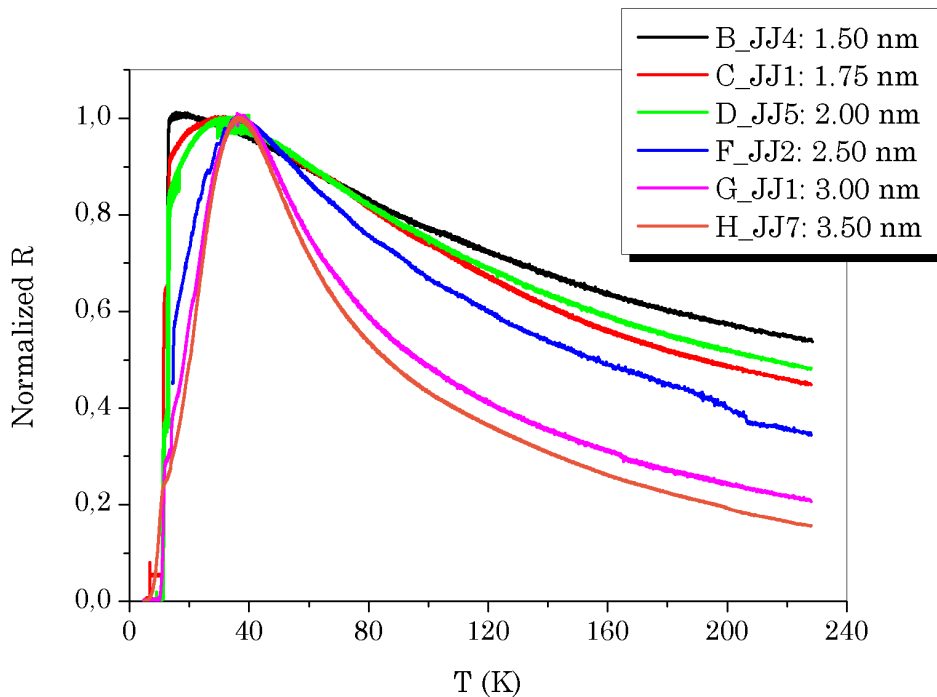


Figure 4.1: Normalized resistances vs. temperature for different GdN barrier thicknesses

in section 2.4.1). We also observe that the thicker the interlayer is, more quickly the resistance decreases, because the lower is the barrier height for a single spin channel. Junctions with thinner barrier such as B_JJ4 have a small exchange field, not sufficiently strong to filter a single spin channel, and the decrease in R with respect to the maximum value is 2%, while thicker junctions such as G_JJ1 have a resistance decrease of more than 10%.

In section 2.4.1 we anticipated that a practical indirect way to estimate the spin-filtering efficiency is to compare the semiconductor-like device resistance R^* (resistance in absence of spin-filtering) with the junction resistance R at a fixed temperature $T_c < T < T_{\text{Curie}}$. With the aim of estimating the resistance R^* , we performed the fit of the experimental $R(T)$ curves above the Curie temperature with the function [55]

$$R(T) = Ae^{\frac{B}{T+T_0}}, \quad (4.1)$$

Table 4.1: Maximum resistance value for each junction

Junction	t_{GdN} (nm)	R_{max} (Ω)
B_JJ4	1.50	5.77 ± 0.12
C_JJ1	1.75	8.55 ± 0.18
D_JJ5	2.00	7.54 ± 0.16
F_JJ2	2.50	13.5 ± 0.3
G_JJ1	3.00	52 ± 1
H_JJ7	3.50	261 ± 5

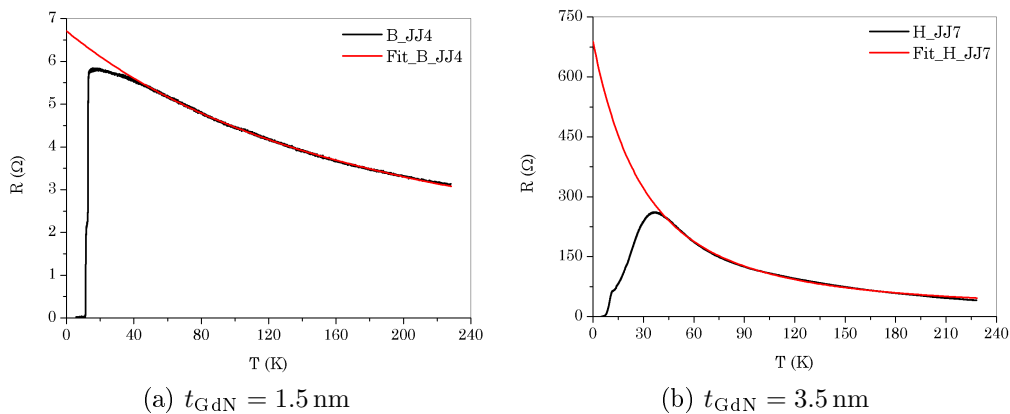


Figure 4.2: Resistance vs. temperature and fit with the semiconducting trend in equation 4.1

where A is associated to the resistance at very high temperatures and B is linked to the GdN energy gap in its paramagnetic phase. In figure 4.2 we plot the experimental fit for the JJs in the extreme cases of the GdN thickness 1.50 nm and 3.50 nm. Thus, we have calculated the spin-filtering efficiency at 15 K with the formula in equation 2.12 (table 4.2), and we have plotted in figure 4.3 the function $P(t)$. Since P is evaluated with an approximated formula and indirectly from the $R(T)$ curves, we will only give an indicative value for it, as Senapati et al. did in their work [46].

The spin-filtering efficiency follows a sigmoid curve, which typically describes saturation processes [56]. We fitted the curve with the function

$$\sigma(t) = \frac{L}{1 + e^{-k(t-t_0)}}, \quad (4.2)$$

Table 4.2: Spin-filtering efficiency

Junction	t_{GdN} (nm)	P (%)
B_JJ4	1.50	37
C_JJ1	1.75	59
D_JJ5	2.00	64
F_JJ2	2.50	88
G_JJ1	3.00	97
H_JJ7	3.50	98

which presents an exponential growth at the beginning, starting at the value t_0 (sigmoid's midpoint), a linear dependence for intermediate values of the thickness, with a slope determined by k (steepness), and a *plateaux* for the saturation value L .

The maximum spin-efficiency resulted from the fit is 100%, while the steepness is $k = (2.3 \pm 0.4) \text{ nm}^{-1}$. The calculated sigmoid's midpoint is the most important fit parameter, because it represents the value at which the spin-filtering efficiency appreciably increases. We have calculated a sigmoid's midpoint $t_0 = (1.69 \pm 0.05) \text{ nm}$, which is consistent with our picture: for barrier thicknesses larger than 1.5 nm, the SIFS junction deserves the title of *spin-filter*.

4.2 Damping regime of the junctions

Voltage-current characteristics, or $I(V)$, suggest a dominant role of tunneling processes: the presence of a hysteresis in these curves is linked to a capacitive effect as in conventional SIS junctions, and as a consequence to a recharge of the junction capacitance.

In figure 4.4 (a), we report the $I(V)$ curves at 300 mK for all the analyzed junctions, while in the inset we show the comparison between the sub-gap branches for all the junctions, i.e. the curves $i(v)$, where $i = I/I_c$ and $v = V/V_s$, with V_s switching voltage.

$I(V)$ measurements allow to determine qualitatively the damping regime of the JJs and to provide a first estimation of their characteristic parameters:

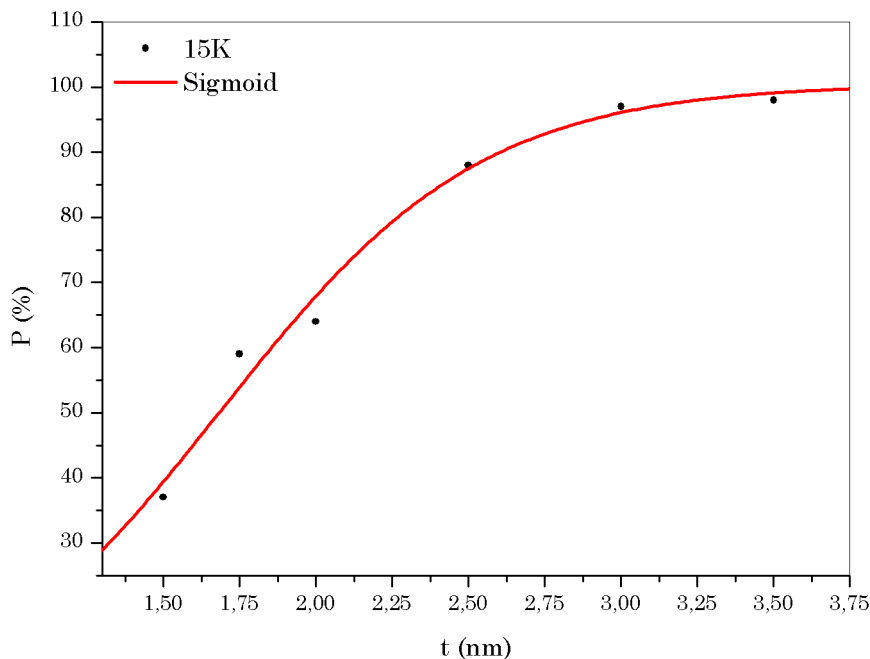


Figure 4.3: Spin-filtering efficiency vs. barrier thickness and fit function

critical currents, normal resistances and Stewart-McCumber parameters.

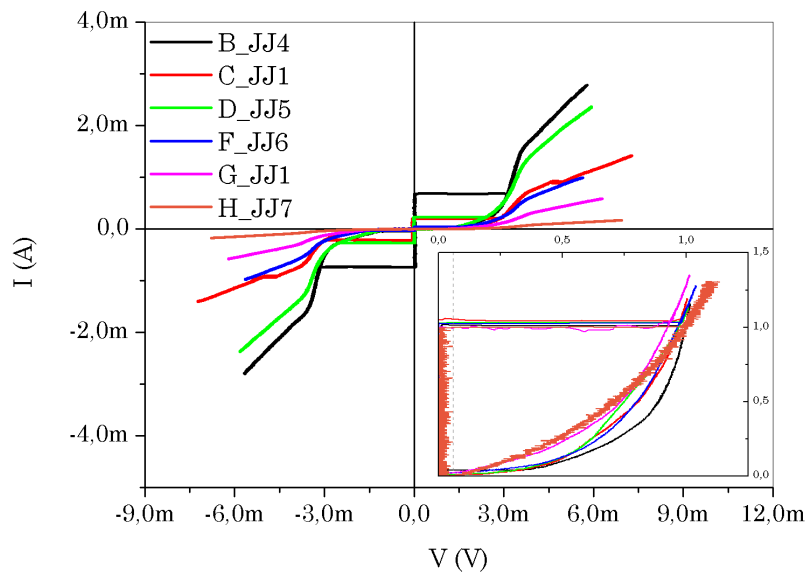
4.2.1 Critical currents

From the $I(V)$ curves we estimated the positive critical current I_c^+ and the negative one I_c^- by choosing a voltage threshold V_{th} far from the zero axes (dashed gray line in figure 4.4 (a)). These values allow to calculate the average critical current

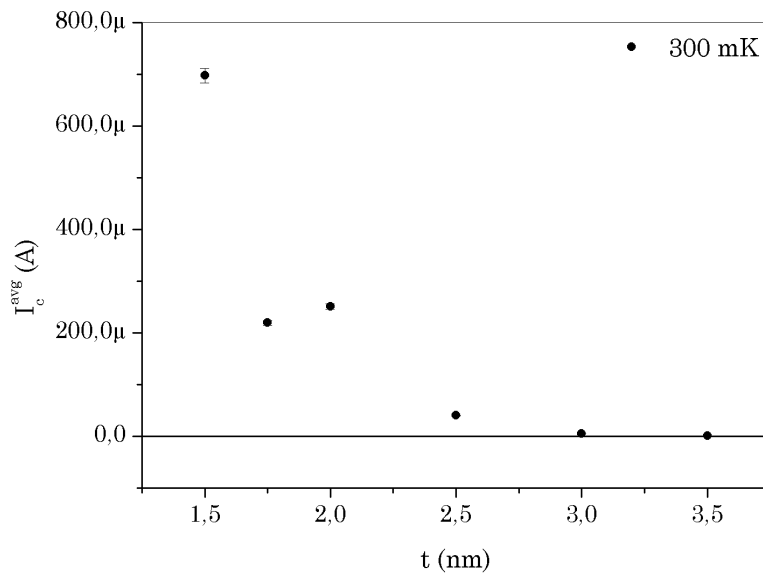
$$I_c^{avg} = \frac{I_c^+ + I_c^-}{2}, \quad (4.3)$$

with a maximum error $(\Delta I_c^+ + \Delta I_c^-)/2$.

In figure 4.4 (b), we report the average critical current as a function of the barrier thickness: it decreases exponentially as the barrier thickness increases by means of tunneling processes, as observed in other works on conventional Nb-AlO_x-Nb JJs [57].



(a) Long-range $I(V)$ characteristics at 300 mK



(b) $I_c(t)$

Figure 4.4: In (a): long-range $I(V)$ characteristics at 300 mK; in the inset, normalized current $i = I/I_c$ vs. $v = V/V_s$ in the sub-gap branch (the dashed gray line is the voltage threshold at which the critical current was taken). In (b): average critical current I_c^{avg} versus GdN barrier thickness t

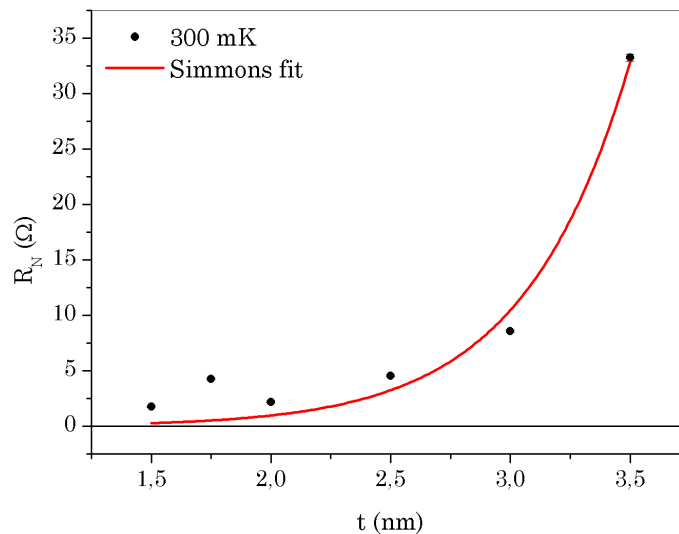


Figure 4.5: Normal resistance vs. the barrier thickness and fit with the Simmons model

4.2.2 Normal resistances

We have estimated the normal resistances by a linear fit in the normal branch of the $I(V)$ curves above the voltage gap $V_g = (4.00 \pm 0.04)$ mV, and we have plotted the slope inverse $G_N^{-1} = R_N$ as a function of the barrier thickness.

According to J.G. Simmons [58], it is possible to derive a single theory for the current flow through a barrier by means of tunnel effect, in which the normal resistance versus the barrier thickness t is exponential. In fact, R_N can be expressed in terms of the mean energy barrier height \bar{E} and the effective mass m^* of the particles involved in the conduction as

$$R_N(t) = \frac{2t}{3\sqrt{2m^*\bar{E}}} \left(\frac{h}{e}\right)^2 e^{\frac{2t}{h}\sqrt{2m^*\bar{E}}}. \quad (4.4)$$

By fitting the function $R_N(t)$ with the Simmons model, we verified the exponential dependence of the normal resistance and we found an energy barrier of some millielectronvolts (figure 4.5).

We have also calculated the characteristic voltage V_c for all the analyzed JJs,

$$V_c = I_c^{\text{avg}} R_N. \quad (4.5)$$

This last quantity allows to calculate the Josephson oscillation frequency ω_c ,

$$\omega_c = \frac{e^*V_c}{\hbar}, \quad (4.6)$$

which results of the order of some tens of gigahertz for the thicker barrier, up to some terahertz for the thinner one. This values are very similar to those observed in conventional SIS JJs.

4.2.3 Stewart-McCumber parameters

The damping regime of a junction is determined by the value of the Stewart-McCumber parameter.

As we can observe in the $I(V)$ characteristics in figure 4.4 (a), our junctions are hysteretic, and an underdamped regime is expected. We also expect that the NRSJ model described in chapter 1 allows to approximate very well the measured trends.

In figure 4.6, we report as an example a comparison between the normalized $I(V)$ curve of H_JJ7 and the simulated one for $n = 2$; the voltage-current characteristic for the Nb-AlO_x-Nb from Hypres (figure 1.10) is added as a term of comparison, since it is a typical junction with $n = \infty$.

The parabolic dependence in the sub-gap branch suggests that the Stewart-McCumber parameter can be estimated from the $\beta(\tau)$ curve in figure 1.13 in section 1.2.1. We collect in table 4.3 the measured ratios τ in percentage (hysteresis fractions),

$$\tau = I_r/I_c, \quad (4.7)$$

where I_r is the retrapping current, the β -factors estimated from the curve $\beta(\tau)$ in figure 1.13 and the quality factors Q . The error on these parameters is very high, because they are extrapolated from a curve that is the result of a set of approximations; in particular, we will follow the work by Devoret et al. [60], in which the error on the quality factor is of about 20%.

The calculated Stewart-McCumber parameters and quality factors, anyway, are only indicative for the following motivation. The sub-gap junctions shape is only approximated by a parabola: a better estimation of the Stewart-

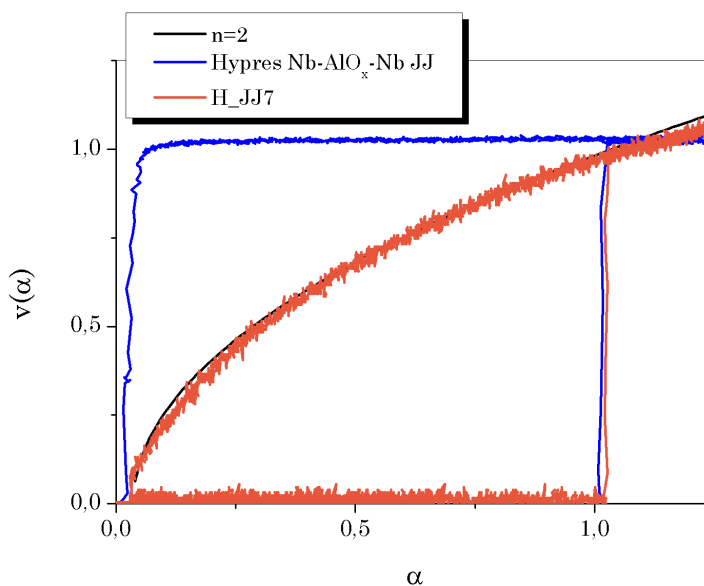


Figure 4.6: Comparison between the normalized $\bar{v}(\alpha)$ for the junction H_JJ7, the Hypres Nb-AlO_x-Nb junction and a simulated $\bar{v}(\alpha)$ in the NRSJ model for $n = 2$ and $k = 1.8 \cdot 10^{-2}$

McCumber parameter, which is out of these work purposes, can be achieved with the knowledge of the exact power-law of the normal current. For example, one can fit the sub-gap in the $I(V)$ characteristics with a power-law; after that, one has to solve the differential equation 1.39 in section 1.2.1 for the power found, with the aim of expliciting the normalized $\bar{v}(\alpha)$ for different k -values. From these curves, one can estimate the ratio τ for every k -values and the $\beta(\tau)$ curve. Finally, this trend allows to find the Stewart-McCumber parameter for the measured ratio τ from the experimental $I(V)$.

A very important result that goes beyond the quality factor accuracy is that the resistance values, calculated by the formula

$$R_0 = \frac{Q}{\omega_P C}, \quad (4.8)$$

where C is the plane-condenser geometrical capacitance, calculated with $A = 49 \mu\text{m}^2$, $\epsilon_0 = 8.85 \text{ pF/m}$ and $\epsilon_r = 26.5$ [59], are consistent with the order of magnitude of the “external” circuitry resistance, i. e. some tens of ohm.

Table 4.3: τ , β -parameters and quality factors Q for all the analyzed junctions

Junction	τ (%)	β	Q
B_JJ4	3.94 ± 0.09	1109	33 ± 7
C_JJ1	0.51 ± 0.01	1113	33 ± 7
D_JJ5	0.94 ± 0.02	1034	32 ± 6
F_JJ6	1.32 ± 0.03	992	31 ± 6
G_JJ4	0.053 ± 0.001	1168	34 ± 7
H_JJ8	7.01 ± 0.14	320	18 ± 4

The “external” circuitry resistance is given by the characteristic impedance of the lines and of the leads connecting the junction to the experimental setup, as in conventional tunnel SIS junctions analyzed in the work by Devoret et al. [60]. This means that dissipation in SIFS JJs is mostly determined by the environment in which the junction is embedded, while in common SFS JJs the damping is linked to R_N , i. e. the dissipation strictly depends on the intrinsic junctions parameters.

The clear advantage is that, for possible applications in superconducting electronics, spintronics and quantum circuits, the dissipation can be tuned by adjusting the overall circuitry; instead, SFS JJs are intrinsically more dissipative devices.

4.3 Fraunhofer pattern analysis

As extensively described in section 1.2.2, another important feature of a Josephson junction is its modulation in a magnetic field.

The effect of an in-plane magnetic field is to modulate the critical current of a JJ (section 1.2.2), as we can observe in the $I(V)$ curves at 0.3K in figure 4.7 for the F_JJ6, taken as reference.

From these curves we have estimated the critical currents I_c^- , I_c^+ and the average critical currents I_c^{avg} , as we have done in section 4.2, and we have plotted $I_c^{\text{avg}}(H)$ for magnetic field sweeps from positive to negative values, i. e. the *down* curves, and for magnetic field sweeps from negative to positive

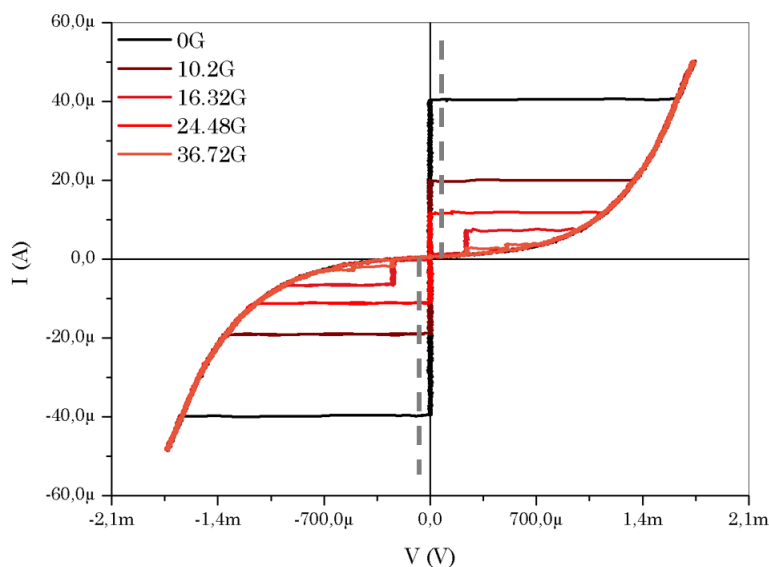


Figure 4.7: $I(V)$ curves at different applied in-plane magnetic fields for the junction F_JJ6: the dashed gray lines represents the voltage threshold V_{th} chosen in order to estimate the critical currents.

values, i. e. the up curves (figure 4.8).

Qualitative behaviors in figure 4.8 are consistent with what expected from a Josephson junction with a ferromagnetic barrier (section 2.3.2): a slight hysteresis in the Fraunhofer pattern can be observed in junctions with intermediate thicknesses, i. e. from barriers thicker than 1.75 nm, because the GdN magnetization influences the modulation of the critical current in the magnetic field. The only exception is the very small hysteresis for the junction H_JJ7, which is quite unexpected. However, deviations from the expected behavior can occur in prototype junctions like our SIFS.

Moreover, we have not observed any considerable distortion on the central lobe of the curves $I_c^+(H)$ and $I_c^-(H)$, as one can expect in the long junction limit.

Last but not least, the first minima in the pattern are not effectively zero: this could be due to a non-uniform current distribution in the system, as in SIS junctions with structural imperfections of the barrier [3], or to the presence of higher harmonics in the CPR relation.

In order to study these aspects on detail, we will perform the following

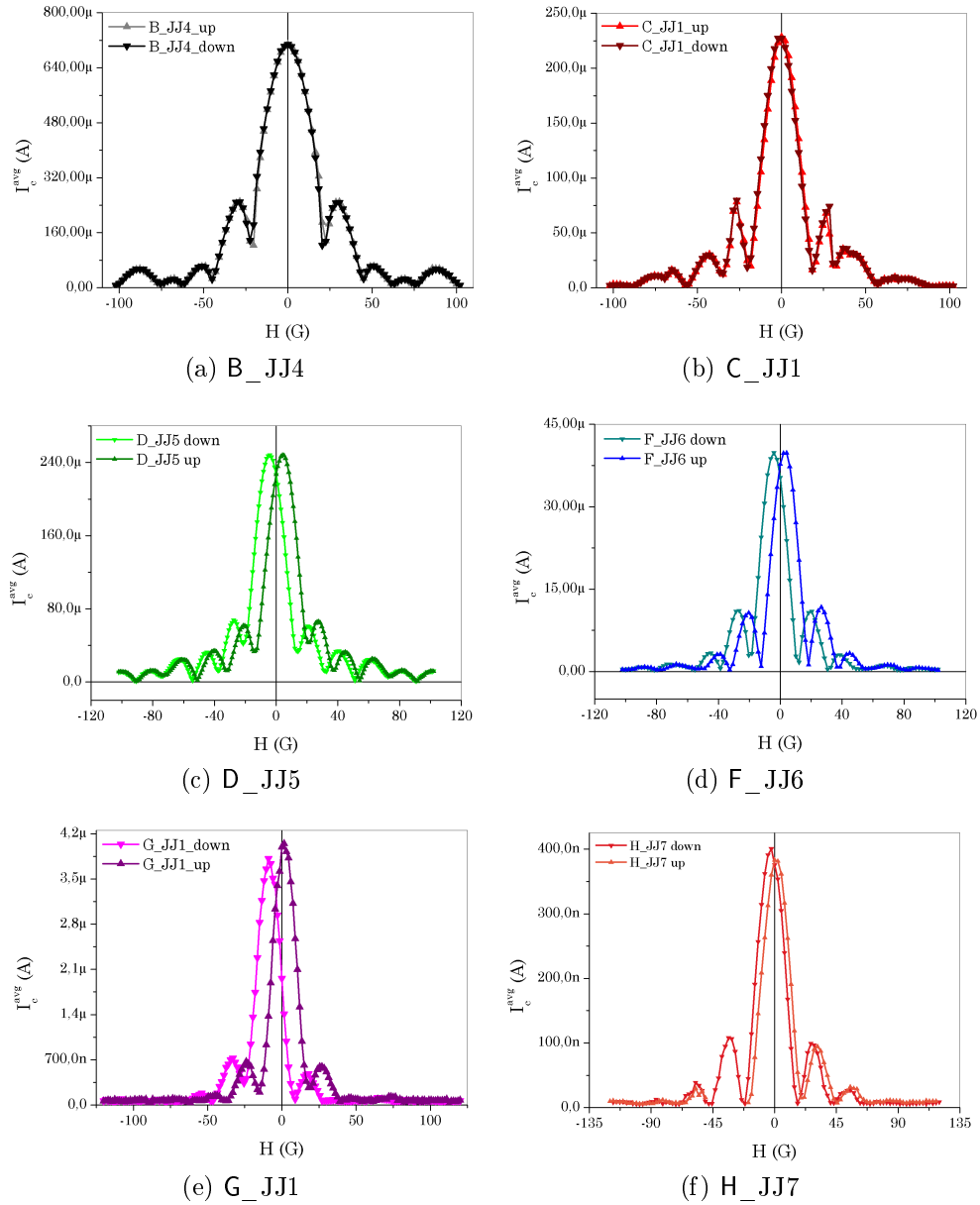


Figure 4.8: Down and up average critical current curves vs. the magnetic field for all the analyzed junctions

analysis:

- we will classify the analyzed junctions as small or long;
- we will study the hysteresis and a relative measure of the magnetization effect;
- we will analyze the Fraunhofer pattern periodicities and possible deviations from the expected one, i.e. the presence of a non-zero second harmonic in the CPR relation.

4.3.1 Long or small junctions regime

In order to properly classify these junctions as small or long, we need to estimate the Josephson penetration depth by taking into account that the electrodes dimensions are smaller than their London penetration depth in NbN ($\lambda_L \sim 200$ nm) and the ferromagnetic nature of the barriers. We substitute the magnetic spacing that appears in equation 1.73 with the expression

$$d''' = \mu_r t_{\text{GdN}} + \lambda_L \tanh\left(\frac{d_L}{2\lambda_L}\right) + \lambda_R \tanh\left(\frac{d_R}{2\lambda_R}\right), \quad (4.9)$$

where the GdN thickness t_{GdN} is multiplied by its relative permeability [42].

The relative permeability μ_r of the GdN strictly depends on the frequency of the field applied, the humidity, the temperature and other parameters and it is not easy to define a fixed value for it, also because of the difficulties that arise in the determination of the crystallographic structure of the GdN [59].

In similar SIFS JJs, A. Pal et al. estimated μ_r with a linear fit in different region of the barrier magnetization curve $M(H)$ [42].

Since our purpose is to verify if the junctions are small, i.e. the ratio L/λ_J satisfies the condition

$$L/\lambda_J < 1, \quad (4.10)$$

it is sufficient to have an underestimation of λ_J , i.e. an overestimation of the magnetic spacing d''' . We reach this goal by considering the highest value of μ_r , that is $\mu_r = 85$. In table 4.4 we show the λ_J values, with a relative error

Table 4.4: Critical density currents, estimated Josephson penetration depth and ratio L/λ_J of the analyzed samples with $\mu_r = 85$

Junction	J_c (A/cm ²)	λ_J (nm)	L/λ_J
B_JJ4	1422 ± 28	9.04 ± 0.9	0.74 ± 0.08
C_JJ1	449 ± 9	15 ± 2	0.46 ± 0.06
D_JJ5	510 ± 10	14 ± 1	0.51 ± 0.04
F_JJ6	82 ± 2	32 ± 3	0.22 ± 0.02
G_JJ1	8.24 ± 0.16	95 ± 10	0.074 ± 0.008
H_JJ7	1.07 ± 0.02	249 ± 25	0.028 ± 0.003

of 10% [42], and the ratio between the lateral dimension of the junctions ($L = 7 \mu\text{m}$) and λ_J . The error on the critical current density and on the ratio have been calculated by maximum error propagation, taking into account the errorless area. We can observe that these ratios satisfies the condition $L/\lambda_J < 1$ for all the junctions, but the thinner the barrier is, closer to 1 L/λ_J is.

This confirms the small junction limit, but we approach to the intermediate regime for thinner barrier thicknesses.

4.3.2 Hysteresis in the Fraunhofer patterns

In a Josephson junction with a ferromagnetic barrier the shift in field is strictly linked to the magnetization curve of the barrier $M(H)$. In these measurements we never reached the saturation field, and we only moved on the linear branch of the magnetization; as a consequence, we could perform a non-linear fit with the simplified model function

$$I_c(H) = I_c(0) \left| \frac{\sin\left(\frac{H+b}{a}\right)}{\frac{H+b}{a}} \right|, \quad (4.11)$$

where $I_c(0)$ is a scaling factor that represents the critical current at zero field, a is linked to the magnetic surface of the junctions,

$$a = \frac{\phi_0^*}{Ld^m}, \quad (4.12)$$

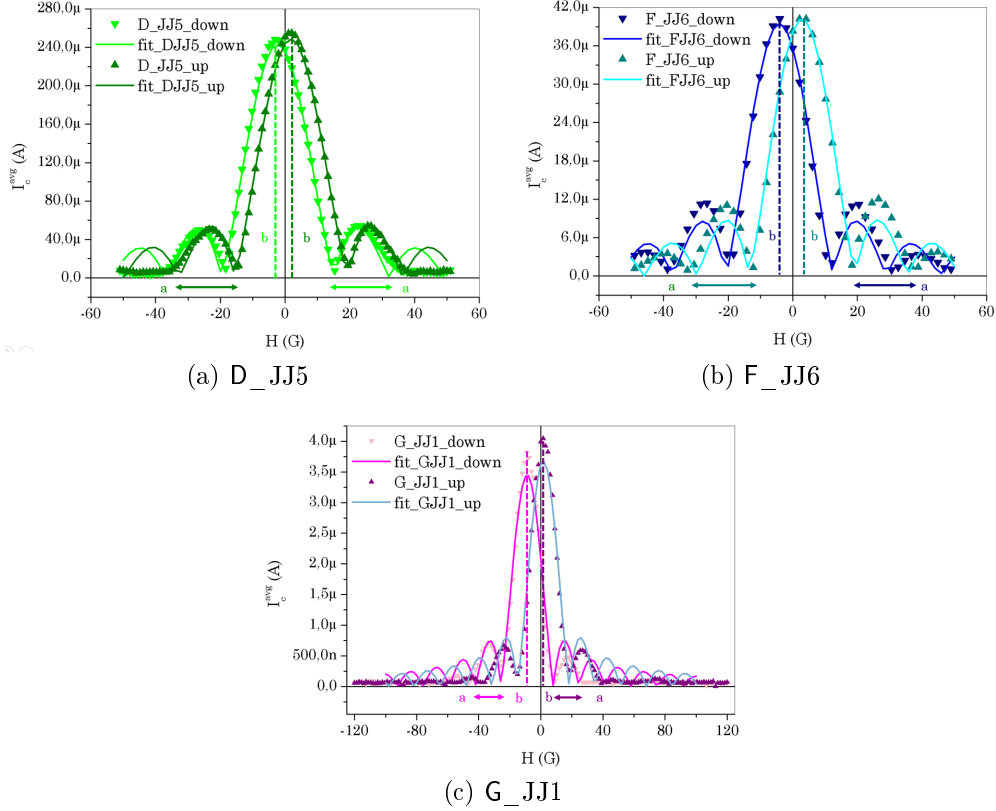


Figure 4.9: Fraunhofer pattern and fit with the simplified model in equation 4.11 for the junctions with bigger hysteresis (short dotted lines indicate the hysteresis, while the arrows represent the factor a)

with ϕ_0^* magnetic quantum flux $\phi_0^* = 2.07 \cdot 10^{-7} \text{ Gcm}^2$ for a Cooper pair, $L = 7 \mu\text{m}$ and d''' effective magnetic spacing, and b is the constant shift due to the residual magnetization of the barrier, i. e. the hysteresis. We show in figure 4.9 the calculated fit for the more ferromagnetic junctions.

In figure 4.10, we have plotted the calculated hysteresis b and the spin-filtering efficiency P . We can observe that for junctions with GdN thickness smaller than 2.00 nm, i. e. with lower spin-filtering efficiencies, the hysteresis is very small compared to that of junctions with thicker barriers and higher spin-filtering efficiency, according to the fact that the ferromagnet exchange field depends on the thickness.

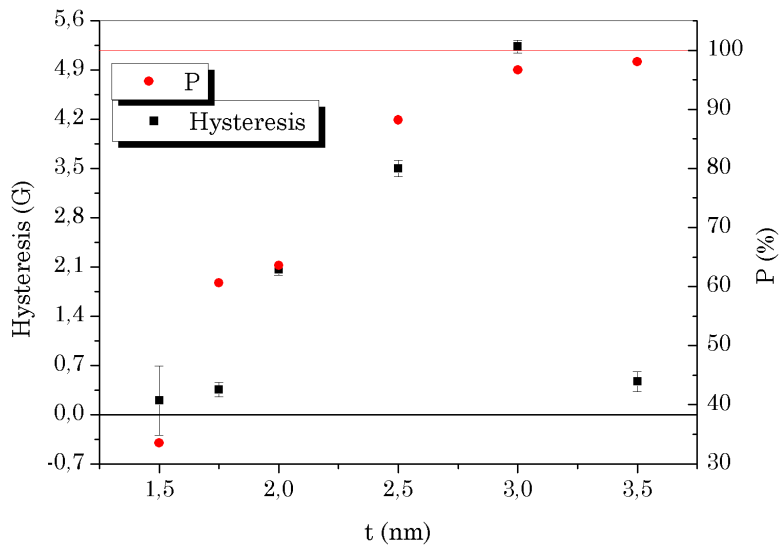


Figure 4.10: Comparison between the spin-filtering efficiency trend and the hysteresis curve vs. the barrier thickness

4.3.3 Second harmonic

The simple model proposed to calculate the shift in field of the Fraunhofer pattern does not reproduce the non-zero first minima that qualitatively emerges in junctions as B_JJ4, C_JJ1 and D_JJ5, and the half-periodicities in F_JJ6, G_JJ1 and H_JJ7.

These peculiar phenomena can not be simply explained in the sense of a disuniformity in the current spatial distribution. In order to analyze the $I_c(H)$ in our junctions, instead, we follow the Goldobin theory about the presence of a second harmonic in the CPR relation [36] (section 2.4.3).

In figure 4.11, we report the comparison between the normalized $I_{c,up}^{avg}(H)$, shifted by hand taking into account the calculated hysteresis b in the simplified fit 4.11, and the Goldobin curves. The qualitative values for g are reported in table 4.5.

The final result is that the second harmonic seems to be more important in junctions with a thicker GdN barrier, i.e. when the spin-filtering efficiency of the device increases. This can be due to the effect of the exchange field in the barrier, which forces the electrons to flip their spins in the direction of the magnetic field: this assumption is consistent with the idea

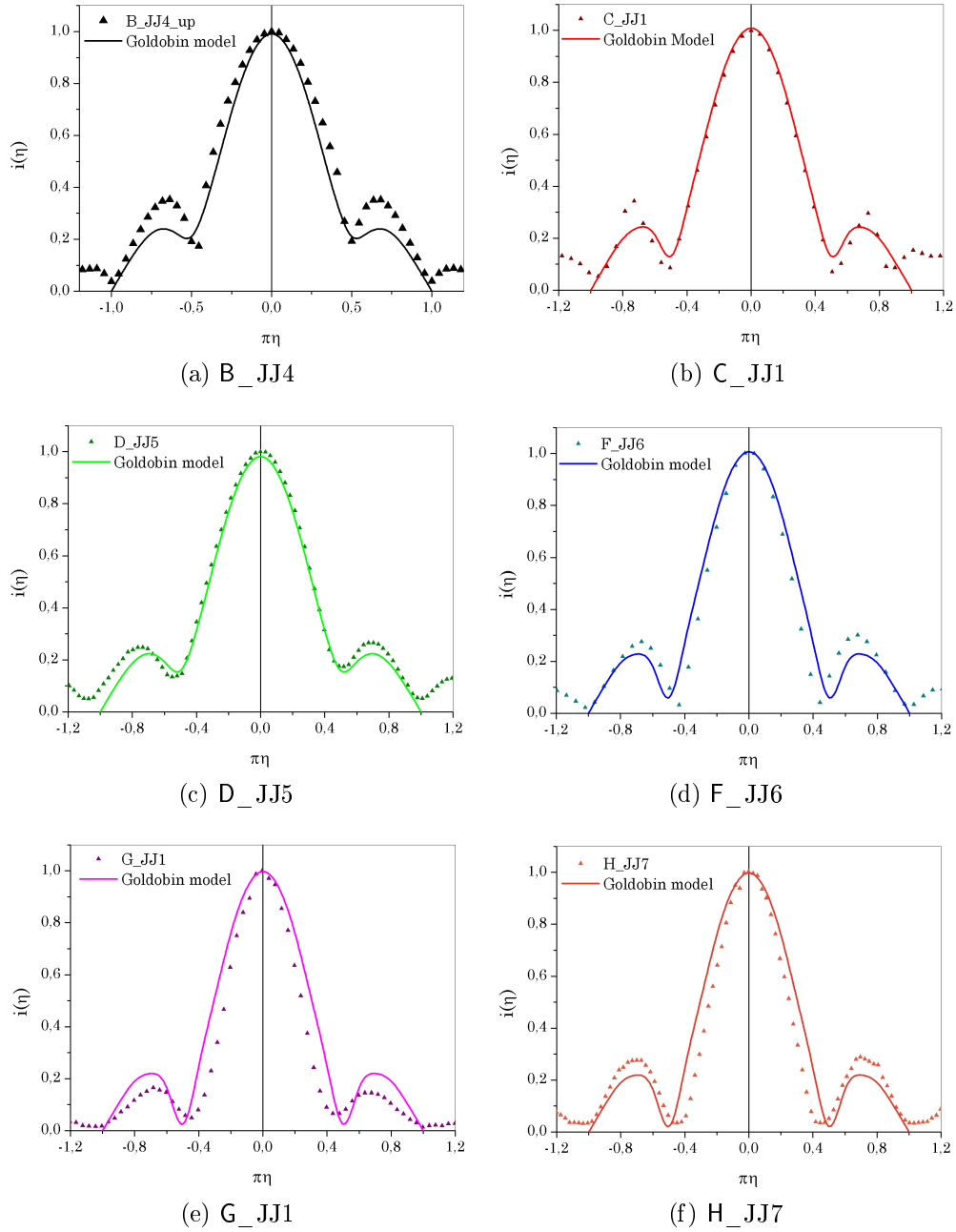


Figure 4.11: Comparison between the simulated theoretical curves with the Goldobin theory and the experimental ones

Table 4.5: Parameters g in the simulation of theoretical Goldobin curves

Junction	g
B_JJ4	3
C_JJ1	4.2
D_JJ5	5
F_JJ6	10
G_JJ1	25
H_JJ7	30

Table 4.6: Maximum critical current value for each junction at 300 mK

Junction	t_{GdN} (nm)	$I_c(0.3\text{ K})$ (μA)
B_JJ4	1.50	699 ± 7
C_JJ1	1.75	216 ± 2
D_JJ5	2.00	253 ± 3
F_JJ6	2.50	39.9 ± 0.4
G_JJ1	3.00	4.15 ± 0.04
H_JJ7	3.50	0.553 ± 0.006

that the conduction in SIFS JJs could be based on unconventional conduction phenomena, like: the presence of a *pure second harmonic*, as proposed by the Cambridge group [42], and the odd-frequency triplet conduction, as proposed by C. Richard et al. for SFS junctions [41] and by R.S. Keizer et al. in junctions with an half-metallic ferromagnetic barrier made of CrO_2 [61].

4.4 $I_c(T)$ curves

In order to have a complete overview of our junctions, we also measured the $I(V)$ curves at different temperature; from these measurements we got an estimation of I_c^+ and I_c^- , as we have done in section 4.2 for the electro-dynamical analysis of the junctions and in section 4.3 in Fraunhofer pattern measurements. We have plotted the average critical current I_c^{avg} versus the temperature; in particular, we show in figure 4.12 the average critical current normalized to its maximum value (table 4.6) versus the normalized temper-

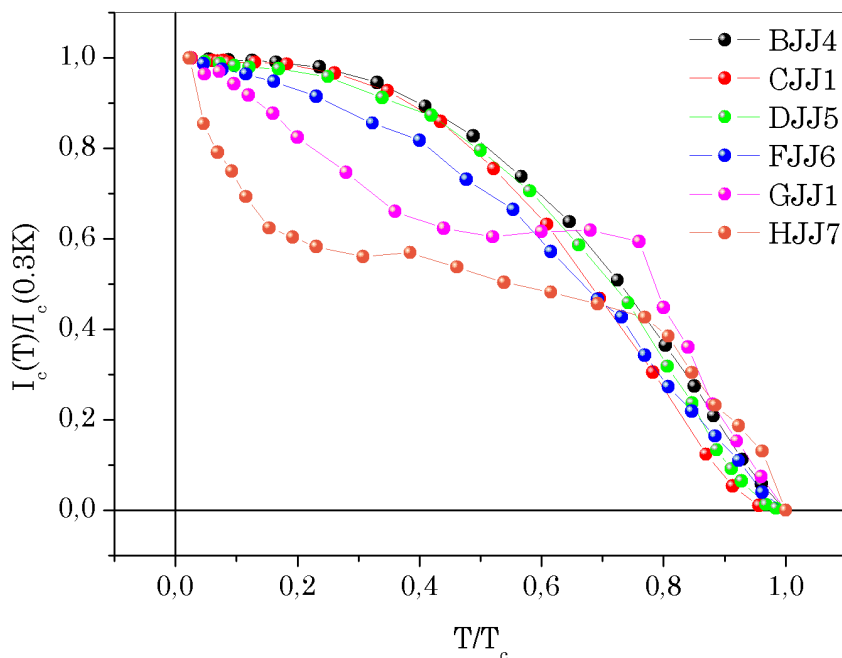


Figure 4.12: Average critical current normalized on its maximum value vs. the normalized temperature T/T_c

ature T/T_c , where the critical temperature is about $T_c = 12$ K.

The peculiar trend of the $I_c(T)$ seems to be the strongest proof that something far from the conventional superconductivity happens in JJs with thicker ferromagnetic insulator as a barrier.

In this thesis, we will not expose any quantitative study of the critical currents dependence on temperature, because further analyses have to be made, but a look on the measurements suggests that, as theoretically demonstrated by Bergeret et al. (section 2.4.4), the Ambegaokar-Baratoff relation (equation 1.80) fits very well experimental data for the thinner barriers (from 1.5 nm to 2.5 nm) in the high temperature limit, while it has to be corrected with a pre-factor dependent on the spin-filtering efficiency r at low temperatures. On the contrary, junctions with a thicker barrier (3.0 nm to 3.5 nm) present a change in concavity at about $T/(2T_c)$, which can be linked to a non-zero triplet current component.

Taking into account what we mentioned in section 2.4.4, we simulated in the Bergeret picture the normalized critical current curves as a function of the normalized temperature and we compared them with the experimental ones in the extreme cases of low spin-filtering efficiency (B_JJ4), intermediate spin-filtering efficiency (F_JJ6) and high spin-filtering efficiency (H_JJ7).

We expect a nearly zero exchange field h for non-spin-filter junctions and a r -factor linked to the spin-filtering efficiency P as

$$r = \sqrt{1 - P^2}, \quad (4.13)$$

so that it tends to 0 for high spin-filtering efficiency and to 1 for low spin-filtering efficiency.

In the Bergeret picture, in conclusion, one finds the curves in figure 4.13. All this is consistent with our picture: the effect of the magnetic exchange field is to break singlet Cooper pairs and to favor the triplet pair conduction in junctions with higher spin-filtering efficiency.

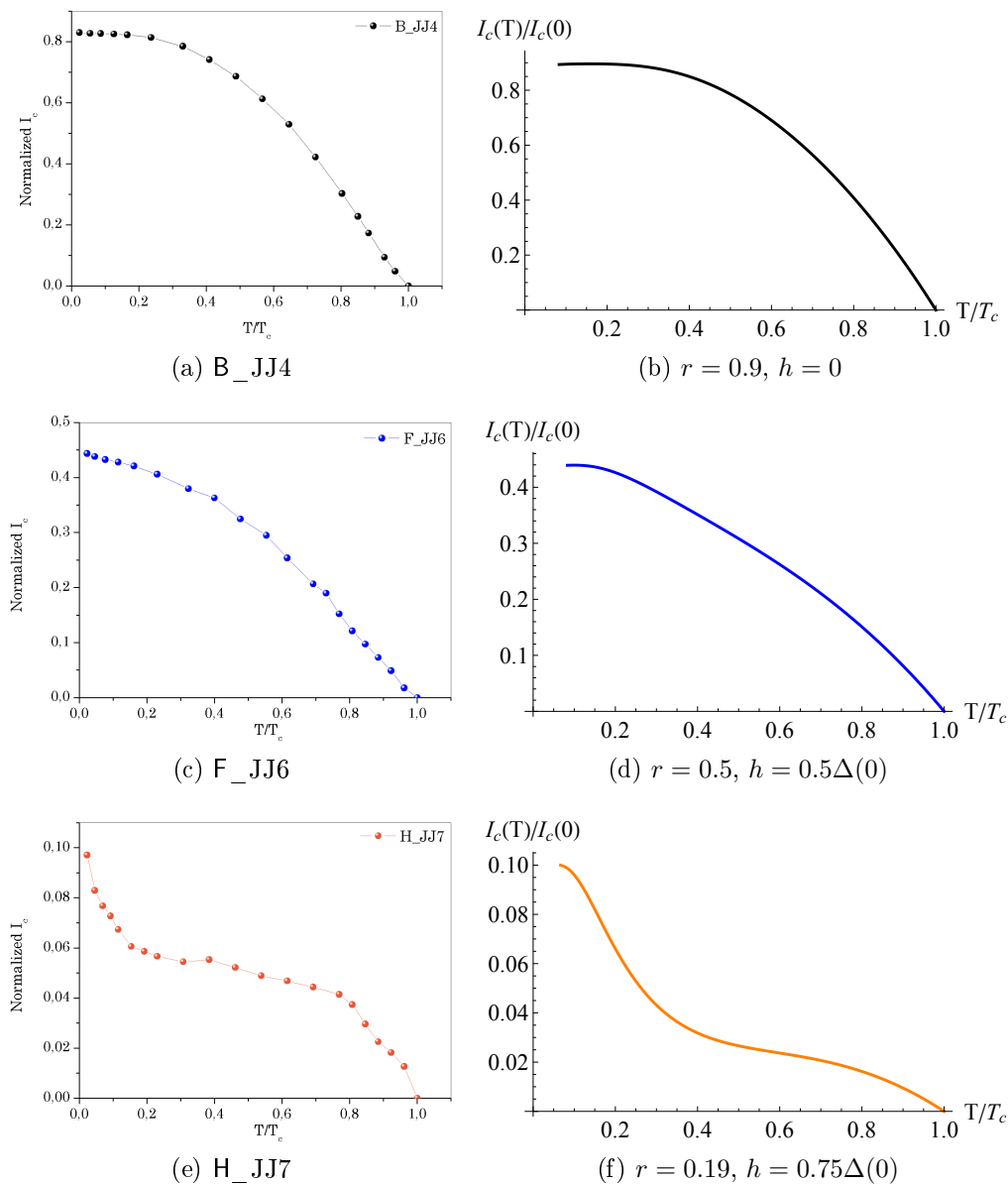


Figure 4.13: Comparison between the experimental $I_c(T)/I_c(0.3\text{ K})$ vs. T/T_c curves and the simulated ones in the Bergeret picture for noncollinear magnetic exchange fields ($\alpha = \beta = \pi/2$): *Mathematica11* simulations

Conclusions

In this work we have performed a methodical characterization of the first generation of superconductor-ferromagnetic insulator-superconductor (SfIS) Josephson junctions. The barrier, in particular, is composed of an insulating ferromagnetic barrier made of GdN, and it varies in a range from 1.50 nm to 3.50 nm. From a systematic study of $I(V)$ curves as a function of T and H , we have given evidence of a series of exotic behaviors, induced by the nature of the barrier.

The average critical current I_c^{avg} and the normal resistance R_N dependence on the GdN layer thickness t are exponential, suggesting that the conduction mechanism in the junctions is almost tunnel-like. The critical current decreases as the thickness barrier increases, so as the resistance increases with the GdN layer thickness.

A systematic and reliable fitting of $I(V)$ curves has given hints on the “electromagnetic” behavior of the junctions, and has allowed an estimation of their quality factors and information about the dissipation. We found that our junctions fall in the underdamped regime and that, differently from SFS JJs, dissipation is mostly determined by the environment and the circuit in which the junction is embedded: intrinsic dissipation mechanisms play a minor role. This is a very appealing property from the point of view of engineering applications in the spintronic and superconducting electronics fields.

The spin-filter nature occurring for thicker If barriers generates distinctive behaviors, which add to the interesting phenomena in SFS JJs, like the thickness-dependent hysteresis in the $I_c(H)$ curves. In particular, high spin-filtering efficiency due to the effect of the barrier exchange field h suggests

that Cooper pairs in a singlet state can not flow undisturbed through the junctions, and the Josephson effect in SIFS JJs could derive from other unconventional processes. From $I(V)$ measurements in presence of an external magnetic fields, for example, we observed that the hysteretic $I_c^{\text{avg}}(H)$ present an half-periodicity due to a second harmonic contribution in the CPR relation.

A pure second harmonic can be strongly correlated to the presence of higher orders of tunneling processes, which could involve also multiple electron pairs in a triplet state, favored over the singlet one. The exotic trend in measured $I_c(T)$ curves in the junctions with GdN thickness of 3.00 nm and 3.50 nm would be consistent with the presence of a Josephson triplet current.

The future prospective is to carry on a deeper analysis on the $I_c(H)$ curves and the $I_c(T)$ measurements to better explain unconventional conduction mechanisms, but also to perform switching current measurements to have a complete understanding of their electrodynamical properties. Low-dissipation spin-filter devices based on the robust Josephson effect, moreover, could be also employed in spintronics systems and in quantum and classical computers as building blocks (MRAM, qubits, logic elements).

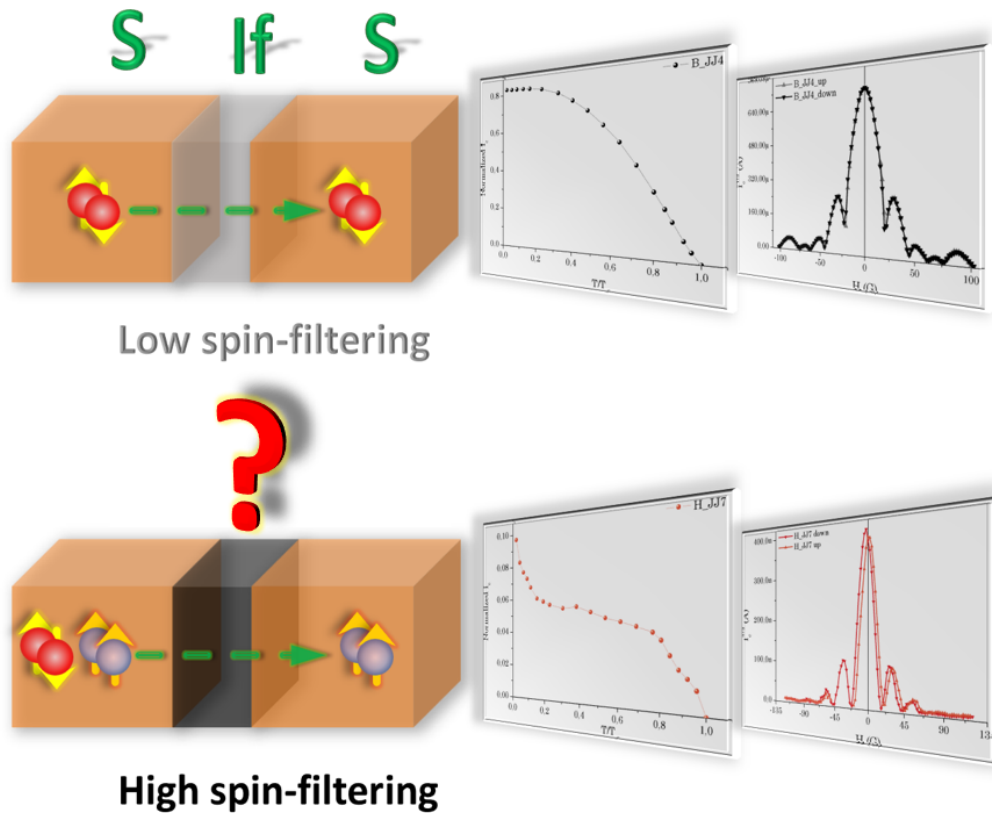


Figure 4.14: Pictorial representation of the conduction mechanism in SIfS JJs: Cooper pairs in a singlet state can not flow undisturbed when the exchange field in ferromagnetic barrier flips one of the two spin of the pair. The idea is that a Cooper pair in the triplet state, instead, can flow through the ferromagnetic insulator if the interlayer exchange field reduces the tunnel barrier experienced by the two electrons of the pair.

Bibliography

- [1] B.D. Josephson (1962) - *Possible new effects in superconductive tunneling*, Physics letters, Vol. **1**, number 7.
- [2] F. Leuenberger, A. Parge, et al. (2005) - *GdN thin films: Bulk and local electronic and magnetic properties*, Phys. Rev. B **72**, 014427.
- [3] A. Barone, G. Paternò (1982) - *Physics and application of the Josephson effect*, John Wiley & Sons, Inc., United States of America.
- [4] F. London, H. London (1935) - *The Electromagnetic Equations of the Supraconductor*. Proceedings of the Royal Society A: Mathematical, Physical and Engineering Sciences.
- [5] W. Meissner, R. Ochsenfeld (1933) - *Ein neuer Effekt bei Eintritt der Supraleitfähigkeit*. Naturwissenschaften. **21**, 44.
- [6] J. Bardeen, L.N. Cooper, and J. R. Schrieffer (1957) - *Microscopic Theory of Superconductivity*, Phys. Rev. **106**, 162 - 164.
- [7] L.P. Gor'kov (1958) - *On the energy spectrum of superconductors*, Soviet Phys. JETP **7**, 505.
- [8] P.W. Anderson (2015) - *On the energy spectrum of superconductors*, Nature Physics **11**, 93.
- [9] M. Tinkham (2004) - *Introduction to superconductivity*, Vol.1, Second edition, Dover Books on Physics.

- [10] K.K. Likharev (1979) - *Superconducting weak links*, Rev. Mod. Phys., Vol. **51**, No. 1.
- [11] K.K. Likharev (1986) - *Dynamics of Josephson junctions and circuits*, Gordon and Breach Science Publishers, Amsterdam.
- [12] W.C. Stewart (1974) - *Current-voltage characteristics of superconducting tunnel junctions*, Journal of Applied Physics, **45**, 452.
- [13] J.C. Swihart (1961) - *Field Solution for a Thin-Film Superconducting Strip Transmission Line*, Journal of Applied Physics, **32**, 461.
- [14] V. Ambegaokar, A. Baratoff (1963) - *Tunneling between Superconductors*, Physical Review Letter, **10**, 11.
- [15] L.G. Aslamazov, A.I. Larkin, Yu.N. Ovchinnikov (1969) - *Josephson effect in superconductors separated by a normal metal*, JETP, **28**, p.171.
- [16] H. Fukuyama, T. Ando (1991) - *Transport phenomena in mesoscopic systems*, Springer-Verlag, p.244.
- [17] P. Dubos (2001) - *Josephson critical current in a long mesoscopic SNS junction*, Physical Review B, **63**, 064502.
- [18] J.C. Cuevas, F.S. Bergeret (2007) - *Magnetic interference patterns and vortices in diffusive SNS junctions*, Physical Review Letters, **99**, 217002.
- [19] A. Buzdin, I. Baladié (2003) - *Theoretical description of ferromagnetic π -junctions near the critical temperature*, Phys. Rev. B **67**, 184519.
- [20] H. Courtois et al. (2008) - *Origin of Hysteresis in a Proximity Josephson Junction*, Physical review letters, **101**, 6, 067002
- [21] D. Massarotti et al. (2015) - *Breakdown of the escape dynamics in Josephson junctions*, Physical Review B, **92**, 054501
- [22] R.G. Seed, C. Vittoria, A. Widom (1994) - *Excess current in shunted Josephson weak links*, Journal of Applied Physics, **75**, 8195.

-
- [23] I.V. Vernik et al. (2012) - *Magnetic Josephson Junctions with Superconducting Interlayer for Cryogenic Memory*, IEEE Transactions on Applied Superconductivity, **23**, Issue:3, 13305938.
- [24] S. Narayana et al. (2012) - *Design and testing of high-speed interconnects for Superconducting multi-chip modules*, IOP Science, Superconductor Science Technology.
- [25] T. Ortlev et al. (2006) - *Flip-flopping fractional flux quanta*, Science: Vol. **312**, Issue 5779, pp. 1495-1497.
- [26] M.H. Volkmann et al. (2012) - *Implementation of Energy Efficient Single Flux Quantum (eSFQ) Digital Circuits with sub-aJ/bit Operation*, Superconductor Science and Technology, Volume **26**, Number 1.
- [27] S. Nagasawa et al. (1999) - *High-frequency Clock Operation of Josephson 256-word x 16-bit RAMs*, IEEE TRANSACTIONS ON APPLIED SUPERCONDUCTIVITY, **9**, 2.
- [28] G. Grosso, G. Pastori Parravicini (2014) - *Solid State Physics*, Second edition, 2000 Elsevier Ltd.
- [29] K.H.J. Bushow, F.R. De Boer (2004) - *Physics of Magnetism and Magnetic Materials*, Kluwer Academic Publisher, New York.
- [30] L.N. Bulaevskii, A.I. Buzdin, et al. (1985) - *Coexistence of superconductivity and magnetism. Theoretical predictions and experimental results*, Adv. Phys. **34**, 175–261.
- [31] Y. Matsuda, Shimahara, Hiroshi (2007) - *Fulde-Ferrell-Larkin-Ovchinnikov State in Heavy Fermion Superconductors*, J.Phys.Soc.Jpn.**76**: 051005.
- [32] H. Shimahara (2008) - *Theory of the Fulde-Ferrell-Larkin-Ovchinnikov State and Application to Quasi-Low-Dimensional Organic Superconductors: The Physics of Organic Superconductors and Conductors*, Springer, Berlin.

- [33] K.H.J. Buschow (1992) - *Concise encyclopedia of magnetic and superconducting materials*, II ed., Elsevier, University of Amsterdam, The Netherlands.
- [34] T.I. Larkin (2012) - *Ferromagnetic Josephson switching device with high characteristic voltage*, Applied Physics Letters, **100**, 222601.
- [35] A. K. Feofenov et al. (2010) - *Implementation of superconductor/ferromagnet/superconductor π -shifters in superconducting digital and quantum circuits*, Nature Physics **6**, 593–597.
- [36] E. Goldobin (2007) - *Josephson junctions with second harmonic in the current-phase relation: Properties of φ junctions*, Physical Review B, **76**, 224523.
- [37] H. Sickinger et al. (2010) - *Experimental evidence of a ϕ -junction*, Phys. Rev. Lett., vol. **109**, p. 107002, 2012.
- [38] D. Massarotti et al. (2015) - *Macroscopic quantum tunneling in spin-filter ferromagnetic Josephson junctions*, Nat. Commun. 6:7376 doi:10.1038/ncomms8376.
- [39] Ya.V. Fominov et al. (2007) - *Josephson effect due to the long-range odd-frequency triplet superconductivity in SFS junctions with Néel domain walls*, Phys. Rev. B **75**, 104509.
- [40] H. Meng et al. (2015) - *Long-range superharmonic Josephson current and spin-triplet pairing correlations in a junction with ferromagnetic bilayers*, Scientific Reports. 2016;6:21308. doi:10.1038/srep21308.
- [41] C. Richard, M. Houzet, J.S. Meyer (2013) - *Superharmonic Long-Range Triplet Current in a Diffusive Josephson Junction*, Physical Review Letters, **110**, 217004.
- [42] A. Pal et al. (2014) - *Pure second harmonic current-phase relation in spin-filter Josephson junctions*, Nat. Commun. 5:3340 doi:10.1038/ncomms4340.

- [43] D. Massarotti et al. (2016) - *Low temperature properties of spin filter NbN/GdN/NbN Josephson junctions*, Physica C. Superconductivity and its applications, 000, 1-6.
- [44] F.S. Bergeret et al. (2012) - *Spin polarized Josephson junctions and quasiparticles currents in superconducting spin-filter tunnel junctions*, Physical Review B, **86**, 060506(R).
- [45] G.X. Miao, J.S. Moodera (2014) - *Spin manipulation with magnetic semiconductors barriers*, PCCP.
- [46] K. Senapati et al. (2011) - *Spin-filter Josephson junctions*, Nature Materials, Letters, Macmillan Publisher Limited.
- [47] J.H. Park, E. Vescovo, et al. (1998) - *Direct evidence for a half-metallic ferromagnet*, Nature, VOL. **392**, NSLS Brookhaven National Laboratory, Upton, New York 11973-5000, USA Center for Superconductivity Research, Department of Physics, University of Maryland, College Park, Maryland 20742, USA.
- [48] R.J. Gambino et al. (1970) - *Magnetic properties of GdN and GdN_{1-x}O_x*, Journal of Applied Physics, **41**, 3.
- [49] F. Leuenberger et al. (2006) - *X-ray magnetic circular dichroism at the Gd L_{2,3} absorption edges in GdN layers: The influence of lattice expansion*, Physical Review B, **73**, 214430.
- [50] K. Senapati et al. (2011) - *Structural evolution and competing magnetic orders in polycrystalline GdN films*, Physical Review B, **83**, 014403.
- [51] K. Senapati et al. (2010) - *Magnetic exchange hardening in polycrystalline GdN thin films*, Journal of Physics: Condensed Matter, 22, 302003 (5pp), **83**, 014403.
- [52] D. Stornaiuolo (2007) - *Advances in HTS mesoscopic junctions*, Tesi di Dottorato in Tecnologie Innovative per Materiali, Sensori e Imaging, Università degli Studi di Napoli "Federico II".

- [53] © Copyright Agilent Technologies (2002) - *Agilent 33120A,15MHz Function, Arbitrary Waveform Generator, Agilent User's guide*, Publication. Number 33120-90006.
- [54] ® Keithley: A techtronik Company - *Source meter SMU instruments: Series 2400*.
- [55] O. Madelung (1978) - *Introduction to Solid-State theory*, Springer Verlag Berlin Heidelberg, New York.
- [56] J. Han, C. Morag (1995) - *The influence of the sigmoid function parameters on the speed of backpropagation learning*, Natural to Artificial Neural Computation. pp. 195–201.
- [57] E.P. Houwman et al. (1990) - *Fabrication and properties of Nb-Al- AlO_x -Nb Josephson tunnel junctions with a double oxide barrier*, Journal of Applied Physics **67**, 1992.
- [58] J. G. Simmons (1963) - *Generalized Formula for the Electric Tunnel Effect between Similar Electrodes Separated by a Thin Insulating Film*, J. Appl. Phys. **34**, 1793.
- [59] C. Bonnelle, N. Spector (2015) - *Rare-Earths and Actinides in High Energy Spectroscopy*, Springer, Science+Business Media Dordrecht.
- [60] M.H. Devoret et al. (1984) - *Resonant Activation from the Zero-Voltage State of a Current-Biased Josephson Junction*, Physical Review Letters, **53**, 13.
- [61] R.S. Keizer et al. (2006) - *A spin triplet supercurrent through the half-metallic ferromagnet CrO_2* , Nature Letters, **439**.